First-Principles Calculations of Transition Metal Phthalocyanines for Graphene-based Supercapacitor

Apichai JOMPHOAK

Japan Advanced Institute of Science and Technology

Doctoral Dissertation

First-Principles Calculations of Transition Metal Phthalocyanines
for Graphene-based Supercapacitor

Apichai JOMPHOAK

Supervisor: Ryo Maezono

School of Information Science
Japan Advanced Institute of Science and Technology

Degree conferment: September, 2017

Abstract

The research and development of the novel composite materials for electrodes used in supercapacitor applications are indeed in the great demand due to the need of the improving electrodes that can largely enhanced capacitance. Supercapacitors are generally governed by the same fundamental equations as the typical capacitors. The notable differences are that supercapacitors have utilized their electrodes with higher surface area materials and dielectrics with smaller gap between electrode and insulator to achieve several orders of magnitude greater than conventional capacitors. These lead them to have higher energies than those of typical capacitors and greater power than battery.

In order to realize the supercapacitors, the key strategy is to improve the electrode with larger surface area and also enhanced ability to attract more electrolyte ions. Therefore, the main focus in this dissertation aims to rectify and seek for electrode materials that would improve the ability to attract more ions with the supported larger surface of graphene-based electrodes. The desired materials for the extra-attached layer should also be easy to realize the charge transfer within the material inducing double layer and more stable stacking for better lifetime of device. The promising candidate is proposed with the transition metal phthalocyanines (TMPcs). The available electrons between these interlayers would form a π-π interaction, and the central metallic ion of TMPcs can also be adsorbed as an anchor for attaching a molecule on graphene sheet. Thus, the central target of this research is to investigate the molecular and electronic structures of each selected TMPcs (MnPc, FePc, CoPc, NiPc, and CuPc) that are used as model to formulate stability in microscopic perspective. *Ab initio* calculation is possible by using density functional theory (DFT) for evaluating binding energies and geometry optimization.

In this dissertation, the exchange-correlation (XC) functionals of LDA, PBE, and B3LYP were used to describe and predict the energies and formations of graphene and TMPcs interlayers, and also the individual geometries of graphene and TMPcs. The computational results expect the binding energies of TMPcs on a graphite surface, and the bond length and angle of each TMPc molecular structures whereas experiment and calculation results are in good agreement. Their binding energies show large stabilities for the TMPc/G interlayers, and for comparison under the same XC functional, CoPc/G possesses the lowest one, except the B3LYP results of MnPc/G. The results indicate that, among these formations, CoPc has the most stable structure of stacking TMPc on a basal graphene layer, compared with other candidates within the same calculation parameters. However, it is also pointed out the prediction depends on the choice of selected XC functionals, where the results obtained from PBE and B3LYP share similar trend while those from LDA shows several fluctuated ones.

Furthermore, HOMO orbital distribution of completely isolated CoPc molecule has one of the $a_{1g}(d_{z^2})$ electron is available, and the empty b_{1g} orbital, which is largely composed of $d_{x^2-y^2}$. The CoPc states e_g are mixed due to hybridization, the interaction between the CoPc and graphene, one electron from the $a_{1g}(d_{z^2})$ would transferred from graphene. This suggestion comes from the charge transfer between the d^7 Co configuration and graphene through the d_{z^2}

orbital. This may lead to one of the possible reason for intermediate formation between CoPc and graphene with strong interaction. However, the computational HOMO-LUMO results from LDA has noticeably failed to represent the $a_{1g}(d_{z^2})$ of CoPc, but PBE and B3LYP achieved to reproduce this state so LDA may not be a preferable XC choice for calculation of both energy and orbital distribution.

In addition to the geometry optimization results, most of the TMPc molecules are settled and immobilized at one of the center of benzene ring, hexagonal site (H-site), except for the cases of CuPc and MnPc that are slightly of the central grid. For the case of NiPc/G, the edges of graphene sheet are bent toward the NiPc monomer from the PBE and B3LYP results while there is no such noticeably change in NiPc structures from all other obtained results. This might be possibility to have strong artifact on the distortion estimations due to too small size of graphene fragment, only 25 benzene rings. However in contrast, there are also some cases that the graphene sheets are still in flat shape, but TMPcs structures are distorted after the geometry have been optimized, such as FePc and MnPc. The deformation of graphene fragment in the model would lead deformation of TMPc layers in reality because the basal graphene substrate would be infinity spread firmly. On the other hand, when the deformation occurred as spatially non-uniform force to graphene substrate, this particular case would lead to substrate damaging where graphene would be eventually peeled off by TMPc layer, and then shortened in electrode lifetime.

Therefore from the computational prediction of CoPc for the strongest anchoring on basal graphene sheet, the production of CoPc/G electrode process in the laboratory scale is feasible that would lead to the possible construction of these tunable hybrid electrodes used for super-capacitor applications.

Acknowledgments

During my research, I have gradually met many intellectual people, and each person has eventually made a great contribution in my research efforts. They have been providing me with valuable inputs and also fruitful feedback in their academic fields of expertise. As I have finalized my dissertation, I would like to take this delightful opportunity to express my sincere gratitude toward the following people who have contributed to my success both directly and indirectly.

I would like to express my highest gratitude for my supervisor, Assoc. Prof. Dr. Ryo Maezono for his tireless faith in me during my entire research and dynamically keeping me working hard toward my goal. The underlying educational enlightenment and knowledgement represented in this dissertation are utmostly the true product of his motivation, inspiration, endless support, and encouragement. Assoc. Prof. Dr. Maezono has not only provided me the pristine guidance but also maintained an excellent standard and set himself as a role model for developing my career path in scientific research.

Other than my supervisor, there are a few other people who deserved the specific mention for their critical guidances and contributions. First, Prof. Dr. Thawatchai Onjun has been my excellent mentor and one of the inspired sources since I started my graduate career. He has perpetually motivated and kept me improving to always be both a holistic learner and a gainful listener. In addition, I am grateful for his excellent example as a successful scientist, a professor, and a good human being.

Next, I am thankful to Asst. Prof. Dr. Kenta Hongo who has always offered his helpful inputs and useful advice throughout several special projects. He has provided invaluable amounts of feedback and support in my research path as well.

Moreover, all of my research colleagues at Maezono Laboratory, JAIST, have helped me with the research work several times, and I am sincerely thankful to them for their assistance.

I would like to gratefully thank to all of my committee members; Professor Hiroyuki Iida, Professor Hiroshi Mizuta, and Professor Tatsuya Shimoda, and also to my external examiner; Professor Tamio Oguchi, for their meticulous reviews, productive feedback, fruitful advices, and overall suggestions during my preliminary and dissertation defense.

I would also like to acknowledge the financial support from the JAIST-NECTEC-SIIT Dual Degree Scholarship program for giving me the opportunity and supportive funding which enabled me to progress successfully and complete my dissertation.

And finally, my deepest gratitude must go toward my dearest parents for their endless support and unconditional love that they have given and cherished me throughout my entire life. They have been the main reason that I have been able to accomplish till today, and I am extremely indebted to them. I want to gratefully thank them, and state that I love them very much.

Furthermore, my special thanks have to go to my better half, Dr. Wanida. Her accompany with all the love, kindness, encouragement, support, and patience has eased my staying at JAIST to be fulfilled with happiness and alleviating, and that have always kept me energetic and active while working on my Ph.D. research. This dissertation would not be feasible and complete without her encouragement and sacrifice. I need to thank her for just being a wonderful person in my life.

At last but not the least, all have been devoted to my son, Lego Achawin, because you are my everything.

Contents

"This dissertation was prepared according to the curriculum for the Collaborative Education Program organized by Japan Advanced Institute of Science and Technology and Sirindhorn International Institute of Technology, Thammasat University."

List of Figures

List of Tables

List of Acronyms

2D	Two Dimensional
3D	Three Dimensional
AFM	Atomic Force Microscope
a.u.	Hartree Atomic Units
B3LYP	Becke, 3-parameter, Lee-Yang-Parr exchange-correlation functional
BPG	Basal-Plane Pyrolytic Graphite
BZ	Brillouin Zone
C	Carbon
CDR	Recordable Compact Disc
CH_3CN	acetonitrile
CME	Carbon Microelectrode
CNT	Carbon Nanotube
CoPc	Cobalt Phthalocyanine
Cu	Copper
CuPc	Copper Phthalocyanine
DN	Double Numerical
DNA	Deoxyribonucleic Acid
DFT	Density Functional Theory
EDLC	Electrochemical Double-Layer Capacitor
EMI	Electromagnetic Interference
ESR	Electron Spin Resonance
eV	Electron Volt
FCC	Face-Center-Cubic
FePc	Iron Phthalocyanine
G	Graphene
GCE	Glassy Carbon Electrode
GGA	Generalized Gradient Approximation
GO	Graphene Oxide
H	Hydrogen
HEG	Homogenous Electron Gas
HF	Hartree-Fock
Hg/Hg_2SO_4	Mercury/Mercury Sulphate
HOMO	Highest Occupied Molecular Orbital
HOPG	Highly Oriented Pyrolytic Graphite

HPC	High Performance Parallel Computing
HSE	Heyd-Scuseria-Ernzerhof exchange-correlation functional
H_2SO_4	Sulfuric Acid
IPES	Inverse Photoemission Spectroscopy
KMC	Kinetic Monte Carlo
KOH	Potassium Hydroxide
KS	Kohn-Sham
LBL	Layer-by-Layer
LDA	Local Density Approxiamtion
LED	Light Emitting Diode
$Li/SOCl_2$	Lithium-Thionyl Chloride
LSDA	Local Spin-Density Approximation
LUMO	Lowest Unoccupied Molecular Orbital
MBE	Molecular Beam Epitaxy
MnPc	Manganese Phthalocyanine
MO	Molecular Orbital
MPc	Metal Phthalocyanine
MWNT	Multi-Walled Nanotube
N	Nitrogen
Ni	Nickel
NiPc	Nickel Phthalocyanine
NLCC	Nonlinear Core Correction
NMR	Nuclear Magnetic Resonance
OFET	Organic Field-Effect Transistor
OLED	Organic Light Emitting Diode
OPGE	Ordinary Pyrolytic Graphite Electrode
OTFT	Organic Thin Film Transistor
PANI	Polyaniline
PBE	Perdew-Burke-Ernzerhof exchange-correlation functional
PEDOT	Poly(3,4-ethylenedioxythiophene)
PES	Photoemission Spectroscopy
PPy	Polypyrrole
PW91	Perdew-Wang exchange-correlation functional
QMC	Quantum Monte Carlo
RCACI	Research Center for Advanced Computing Infrastructure
RGO	Reduced Graphene Oxide
RuO_2	Ruthenium Oxide
SAM	Self-Assembled Monolayer
SCF	Self-Consistent Field
SPCE	Screen Printed Carbon Electrode
SR	Screened-Short Range
SWNT	Single-Walled Nanotube
TEM	Transmission Electron Microscopy
TMPc	Transition Metal Phthalocyanine

UPS	Ultraviolet Photoelectron Spectroscopy
VCE	Vitreous Carbon Electrode
vdW-DF	van der Waals Density Functional
VWN	Vosko-Wilk-Nusair
XC	Exchange-Correlation
XRD	X-Ray Diffraction

Chapter 1

Introduction

1.1 Motivation

The demand of more advanced energy storage for improved and enhanced characteristics, such as the power density with higher magnitudes, the charging time with shorter duration, and its cycles with longer life span, has predictably become critical focus of many research communities in corresponding to the global technology transformation. Over the last decade, supercapacitors have potentially become one of those energy storage devices which have significantly been developed and refined to be more efficient devices.

Based upon the reviews of several literatures [4, 15, 16], there is a possible tendency that supercapacitors will be able to replace the available electrochemical batteries in the electronic consumers, electronic vehicles, and many other industries as the general solution for power storage. However, their achievements are still obstructed mainly at the stage of research and development because currently envisioned supercapacitor systems are still not be able to store as much energy as batteries. This may possibly be due to their flexibilities that supercapacitors can be properly tailored to operate for other roles where the available and conventional batteries are disadvantage to serve. On the other hands, supercapacitors also have several other benefitial features that make them preferably appropriate for other applications, compared to those of batteries. For example, supercapacitors possess potential applications, such as larger power capacity, faster charging time, more stable materials, and last longstanding.

For all of these reasons, the research efforts continue to develop novel hybrid composite supercapacitors that become an essential solution to such various applications. It is hoped that this work would further discover the new composite materials to be served as a starting point for developing energy storage in the near future.

1.2 Research Concept

The aim of this dissertation is to utilize computational simulation models based on density functional theory (DFT) with different exchange-correlation functionals in order to investigate, describe, and evaluate the molecular structures and their formations of new hybrid materials as composite electrodes to be used in supercapacitor applications.

In this thesis, we shall focus on the composite electrodes consisting of graphite with transition metal phthalocyanines (TMPcs) attached on its surface. As mentioned in Section §2.1, the TMPcs on the graphite electrodes are expected to enhance attraction of electrolyte ions towards the electrodes. However, its mechanism are still open to discussion, and even structural and electronic features have not yet been elucidated so far. To understand them, we systematically investigate five type of TMPcs, MnPc, FePc, CoPc, NiPc, and CuPc attaching on the graphene sheets (instead of considering the graphite electrode), which would be a good model to simulate the actual interface structure between the TMPcs and graphite with moderate computational cost and reasonable accuracy. The computational procedures are given below.

First, both of the molecule of pristine graphene and also metal phthalocynines will be optimized by deploying the LDA, GGA, and hybrid functionals to determine their molecular strcutures and then compare those with the available experimental data.

Next procedure was to combine the optimized molecule of graphene with each of transition metal phthalocyanines; MnPc, FePc, CoPc, NiPc, and CuPc as an additional layer attracted to graphene sheet. The re-optimization of the interlayered materials are also required before going to the next step.

After both of the layers have been evaluating both of the layers, the setup parameters for calculations were selected according to the previous calculations. The formation of TMPc/graphene were evaualed from their binding energies, and then comparison of binding energies among the TMPc led us to conclusion.

1.3   Computer Software

All of the density functional theory (DFT) described in this dissertation were carried out using the DMol^3 package within the Materials Studio program. It can be emploted to constructed the specific models of electronic structure and energies of atoms, molecules, and surfaces which produces accurate results, while fairly keeping the computational resources at low consumption for an *ab initio* method. It can be used to investigate various systems by deploying DMol^3, including inorganic or organic molecules, metal solids, and material surfaces. With DMol^3, it can be used to predict the structures, binding energies, reactions, thermodynamic properties, and vibrational criteria.

1.4   Units

Most of the computational results are in electron volt unit (eV). If the author has stated beforehand, otherwise, Hartree atomic units (a.u.) is used in equations where $\hbar = m_e = |e| = 4\pi\epsilon_0 = 1$, in which the Dirac constant, the magnitude of the electronic charge, the electronic mass (m_e), and 4π times the permittivity of free space (ϵ_0) are unity. Please see the conversion factors between Hartree atomic units (a.u.) and SI units in Appendix A.

1.5 Outline of Dissertation

In Section §1.1 of chapter 1, as an introduction, we have made some brief descriptions of motivation to conduct this research and develop the composite electrode that aims to use in the field of supercapacitor devices. In the following section, research concept, outline, objectives, and software used in this research have been described.

Chapter 2 is devoted to general backgrounds in our research. We first introduce the fundamentals of supercapacitors to readers, especially focussing on graphite electrodes with enhanced layers for more ion attraction. TMPcs are introduced to be a candidate material for attracted layer applications to realize supercapacitors, followed by previous studies of TMPcs themselves.

In chapter 3, we make a minimal description of theory and methodology for first-principle simulations based on density functional theory (DFT) with three conventional functionals, Local Density Approximation (LDA), Generalized Gradient Approximation (GGA), and a hybrid functional (B3LYP). Our treatment of spin and basis functions adopted in this research.

Chapter 4 reports our numerical results of the five TMPcs (MnPc, FePc, CoPc, NiPc, and CuPc), graphene, and their compounds, obtained from our DFT simulations with the three different density functionals. Computational electronic structures (energetics, molecular geometries, molecular orbitals, spin states) are systematically analyzed and discussed for all the TMPcs to explore the most promising candidate for composite materials in interlayered electrodes.

Chapter 5 finally presents the summary, recommendation, and the further discussions about the possiblities of future works related to this dissertation. For potential prospects of this research directions, the selected complex of TMPc and graphene will be synthesized and produced in laboratory or industrial scale.

Chapter 2

Background

This chapter principally represents the general background of materials that mainly focused to be used as composite electrode in this dissertation. For the first section, it briefly presents a brief information of supercapacitors based on literature reviews in the field of supercapacitor research and development. Followed by the introduction of supercapacitors, in subsection with the fundamental background of both conventional capacitors and supercapacitors are provided. The classification of supercapacitors that based on their electrode materials, the discussion of the various classes and their materials, and represent the different classes typically shaped the order of energy storage attempts will covered in more details in the Appendix B.

Next, graphene is presented in Section §2.2. A brief explanation of structure of graphene and graphite, electronic structure, properties, adsorption, and migration are presented in subsection §2.2.1, §2.2.2, and §2.2.3, respectively.

Finally, Section §2.3 provides the brief knowledge of phthalocyanines (Pcs). Their basic molecular structure of Pc monomer is illustrated in subsection §2.3.1, and §2.3.2. They present in details of different derivatives of transition metal phthalocyanines (TMPcs). The applications of TMPcs are presented in subsection §2.3.3.

2.1 Supercapacitors

The increasing demand of more advanced energy storage with larger capacitance magnitudes, faster charging times, and longer lasting, is increasing notably, and it has predictably become an essential focus of the leading governments and scientific research communities in corresponded to the shift of new technology. In the past decades, there has predictably become a global attention in refining and developing more efficient energy storage in many devices, and that is supercapacitor.

The new emerging technologies have significantly been facilitating the developments in supercapacitors in various aspects, such as overall more efficiency, their electrodes with larger surface area, higher power density, and their longer life cycles. All types of supercapacitors and the conventional capacitors are generally governed by the same fundamental equations, demonstrated in Appendix B.
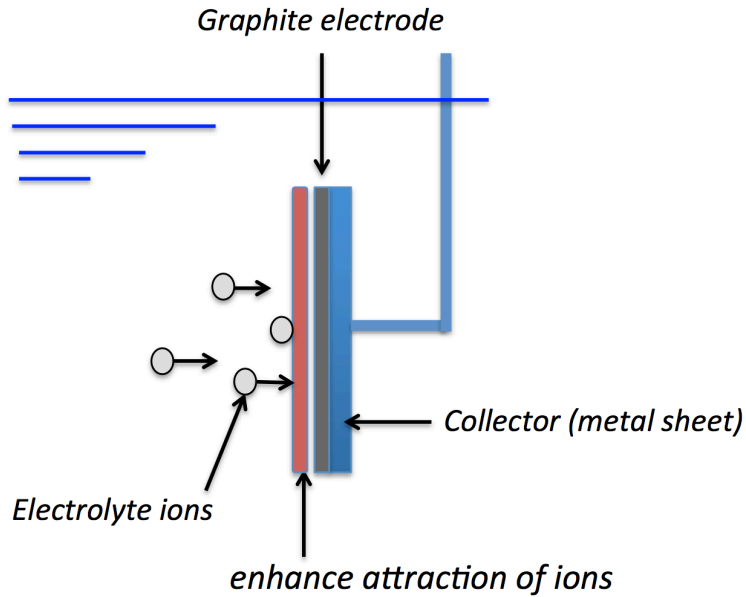
Figure 2.1: Schematic of graphite-based electrode with enhanced layer for more ion attraction.

The notable differences are that supercapacitors have utilized their electrodes with higher surface area materials and dielectrics with smaller gap to reach orders of magnitude in such a way that are greater than currently available capacitors in the industries. The above reasons notably lead them to have higher energy and power densities than normal capacitors and batteries, respectively.

Therefore, supercapacitors are potentially emerged to use in many applications and power systems. Especially, supercapacitors for hybrid electric vehicles or pure EVs power systems, the applications in pulse power, as well as that emergency-backup for power supplies [4, 15, 16]. Notwithstanding the advantages of supercapacitors in the above areas, their production in laboratory or industrial scale, and implementation have been limited at the present time. Burke and Kotz *et al.* suggested that these difficult issues can possibly be overcome in the near future [4, 15].

In general, normal capacitors and supercapacitors can typically be calculated by the same fundamental relationship. The notable differences are that supercapacitors have utilized their electrodes with higher surface area materials and dielectrics with smaller gap are the important keys to consider in order obtaining larger orders of power values [4, 15, 16]. Accordingly, these lead them to take these advantages to reach both in greater energy and power than capacitors and batteries, respectively.

Therefore, the main focus in this research is that to increase surface area of electrode materials with the additional layer attached to the carbon-based one which will also enhance the overall ability to attract more electrolyte ions diffused to the interlayered surface as illustrated in Figure 2.1. The carbon-based electrodes that have been deployed are multilayer graphene sheet or graphite system because graphene-based are known to possess good conductivities, tunable surface area, and also chemical stabilities [17].
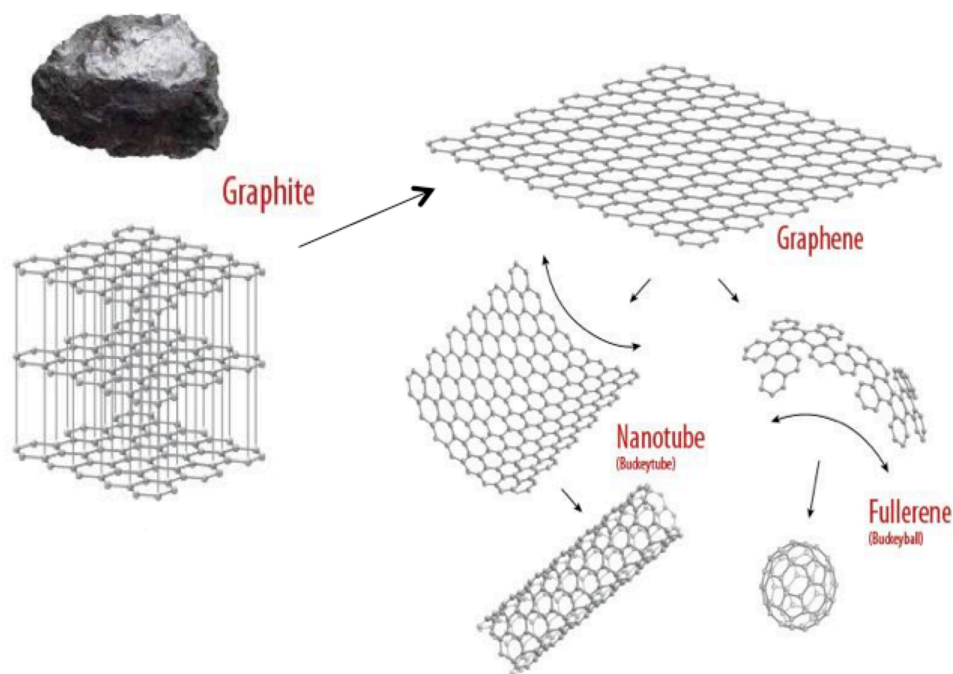
Figure 2.2: Graphene (top right) is the basic tiling of different forms of carbon, such as graphite (left) viewed as stacking multilayers of graphene, carbon nanotube (bottom middle) viewed as rolled-up graphene, and bulkyball (bottom right) viewed as wrapped spherical graphene.

2.2 Graphene

Graphene has become an attractive material of this century because it truly is the first 2D material that entirely made of monolayer of C atoms tiled in repetitive hexagonal lattice. A single C-C bond normally has length of 1.42 Å, similar to benzene ring [18]. It has been seated in the front row as a leading class of other 2D materials. In 2009, C. Q. Sun *et al.* has reported that the C-C bond contracted by up to 30% [18] with respect to the bulk of diamond of 1.54 Å [19].

Graphene is the basic structural formation of many fullerenes, such as nanotubes (CNTs), bulkyball, and graphite as depicted in Figure 2.2. In nature, graphite system consists of multilayer graphene which each single layer is stacked together by the van der Waals interaction between layers. It has become widely attracted attentions for its superlative and remarkable mechanical and electrical properties, ever after the separation of layers successfully in 2004. In 2010, two scientists from the University of Manchester, UK, A. K. Geim and K. S. Novoselov have won the Nobel Prize in Physics from producing, isolating, identifying, and characterizing graphene [20].

In following subsections, brief reviews of electronic structure and properties of graphene are presented. Then followed by the absorption sites and energies of any inserted atoms from periodic table onto graphene sheet. These would additionally provide the useful information for the prediction of preferable sites to attract other metallic molecules or polymers. The migration energies also predict the mobility of inserted atoms, which will be helpful information during the fabrication process of other materials on graphene sheet.
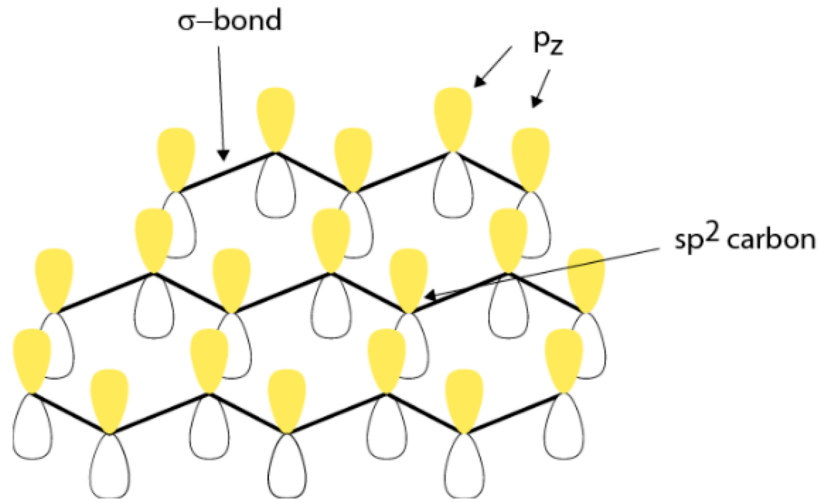
Figure 2.3: Schematic illustration showing the p_z orbitals perpendicular to graphene planar structure and σ bonds between neighboring sp^2 carbon atoms.

2.2.1 Electronic Structure of Graphene

The electronic band structure of a material is able to serve as useful information for describing its physical properties, such as the electrical resistivity and optical absorption. On top of that, it is quite important to understand the operation principles of related solid-state devices, for example, light emitting diodes (LEDs), solar cells, and transistors.

The hybridization of 2D network of carbon atoms in graphene takes a crucial cast in electronic properties. Since a single atom of carbon contains 6 electrons in total so it does exhibit the electronic configuration of $1s^2$, $2s^2$, $2p^2$. Then, all of electrons in the $1s$ orbitals are the core-level electrons which will not be involved in bond formation, on the other hand, those that are leftover in the $2s$ and $2p$ orbitals are the valence electrons. They will definitely be involved in bond formation. These valence electrons can be hybridized and share electrons in 3 possible ways. As a result, the carbon atom can have 2, 3, or 4 adjacent atoms that will also be available for the bond formation, with the electrons forming the hybridized orbitals sp, sp^2 and sp^3, respectively.

In graphene sheet, the carbon atoms are sp^2 hybridization that they have 3 in-plane neighbors which each form a σ bond as demonstrated in Figure 2.3. These bonds are created from covalent character and the acquired crystal structure form the planar hexagonal structure, as depicted in Figure C.6(a). Because of this σ bond formations, it has caused a $2p$ orbital, i.e., $2p_z$, to be left out and perpendicular to the graphene plane. As a result, it will get involved in the bond formation so the adjacent $2p_z$ orbitals interact to form the π band of graphene quite weakly. It also contains the valence electrons that have already been delocalised. From theoretical calculations [21], the electrons in this band are behaving like relativistic particles, or as the massless Dirac fermions, which are mainly responsible for the conductive property of graphene superatively.

In Figure 2.4, it demenstartes electronic band structure of graphene. In the same image, a
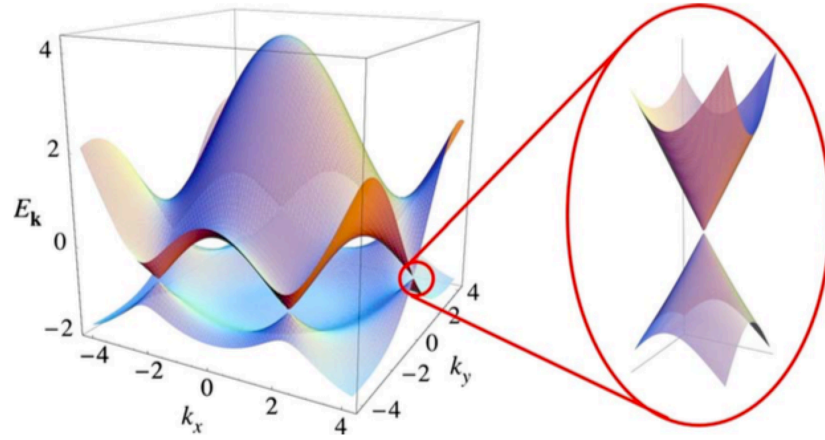
Figure 2.4: Electronic dispersion of graphene plane with zoom-in on the right for band energies of graphene near Dirac points, adapted from reference [1]. Copyright 2009 American Physical Society.
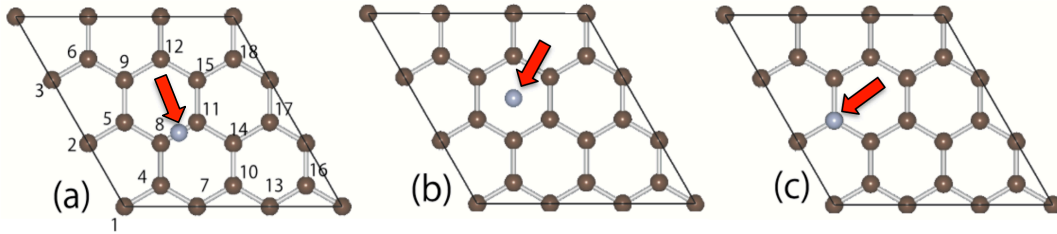
Figure 2.5: Graphene with 3×3 supercell adsorption sites. (a) Bridge site (B-site) is located between C-C bond. (b) Hexagonal site (H-site) is at the center of benzene ring. (c) Tetrahedoral site (T-site) is vertically above a carbon atom, adapted from [2].

zoom-in shape shows the closer Dirac points at the K or K' point in BZ. The energy dispersion is similar to the energy of ultrarelativistic particles described as massless Dirac equation. The immediate cyclotron mass that depend on electronic density [21] defined as

$$m* = \frac{1}{2\pi}\left(\frac{2}{3}\right) \tag{2.1}$$

2.2.2 Adsorption on Graphene

This subsection represents the adsorption mechanism of adatom on graphene based on computational approach of density functional theory. All results in this section containing the reported work done by Nakada and Ishii [2]. The computational results were calculated at three adsorption sites, bridge (B-site), hexagonal (H-site), and tetrahedoral (T-site) as illustrated in Figure 2.5. The adsorption energy can be obtained from the relationship

$$E_{bond} = (E_{graphene} + E_{adatom} - E_{total}) \tag{2.2}$$

where E_{bond} is the binding energy of adatom on graphene plane. $E_{graphene}$ is the total energy of monolayer graphene, and E_{adatom} is the total energy to isolate adatom.

The calculations are performed on periodic elements are presented in Figure 2.6 for the calculation results. That demonstrates the magnitudes of bond energies of various adsorbed atoms with different metastable sites on graphene plane. In depicted periodic table, different coloring is distinguishably used as a method to indicate the most stability of each adatom. Green, pink and yellow are corresponded to B-site, H-site, or T-site, respectively. The numbers indicate values of adsorption energy in eV for each table site, as shown in Figure 2.6.

The results from the Figure 2.6 can be implied that the transition metal elements adsorbed mostly at the H-site. Then for non-metallic atoms, they prefer adsorption site at B-site. For adatoms with only 1 valence electron, such as H, F, Cl, Br, and I, their most stable site is at T-site. Moreover, the magnitude of the adsorption energy of metallic atoms is very large compared to other groups. While non-metallic elements, such as C, N, and O have the largest adsorption energy. The bond energy for the transition metal elements indicates a growing trend along with increasing number of d electrons. As the number of d electrons increases to more than half occupancy, the bond energy will decrease causing by the shifting down of the d orbitals. The metal element adsorptions also have large bond energy but this state is unstable because it is produced in a local unbonded band at Fermi level with the large number density of states.

The differences of adsorption energy between three adsorption sites are additionally very small relatively to the adsorption energy is small amount. On other hand, the adsorption energy is quite high in magnitude for non-metallic adatoms, such as C, N, or O atom. There are significantly large differences in the adsorption energy between sites that are larger than 3.0 eV. However, when the adatom is C, fewer differences between the adsorption energies of T-site and B-site are presented.

The bond distances between graphene and adatoms is shown in Figure 2.7, where red are the lengths that are smaller than 2 Å, white are the lengths that greater than 2 Å. The transition metal atoms adsorbed to graphene sheet on very closed range of distances. In this case, bond distance is the average length between adatom and the graphene plane. If bond distance between adatom and graphene is really long, their trendency of binding energies are decreasing. In other words, the adatom are physically bonding located at far apart from graphene plane.

2.2.3 Migration on Graphene

In the above subsection §2.2.2, the adsorption energy on graphene was discussed. All of this reported work is also reported by Nakada and Ishii [2]. They have mainly discussed about the migration energy, which is an energy needed to shift atom to other sites on graphene plane. At room temperature, if atom possesses high migration energy, it will not be able to be mobile that easily, but being fixed at a paticular location as mentioned previously. In contrast, if the migration energy is rather small, the adsorbed atom can be mobile with less difficult even under the room temperature condition.

The migration energies of adsorbed atoms is depicted in Figure 2.9. From the calculated

Figure 2.6: The most stable sites of adsorbed atom on graphene plane, where the magnitude is the bond energy of each element. Color codes: B-site indicated in green, H-site indicated in pink, and T-site indicated in yellow, adapted from [2].

H																	He
1.49																	
Li	Be											B	C	N	O	F	Ne
1.62	2.93											1.72	1.65	1.62	1.59	1.87	
Na	Mg											Al	Si	P	S	Cl	Ar
2.22	3.21											2.04	2.03	2.09	2.08	2.56	
K	Ca	Sc	Ti	V	Cr	Mn	Fe	Co	Ni	Cu	Zn	Ga	Ge	As	Se	Br	Kr
2.58	2.14	1.76	1.56	1.47	1.42	1.38	1.38	1.42	1.47	2.03	3.02	2.11	2.16	2.22	2.25	2.78	
Rb	Sr	Y	Zr	Nb	Mo	Tc	Ru	Rh	Pd	Ag	Cd	In	Sn	Sb	Te	I	Xe
2.74	2.37	2.00	1.74	1.66	1.59	1.57	1.62	1.71	2.08	2.42	3.18	2.35	2.42	2.46	2.49	3.26	
Cs	Ba	La	Hf	Ta	W	Re	Os	Ir	Pt	Au	Hg	Tl	Pb	Bi			
2.84	2.49	2.07	1.85	1.65	1.60	1.58	1.61	1.70	2.12	2.41	3.13	2.48	2.53	2.57			

■ less than 2.0Å
□ more than 2.0Å

Figure 2.7: Distance between the adatom and grapehene plane. The transition metal atoms adsorbed to graphene sheet on very closed range. Color code: the close distance of adatom that is less than 2 Å indicated in red, re-printed from [2].
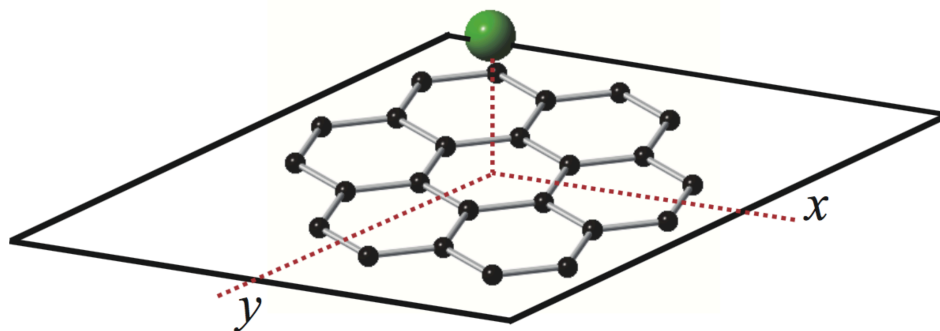
Figure 2.8: Schematic of the migration energy required for atom adsorbed on graphene plane are able to move from one site to another over the plane, re-printed from [2].

1	2	3	4	5	6	7	8	9	10	11	12	13	14	15	16	17	18
H 0.60																	He
Li 0.30	Be 0.02											B 0.12	C 0.25	N 1.00	O 1.02	F 0.45	Ne
Na 0.13	Mg 0.02											Al 0.05	Si 0.05	P 0.45	S 0.46	Cl 0.02	Ar
K 0.12	Ca 0.07	Sc 0.34	Ti 0.61	V 1.05	Cr 1.45	Mn 1.26	Fe 0.97	Co 0.77	Ni 0.40	Cu 0.03	Zn 0.02	Ga 0.03	Ge 0.07	As 0.20	Se 0.23	Br 0.00	Kr
Rb 0.09	Sr 0.04	Y 0.12	Zr 0.39	Nb 0.83	Mo 1.47	Tc 1.40	Ru 0.96	Rh 0.39	Pd 0.06	Ag 0.01	Cd 0.01	In 0.02	Sn 0.03	Sb 0.03	Te 0.09	I 0.00	Xe
Cs 0.10	Ba 0.05	La 0.18	Hf 0.23	Ta 0.60	W 1.17	Re 1.23	Os 0.75	Ir 0.15	Pt 0.19	Au 0.03	Hg 0.01	Tl 0.00	Pb 0.01	Bi 0.00			

Legend:
- more than 0.50 eV
- under 0.50 eV more than 0.30 eV
- less than 0.30 eV

Figure 2.9: The most stable sites of migration energy. Green color is more than 0.5 eV indicating the more stability at fixed location than other elements, re-printed from [2].

results by Nakada and Ishii [2], it was reported that inserted atom divided into two categories; first, fixed site, and second, mobile adatoms. They are tentatively distinguished apart by magnitude of migration energy at 0.5 eV. For example, below 0.5 eV, adatom can move easily at the room temperature. For above 0.5 eV at the room temperature, it will be fixed at its stable site.

$$R = R_0 exp(-E/k_B T) \qquad (2.3)$$

where R is the rate of hoping of adatom per second, it can be denoted with the above relationship. E in this formula is migration energy, R_0 is a pre-factor, T is temperature, and k_B is the Boltzmann constant. Such an example, if graphene plane have more than 1×10^6 atoms, migration energy of 0.5 eV is corresponding to hoping of at least one atom per second. In 1996, Ito and Shiraishi have reported in the their previous work for performing a kinetic Monte Carlo (kMC) simulation of molecular beam epitaxy (MBE) [22]. Some parameters, such as the hopping energies obtained by first-principles calculation were used. Ito and Shiraishi used DFT method to find migration energies because many researchers have already performed their calculations in their former work by the same method. The energy can simply be obtained by deploying the contouring of total energy as a function of adatom sites on surface.

According to the calculation by Nakada and Ishii [2], for some transition metals (TM), the migration energy at their most stable sites are too high. As a result, these TM atoms are strongly adsorbed on graphene and too difficult to change their positions over graphene plane; for example, Mn, Fe, and Co. In contrast, the migration energies of many elements, such as Cu, Pt, and Au, are lesser so adatoms can be mobile easily over the surface. At low profiled temperature, the $3d$ transition elements are polarized so their calculations were performed without

magnetism that becomes average about a spin.

During its adsorption process in some cases, the adatom may disturb the structure of graphene. In spite of that with H-site adsorption, the graphene structure has not altered, especially for some metals adsorption. For consideration, it is necessary and should take into account that during the growth of a material on graphene plane that structure will not be distorted by this kind of H-site adsorption.

As a result, for the non-magnetic calculations, As the adsorption energy is declining, but its energy still at the level that higher than the physical adsorption, graphene plane will keep its consistency and will not be distorted with the adsorption on the H-site. For example in the case of their calculation on Ti adatom, it is also one of transition metal with its migration energy of 0.61 eV, referring to Figure 2.9, and its bond energy is about 3.30 eV, referring to Figure 2.6. The migration energy of Ti adatom is greater than 0.5 eV. So when it is adsorbed on graphene, even though their results are almost same as non-magnetism, the migration energy is lower than that of non-magnetic of the $3d$ transition metal adsorption [2].

2.3   Phthalocyanines

Phthalocyanines are famous colorants that have widely been known for many decades. The name phthalocyanine is from the two Greek words: 'naphtha' and 'cyanide,' which mean 'rock-oil' and 'dark blue,' respectively. In 1907, the first phthalocyanine was accidentally discovered during a study of the properties of 1,2-cyanobenzamide by Braun and Tcherniac [23, 24]. After that, phthalocyanines (Pcs) have become a major pigment in the dye industries due to the varieties in their unique color, high stability, non-toxicity, and low manufacturing cost. In addition, they have also been facilitated in the organic semiconductors. Their strong Q-band absorption in the ranges from 600 to 800 nm [25] and outstanding photo efficiently induced charge generation promoted the applications in the photoreceptors in laser printers [24].

2.3.1   Structure of Phthalocyanines

Phthalocyanines (Pcs) are a class of macrocyclic compounds possesses bivalent, tetradentade, planar, 18 π-conjugated electron aromatic ring systems. They are typically composed of four pyrrole units that also linked by the four N=C groups of pyrrole ring. They have four aza bridges and four phenylene rings.

Approximately seventy different elemental ions can be placed into the central cavity of Pcs, and their chemical and physical properties are greatly influenced by selected ion placed at the central cavity. Pcs usually exist as a Pc^{2-}, which holds many ions tightly with an oxidation state of +2, such as Cu^{2+}, Co^{2+} and Fe^{2+}. It is very difficult, or even impossible, to remove most of the metal ions from the central cavity of Pcs without destroying whole macrocycle structure [26]. Its basic structure of Pcs is demonstrated in Figure 2.10.

Between the time frame of the years 1930-1950, the full elucidation of the Pc chemical structure was determined and its X-ray spectra, absorption spectra oxidation and reduction, catalytic properties, magnetic properties, photoconductivity, and many more physical properties
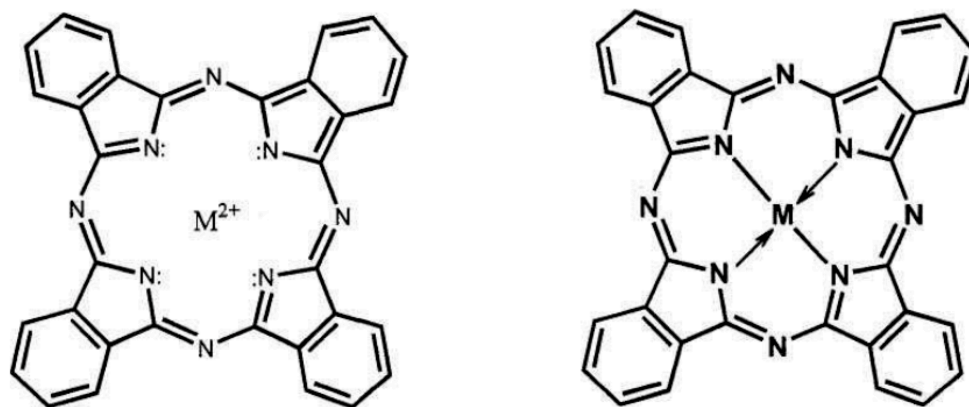
Figure 2.10: Molecular structure of phthalocyanine, where M in the center of the macrocycle represents the metal ion.

have intensively been investigated. As a result of these studies, it was concluded that Pcs are highly colored, planar 18-π electron aromatic ring systems similar to porphyrins.

2.3.2 Metal Phthalocyanines

Derivatives of phthalocyanines have been applied in many industries as functional materials according to their upholding properties are efficiently encouraging the abilities of charges transfer. In a central cavity of the molecule in the phthalocyanine monomer, it has been widely known for its capability of residing various atomic ions. It can accommodate even two H atom, H_2-Pc, which called a metal-free phthalocyanine [27]. The porphyrazine groups in phthalocyanine derivatives are influentially affected by π electrons [28, 29]. By introducing metal phthalocyanine (MPc), it is a phthalocyanine is containing metal ions in the central cavity [27], as depicted in Figure 2.11. Depending on the different central metal cation, the appearance of each MPc can be noticeably changed from dark blue to metallic bronze to green in its solid state.

The macrocycle generally exists as a dianion (Pc^{2-}). Therefore, MPcs are basically categorized into five groups based upon the central ions:

i) the metal free MPc, H_2Pc,

ii) monovalent MPcs, such as Li_2FPc,

iii) divalent MPcs, such as MnPc, CoPc, CuPc,

iv) trivalent MPcs, including AlClPc and AlOHPc. In this case, M can be a metal halide or also a hydroxide,

and v) tetravalent MPcs: TiOPc, $SiCl_2Pc$, and $Si(OH)_2Pc$. They belong to metal oxide, dihalide or dihydroxide. Many metal cations, such as Cu^{2+}, Zn^{2+}, and Fe^{2+} are held tightly with Pc to form planar structure [30, 31] without any distortions of macrocycle. However monovalent, trivalent, and tetravalent metal cations, and other large divalent metal ions, for example Pb^{2+}, will protrude from the plane of Pc, cause some distortions, or form a non-planar structure [32].

Since the discovery of MPcs family after 1990s, they have been widely utilized for dye and pigment applications in textile industries and other materials, i.e., paper. The substituted
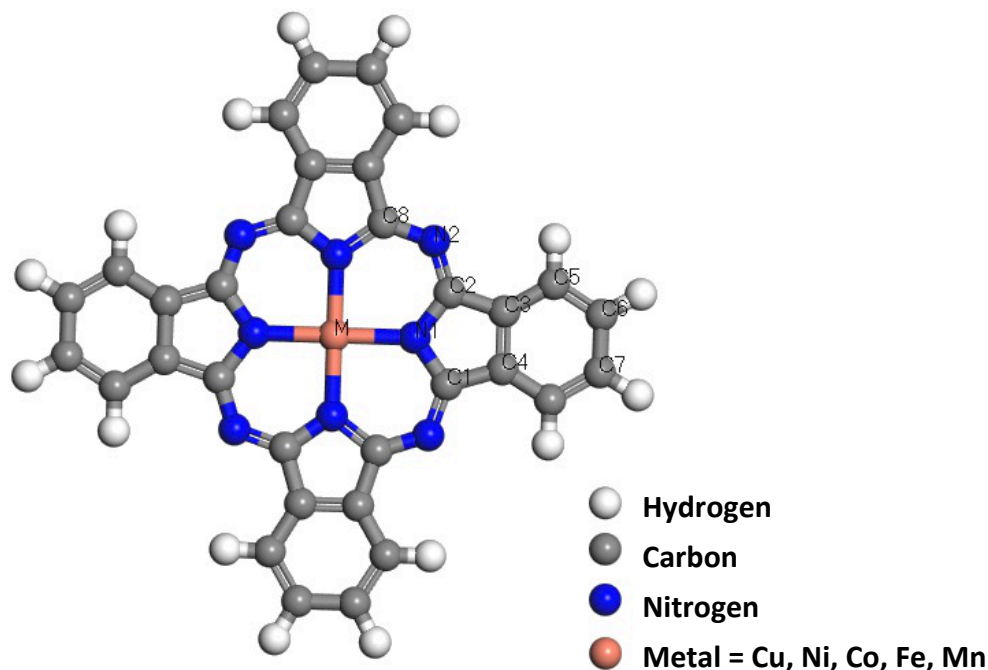
Figure 2.11: Schematic view of the transition metal phthalocyanine (TMPc) monomer, where the central cavity can be accommodated by Mn, Fe, Co, Ni and Cu.

metal ions in MPcs have highly impacted and caused color to change during the redox chemical reaction [33]. Because of their valid chemical stability and changeable shades, MPcs have the outstanding potentials in many applications, such as also being used in organic electronic devices [34–36], solar cells [37], conductors [38,39], photoconductors [25,40], gas sensors [41, 42], catalysts [25,43–45], and other functional chromophores [46]. However, on the downside, they have some disadvantages for poor solubility in organic solvents, and this may have leaded one of the reasons that less usages as functional materials.

The computer generated 3D model of the MPc monomer is depicted schematically in Figure 2.11. The general structure of MPc, as same as a regular molecule of Pc, is composed of coordinated metal ion located in the center cavity inclosed by organic macrocycle of C and N atoms. From outer rings of 4 benzene groups are attached to each group of pyrrole rings, which connected together by 4 additional N atoms. The regular monomer is mostly a planar structure with D_{4h} symmetry. Due to the modification of central ions or macrocycle, MPcs can be customized into various compounds and different molecules.

The central cavity of a Pc monomer is able to accommodate many different metal ions. By introducing the metal cations, for example, Fe^{2+}, Ni^{2+}, Co^{2+} into the central cavity of Pc molecule, it will greatly influences its entirely physical and chemical properties. For instance, when a metal cation is introduced to the Pc molecule, the macrocycle exists as dianion (Pc^{2-}) and can be oxidized or reduced to different oxidation states [26, 47]. The redox reaction of MPcs is affected by the interaction of the phthalocyanine monomer and substituents of central metal [48]. The electrons around the closed system influenced the porphyrazine group in the MPc molecule with the available 18-π electron system [29, 49].

Many metal atoms can be accommodated perfectly into the central cavity of Pc monomer without the destruction of the planar structure of the Pc. Nevertheless, in some cases, several substituents of metals have bigger sizes in their ion forms than the available space in the central cavity of the Pc. As a result, they have even caused some distortions and displacements to the non-planar structure of the macrocycle.

There are generally two types of possible bonding in MPcs: electrovalent and covalent [47, 50]. According to X-ray analysis, the central metal ion with a +2 oxidation state is bonded to two nitrogen atoms by covalent bonds, and to the other two nitrogen atoms by coordinate covalent bonds, referred to Figure 2.10. Metal cations with an oxidation state of +1 can also be incorporated into the central cavity. The bonding between the central metal atom with a +1 oxidation state, i.e., Li^+, K^+, Na^+, and the four nitrogen atoms of the macrocycle is naturally considered to be electrovalent. It is characterized by its ionic character and relative weakness.

The central N atoms can ligate two M^+ atoms. Since both of these two cations cannot concurrently be accommodated in the central cavity, the metal ions protrude from the planar structure. Pc and other alkali metal derivatives also possess high solubility in polar organic solvents [26, 47]. Due to their strong covalent and coordinate covalent bonding between the Pc and the metal ion, the metal cations in the central cavity cannot be removed without destruction of the macrocycle structure.

1. **Manganese Phthalocyanine**

   Most metal-substituted Pcs have planar molecules. In also the case of Manganese phthalocyanine (MnPc), the central metal atom is manganese (Mn) atom, which is in a +2 oxidizing state. The Mn center has a formal $3d^5$ electronic configuration, and expected to approach to Fermi level [51, 52]. Monomer structure of MnPc is depicted in Figure 2.11 where exhibits the arrangement of discrete, planar MnPc molecule. Furthermore, MnPc is also well known for its magnetic molecule [53].

   The main restricted factor for processing and applications is the low solubility in common organic solvents, similarly to the other MPc family. Substitution in the periphery of the macro cycle reduces the strong π-π interaction between the rings and that would help to achieve highly soluble compounds. In contrast, the electrochemistry of MnPc has received a good attention from many researchers [33, 54–57], and that may involve both the central Mn atom and the Pc ring. The electronic structures of the oxidized and reduced species were analyzed through their optical spectra [54–56], but there are no definite conclusions about the ground-state configurations of the ions [51].

   The magnetic properties of MnPc complexes has been studied by group of J. Janczak *et al.*. They reported the potentials of MnPcs in applications, such as biological oxidative processes, catalysts, sensors and coordination chemistry [10]. The main advantage for using MnPc complexes as organic semiconducting materials is that their molecular structures can readily be modified, and hence, their electrical and optical properties [58]. Similar to the case of NiPc, MnPc has previously been studied its performance in lithium battery which it is satisfactory to increase the energy of the battery [59].

2. Iron Phthalocyanine

Transition metal substituted Pcs (TMPcs) as mentioned several times in the previous section that they have already been utilized for specific electronic devices. Among TMPcs, iron phthalocyanine (FePc) has previously been deployed for organic detection and effective catalysts [60–64]. Any practical MPc applications are relatively involved with their electronic structures. Bialek *et al.* have theoretically performed the first principle calculations on the electronic structures of FePc monolayer [65]. The experimental investigations of FePc were studied for many years by applying the inverse photoemission spectroscopy (IPES) [66, 67], by photoemission spectroscopy (PES) [68, 69], and by the ultraviolet photoelectron spectroscopy (UPS) [70, 71].

The crystal formations of FePc molecule have 3 different forms, and among their polymorphic forms, β-phase is mostly their well known stability, where its intermediate electron spinning in ground state of FePc is $S = 1$ [11] used to study a single layer on behalf of FePc thin film, similarly to the case of NiPc [72]. The molecule of FePc is schematically presented in Figure 2.11.

3. Cobalt Phthalocyanine

Cobalt Phthalocyanine (CoPc) complexes have potential as functional materials for gas sensors [73, 74], effective catalysts [63, 75–78], and also electrocatalysts [79]. The applications of CoPc could be more efficient than that of other TMPcs according to their high abilities of charge transfer [49], and magnetic properties of central Co ion [80]. Applications, such as low dimensional molecular magnet, have considered CoPc filling for this part. However, CoPc complexes have been applied in only a few applications, similar to other TMPcs in its family, they have poor solubility in common organic solvents or even in water. Y. Pan *et al.* [77] have found that by modifying peripheral benzene rings in Pc molecule with some appropriate functional groups, this could greatly assist the solubility of Pc in water.

CoPc complexes are outstanding electrochemical catalysts in oxidation process in sulfur compound, where the ground state of CoPc catalyzed redox process, and is the result of charge transferring from the sulfur substrates to O_2 coordinated to Co(II) ion. Structure of CoPc monomer is illustrated in Figure 2.11.

In contrast, several researchers have investigated and found that Pcs can adsorb stably on graphitic electrodes [81], similar to the case of NiPc, and further studied on the electrochemical catalysts characteristics on the surface [45, 82–85]. For example, J. H. Zagal *et al.* reported on redox chemistry of CoPc complexes adsorbed on graphite surface [86].

Main purpose of this research is to study the influence of CoPc adsorbed on graphene plane, to learn more about their formation between CoPc and graphene. In particular, it is interesting in exploring the possibility of CoPc on the graphene as one of the candidates for the hybrid capacitor.

4. Nickel Phthalocyanine

TMPcs and metal-free Pcs have already been utilized as active thin films in various applications as mentioned previously in the section §2.3.2, i.e., gas sensors [87–89], photo capacitive and resistive detectors [25, 40], OLEDs [90, 91], organic thin film transistors (OTFTs) [36], and molecular electronics materials [92]. However, among these various MPc materials, nickel phthalocyanine (NiPc) has considerably received less attention than the other TMPcs.

The NiPc molecule consists of 57 atoms, $NiC_{32}N_8H_{16}$, and it also has D_{4h} symmetry. A Ni atom can also be another substituent, and it can fit perfectly into the central cavity of the Pc monomer without any deformations of the planar structure, similar to the case of Cu atom, as shown in Figure 2.11. The structural properties of NiPc have been investigated by some research groups to explore its potential, structural and morphological characterizations which are considered as a prerequisite in order to gain the insight information [93, 94].

The properties of NiPc are greatly affected by its production processes. The influent techniques are, such as the deposit method on the target substrate, the conditions of deposition, and the temperature of the heat treatment. The re-arrangements of thin films are occurring with varied temperature on substrate [95]. It was found that the properties of NiPc as the substrate temperatures increasing, their grain sizes are also changing. Annealing process is used as a main method to improve the qualitative crystal and also to control the defected structure as desire [95] because the morphology and structural properties in some TMPc materials may have changed during the thermal annealing process [93].

In the previous work reported by Temofonte *et al*. [89], they investigated structural properties of NiPc for using as semiconductor gas sensors, and they have found that charge-transfer interactions occurred after introducing a molecule into the NiPc system which resulted in an enormous increasing in surface conductivity. The charge transfer increases the conductivity by greatly increasing the number of charge carriers, which for phthalocyanines are holes. Therefore, film of NiPc can considerably be used not only as a semiconductor gas sensor [42, 89] but also as a conductivity enhancement [96]. Brito *et al*. [97] also reported their previous work on the investigation of the surface morphology and conductivity of nanostructured layer-by-layer (LbL) films from derivative of NiPc alternated with carbon allotropes, MWNTs.

NiPc is also an organic semiconductor that mounts alternative single and double bonds. In the previous work by Joseph *et al*., they has investigated the changes in the optical properties. The optical band gap of NiPc thin films deposited at various substrate temperatures [98].

The battery of lithium-thionyl chloride ($Li/SOCl_2$) has practically high voltage and energy [59]. Many researches [99, 100] on $Li/SOCl_2$ battery utilizing TMPc as cathode catalysts have been conducted. The energies of $Li/SOCl_2$ battery with NiPc are tentatively 60% up to 100% higher than the practical without this NiPc complex [59]. Thus, in

the case of hybrid capacitor with conductive polymer and activated carbon, the complex of graphene/NiPc might be one of the candidates among other TMPc derivatives.

5. **Copper Phthalocyanine**

Copper phthalocyanine (CuPc) is a well-known TMPc. It is also one of the simple derivatives of TMPc materials yet. In a molecular solid form as depicted in Figure 2.11, CuPc is a highly stable organic material [101]. It has been used in numerous applications in many industries, such as switches [102], light emitting diodes (LEDs) [88] (or organic light emitting diodes (OLEDs) [90, 91]), solar cells [37, 103], gas sensors [87–89], Organic field-effect transistors (OFETs) [104, 105], and various molecular electronics [42, 92, 106]. CuPc has especially shown its physical and chemical properties as a class of macrocyclic planar compounds. In the case of electronics, the properties of the CuPc interact with either organic or other inorganic materials normally dominate the performance of CuPc-based devices. Numerous experiments on its optical, magnetic, and electric properties have been conducted to understand the interfaces of CuPc with other materials [88, 91, 107–110].

CuPc can participate in chemical interaction influentially by either just the central Cu atom, N atoms, or p-electrons [111]. Several works have been reported for electron spectroscopy of the core and the valence electronic states [112–114]. They accomplished to investigate the formation between the interfaces of CuPc films on several metal substrates. This can lead to the insight mechanism of negatively charge transfer between CuPc films and metal substrates [115].

Because CuPc is a complex of a macro-cyclic compound with an extended π density, in previous work by J. H. Zagal *et al.*, they have reported that CuPc can be adsorbed on graphite system and also other fullerenes [45]. In electrochemical processes of charge transfer, CuPc has potential as a catalyst mediator for making active electrodes for electrochemical sensors. It can be used to detect variety of organic applications [45]. Recently, it was discovered that CuPc could enhance the electrical properties of graphene for using as a high quality and transparent conductive film [116].

Ren *et al.* previously studied the interaction between physisorbed CuPc molecules and graphene, and also their charge transfer mechanism at the interface [117]. Thus in this research, it aims to further investigate the molecular structure of graphene/CuPc to gain an insight knowledge of the properties of this composite material as one of the candidates for hybrid capacitors.

2.3.3 Applications of Transition Metal Phthalocyanines

The TMPcs have been used in various applications as presented previously in each TMPc mostly in organic electronic devices. These are due to their high value in charge transfer [27, 50, 118–120]. The functions of TMPcs are influentially based on their abilities in this charge transfer because in their practical molecular structure, they have conjugated 18 π electrons available. TMPcs are approximately 25% of all artificial organic pigments [121]. For example, dyes of

CuPc are manufactured by adding sulfonic acid functions for solubilizing proposes. These dyes are also use in numerous industries of dyeing textile and also extensively in the paper industries.

In addition, Pcs are well known to use in the CD-R media manufacturing because phthalocyanine dye in CD-R products is considered to be an improved version to original cyanine dye. Cyanine structure has less stability in its normal form than phthalocyanine. The data recorded on CD-Rs coated by phthalocyanine will endure for more than a century. While cyanine-based disks only stand for 2 decades. Pc dye has been optimized for propose in high-speed read and write together with the development in advanced laser technology. Then, it can etch the precise pits on the disk surface, resulting in more accurate written disc at high speed.

Many studies by research groups suggested Pcs as components for organic electronic applications [102, 122–124], and recently enhanced the electric properties of graphene [125]. Attempts with the combination of Pcs and graphene-based electrodes for battery and supercapacitor improve the qualitative devices. Pcs offer several benefits over some metals or metal oxides due to their flexibility with customized options, and low-price production [126].

Table 2.1: Table of summary: the usage of phthalocyanines as attached layers in electrode applications. The promising candidate for the layers realizing enhanced ion-attraction.

Phthalocyanine	Effect	References
Octacyanophthalocyanine	Increased life cycle	[127]
Fe/Cu phthalocyanine	Higher discharge voltage	[128]
Fe octacyanophthalocyanine	Higher energy density, better capacity	[129]
Mn and Ni phthalocyanine	Increased energy	[59]
Co phthalocyanine	Increased discharge energy	[130, 131]
Co phthalocyanine	Increased capacity and voltage of discharge	[132]
Co phthalocyanine	improve the charging performance	[133]

According to the review articles, Pcs employed as attached layered electrodes in batteries and supercapacitors for improving the qualitative properties are reported [59, 127–133], as summarized in Table 2.1. They have various effects on voltages, stabilities, life cycles, energies, capacities, and charge performances. Because TMPc is a complex of macro-cyclic compound with π electrons extended, it can be attracted on graphite system and other fullerenes [45]. It was also reported that TMPc could enhance the electrical properties of graphene for using as high quality transparent conductive film [116].

Liu *et al.* synthesized and investigated phthalocyanine/graphene composites for electrocatalytic performance in Li/SOCl$_2$ battery. Their results indicate that Pc/graphene composites have satisfactory catalytic activity with improve the capacity of Li/SOCl$_2$ battery by 24.65 - 83.72% [134]. Therefore, it is investigated the electronic structures of TMPc/graphene to gain insight knowledge of its properties of this composite material.

The interaction between organic molecules and surfaces technologically plays a central role in many applications, such as molecular electronics, organic solar cells, and biosensors. For

instance, organic solar cells are based on organic molecules and their interfaces with solid electrodes and have attracted growing attention in according to their potential low-cost applications, environment friendly and flexible large-scale photovoltaic devices. Their energy conversion efficiency depends sensitively on the interface structure and electronic coupling between molecules and the electrode surface and between organic layers, and has increased significantly over the past decades due to the invention of donor-acceptor heterojunctions [135–138]. Much current research has focused on understanding and controlling the interactions at the organic/inorganic interface, [139–141] with a great deal of effort devoted to growing high-quality organic thin films by manipulating molecular orientation on solid substrates in order to enhance light absorption, control the type and concentration of interface carriers, and improve electron transfer at the interfaces [142–145].

TMPcs and their derivatives, a class of aromatic compounds and a major component in various types of organic solar cells, received great attention during the past decade. TMPc molecules not only absorb in the red region in light spectrum, but are also highly stable organic semi-conductors, which makes them suitable for energy conversion in organic solar cells. TMPcs have often been used as an electron-donor material in contact with materials that have high electron affinity such as the fullerene C_{60} [146, 147]. A sizable charge transfer occurs from metal substrates such as Al, to CuPc at the metal-organic interface [148, 149], while little charge transfer was noted at the interface of CuPc and highly oriented pyrolytic graphite (HOPG) [108, 150]. In contrast, a thin film of copper hexadecafluorophthalocyanine, $F_{16}CuPc$, is a promising n-type π-conjugated organic semiconductor [146, 151] employed as an electron acceptor. The devices based on a CuPc/F_{16}CuPc p-n heterojunction have been fabricated for photovoltaic applications [152].

Graphene, an atomically flat monolayer of C atoms arranged in a honeycomb lattice has emerged as promising materials for electronic devices according to interesting physical properties [1, 20]. With the rapid development of graphene technology in the past few years, high quality of graphene film can be produced in large scale and can be precisely controlled. Therefore, it is highly promising to use graphene and its derivatives as, for example, a nanoscale electrode [153], to assist donor/acceptor molecular assembly and carrier transfer. In addition, as one atomic layer of C atoms, graphene is the simplest model to explore the interactions between layers of organic molecules and the electrode surface in thin-film based devices.

Chapter 3

Theory and Methods

This chapter presents a brief background of theoretical methods used in this dissertation. It mainly centers on density functional theory (DFT) and its related concepts. For the DFT method, it first reminds about the basis of DFT in Section §3.1. In this dissertation, it would particularly focus on the exchange-correlation energy and on some approximations for it as summarized in Section §D.3. A presentation of selected exchange-correlation (XC) functionals of the local density approximation (LDA), the generalized gradient approximation (GGA), and a developed hybrid functional, are provided in following subsection §D.3.1, §D.3.2, and §D.3.3, respectively. The core treatment used in this work is provided in the Section §3.4. For more details of each section, they are presented in Appendix D.

3.1 Density Functional Theory

The problems for the calculations of the full many-particle are intractable for all systems is obviously needed to reformulated into much simple systems. Then, the next encountered problem will be to solve the famous Schrodinger equation. Hohenberg and Kohn managed to find the alternative way to obtain the ground-state electron density of the system and determine ground-state energy [154]. They state that it can express the energy of many-body systems as a functional of density. The density functional theory (DFT) is principally based on this theorem.

For a non-relativistic system, the many-particle Schrodinger equation is demonstrated in a short form as

$$\hat{H}\Psi = E\Psi \tag{3.1}$$

where $\hat{H}$ is the Hamiltonian operator. The total energy of the system in state Ψ is expressed as

$$E = \langle \Psi | \hat{H} | \Psi \rangle = \langle \Psi | \hat{T} | \Psi \rangle + \langle \Psi | \hat{V}_{int} | \Psi \rangle + \int d^3 \vec{r} V_{ext}(\vec{r}) n(\vec{r}) \tag{3.2}$$

Within energy for density as a functional is at its lowest; for example, function of density in this

particular case, as follows

$$E[n] = \min_{\Psi \to n(r)} [\langle \Psi | \hat{T} | \Psi \rangle + \langle \Psi | \hat{V}_{int} | \Psi \rangle] + \int d^3\vec{r} V_{ext}(\vec{r}) n(\vec{r})$$

$$\equiv F[n] + \int d^3\vec{r} V_{ext}(\vec{r}) n(\vec{r}) \tag{3.3}$$

In order to achieve ground-state energy of such target system, the equation 3.3 should be minimized with respect to densities $n(\vec{r})$ with all possibilities. $F[n]$ is a self-sufficient functional of external potential V_{ext}. In order to find an actual expression $F[n]$, it is corresponding for solving many-particle in the Schrodinger equation. And on account of that, the new approach proposed by Kohn and Sham [155] has helped to simplify the DFT, which will be demonstrated in the next section §D.2.

3.2   Kohn-Sham Equations

While Hohenberg and Kohn reformulated the problem of the many-particle Schrodinger equation into a functional of electron density, Kohn and Sham dealt with puzzle of deriving an equation for $F[n]$ by re-framing the interacting many-particle problems into the non-interacting systems. On the account of the kinetic and Coulomb energies, they have to promote to internal energies. Then, $F[n]$ would harmonically unite these quantities in other manners or conditions.

Each electron individually possesses their own kinetic energy and independent from many-body effects. They have Coulomb repulsions from other electrons. Thus in auxiliary system, Hamiltonian $\hat{H}$ has to uphold Hartree energy, kinetic energy, and external potential terms. By deploying DFT, the expression is rewritten for ground-state energy as functional of density

$$E_{aux}[n] = T_s[n] + E_H[n] + \int d^3\vec{r} V_{ext}(\vec{r}) n(\vec{r}) \tag{3.4}$$

The first and the second term on the right-hand side of equation 3.4 can be calculated. The one-electron wave function ϕ_i of the auxiliary system can be derived as

$$T_s = -\frac{1}{2} \sum_{i=1}^{N} \langle \phi_i | \nabla^2 | \phi_i \rangle$$

$$E_H = \frac{1}{2} \int d^3\vec{r} d^3 r' \frac{n(\vec{r}) n'(\vec{r})}{|\vec{r} - \vec{r'}|} \tag{3.5}$$

$$n(\vec{r}) = \sum_{i=1}^{N} |\phi_i'|^2$$

The Kohn-Sham approach to DFT based on assumption, within auxiliary system, it is assorted to possess the similar ground-state density to original system. In order to prove condition, the auxiliary system should be changed into the manners that present many-body effects. It will also be available in the real physical system. The new term should be expressed and show the differentiation between the original systems and the auxiliary ones. The DFT formalism is

expressed as functional of density. To this additional term, Kohn and Sham have also given a name as the exchange-correlation functional $E_{XC}[n]$ which can express in terms of F as

$$F[n] = T_s[n] + E_H[n] + E_{ext}[n] \tag{3.6}$$

The advantage about this, $E_{xc}[n]$ is now an universal realistically approximated. Then, the total energy can be partitioned as follows,

$$E[n] = T_s[n] + E_H[n] + \int d^3\vec{r} V_{ext}(\vec{r})n(\vec{r}) + E_{XC}[n] \tag{3.7}$$

where T_s is kinetic energy of independent particles, E_H is self-interacting energy of electron density, and E_{XC} is exchange-correlation energy. The Kohn-Sham equations numerically derived, and the procedure in more details is demonstrated in Appendix D.

Because of the effects of the exchange-correlation, the potential possess the additional term as

$$h_{eff}|\phi_i\rangle = \left[-\frac{1}{2}\nabla^2 + v_H(\vec{r}) + v_{ext}(\vec{r}) + v_{XC}(\vec{r}) \right]|\phi_i\rangle = \epsilon_i|\phi_i\rangle \tag{3.8}$$

The solutions to the above equation are known as the Kohn-Sham orbitals ϕ_i for auxiliary system with correction approximation derived in exchange-correlation form. The essential element to all of these is clearly the E_{XC} term, and it unfortunately remains as approximation. The following Section §D.3 will cover this issue and outlines several approximations used within this work.

3.3   Exchange and Correlation Functionals

3.3.1   Local Density Approximation

The approximation is entitled by local density approximation (LDA), which is the simplest approximation to the exchange-correlation energy. It based on the assumption that exchange-correlation is not changed in homogeneous gas system, and only depends on the local value of ϵ_{XC}. This expressed as,

$$E_{XC}^{LDA} = \int d\vec{r} n(\vec{r}) \epsilon_{XC}^{LDA}(n(\vec{r})) \tag{3.9}$$

where ϵ_{XC}^{LDA} is exchange-correlation energy of homogeneous gas with density n.

The LDA approximation has worked impressively and is still used for many atomic systems. It also has less accuracy for the systems in which the electronic density varies rapidly, such as in molecules and at surfaces. However, it can be extended into the generalized gradient approximation (GGA) where the PW91 [156] and the simplified PBE [157] functionals are based on.

3.3.2 Generalized Gradient Approximations

The generalized gradient approximations (GGAs) have intimately proposed after the accomplishment of the LDA. Base on the assumption that dependence does not only on the local electron density but also its local gradient. The general form of GGA functionals are expressed as,

$$E_{XC}^{GGA} = \int d\vec{r} \epsilon_{XC}^{LDA} F(n, |\nabla n|, \dots) \tag{3.10}$$

where F is enhancement factor while various forms have been developed.

Normally, the GGA works very well for molecules, which has improved over several drawbacks of the LDA. In this thesis, the simplified PBE [157] is used for all self-consistent calculations. Additional discussion of GGA, referred to textbooks [9].

3.3.3 Hybrid Functionals

The decent developments have enabled the use of hybrid functionals. The basic idea is to incorporate amount of Hartree-Fock (HF) exchange with the exchange and correlation from LDA or GGA functional. These are several functionals, such as B3LYP [158, 159] where traditional functionals are mixed with a certain proportion of Hartree-Fock. Based on the arguments that exchange and correlation energy varies as a function of interelectronic coupling, Perdew, Ernzerhof, and Burke [157] introduced the form as

$$E_{XC} = E_{XC}^{GGA} + \frac{1}{4}(E_X^{HF} - E_{XC}^{GGA}) \tag{3.11}$$

They mixed 1/4 of Hartree-Fock exchange energy, and gave physical explanations.

3.4 All-Electron Core Treatment

The core treatment is the parameter that can be used to handle the electrons in the lowest atomic orbitals. For all-electron potential, these electrons will be treated in the same condition as in the case of valence electrons. As the elements get larger, the relativistic effects would considerably become more crucial matter for the core electrons treatment. For this core treatment method, all-electron potentials used in DMol^3 software package are proposed by Koelling *et al.* [160] and Douglas *et al.* [161]. Both core electrons and scalar relativistic effects are included in the calculations. This method may provide calculation with more accuracy, but it has also increased the computational cost.

3.5 Computational Strategy

This section presents a brief summary of hardware and software that entirely used for this computational research.

3.5.1   Hardware: High Performance Parallel Computing (HPC)

All calculations in this work were performed on high performance parallel computing (HPC) servers, Fujitsu CX250, at Japan Advanced Institute of Science and Technology (JAIST), Japan. The Fujitsu CX250 cluster is maintained by MPC Administrator Group, Research Center for Advanced Computing Infrastructure (RCACI).

The Fujitsu CX250 cluster provides 108 nodes (216CPU/2160core) + GPU node (8CPU/8GPU) with following specification:

Intra-node configuration (normal node)

- CPU: Intel Xeon E5-2680v2 2.80GHz (10Core) x2

- Memory: 64GB (4GB DDR3-1866 ECC x16)

Node memory bandwidth: 119GB/s

- In-node configuration (GPU node)

- CPU: Intel Xeon E5-2680v2 10Core x2,

- GPU: NVIDIA Tesla K40 x2

- Memory: 64GB

Network Infiniband 4xFDR (6.8GB/s)

3.5.2   Software: Materials Studio

All the DFT simulations were carried out throughout using DMol^3 package incorporated in Materials Studio platform by Dassault Systems Biovia K.K.

Chapter 4

Density Functional Theory of Transition Metal Phthalocyanine and Graphene

This chapter presents a density functional theory (DFT) for studying the molecular structure of transition metal phthalocyanines (TMPcs) on graphene for copper phthalocyanine (CuPc), nickel phthalocyanine (NiPc), cobalt phthalocyanine (CoPc), iron phthalocyanine (FePc), and manganese phthalocyanine (MnPc). Self-consistency simulations for molecular structures, bond lengths and angles, formations, stabilities, attraction sites, and binding energies of TMPc and graphene composite material are systematically discussed and carried out by employing the density functional theory (DFT) with including local density approximation (LDA), generalized gradient approximation (GGA), and a conventional hybrid, B3LYP, functionals. The bond lengths and bond angles acquired with different functionals utilized in this chapter are correlated to experimental data. Our results indicate that CoPc has the shortest interplane distances between TMPcs and a graphene layer. The attraction of CoPc on graphene is feasible; yielding a tunable composite electrode material that may lead the promising synthesis process due to their intrinsic electrical properties provided by CoPc/graphene.

4.1   Introduction

For the first decade of the 21st century, it has been remarkable with successful discovery of graphene [7, 20], a magnificent 2D material that has become the central attention of the worldwide scientific community in various aspects due to its superlative properties that are integrated into extensive applications and technologies [162]. For examples, the optical and conductive properties of graphene have been used for the solar cells [163, 164], light-emitting diodes (LEDs) [165, 166], and transparent electrodes [167]. The π-π interactions for these particular cases are a benefit between graphene and the organics systems [168–170].

TMPcs are macrocyclic complexes with the enlarged system of π density that which can adsorb on fullerenes or graphite system [45, 171–173] for the improvement of electrodes in which the TMPcs act as facilitator in the electrochemical processes of charge transfer. They are expected to be productive applications for detecting various organic molecules [45, 174–179]. In addition, TMPcs are also the well-known dyes that used in photovoltaic cells [180–184]. Furthermore, the composite materials of graphene with TMPcs have been used as complex central metal, i.e., cobalt [172], copper [185–188], nickel [189], zinc [190–192], and iron [193].
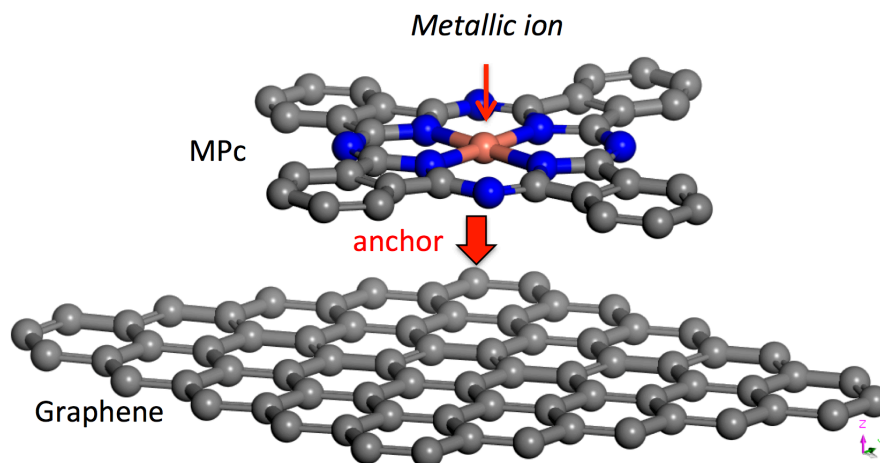
Figure 4.1: Model of metallic ion residing in the central cavity of phthalocyanine monomer, as an anchor, attracted on graphene sheet.

These composite materials have high potential in various applications such as electrochemical sensors [194], optoelectronics [185], photosynthesis, and transparent electrodes for solar energy conversion [190, 191].

In a previous work, the electronic structure of CuPc on graphene has been considered and investigated [186]. The computational study was performed entirely based on the density functional theory (DFT) method with LDA, GGA, and hybrid functionals to describe the geometry of the molecular structure in a favorable approach. The first principle calculations of their molecular geometries can deliver a well-founded basis for the interpreted calculations of experimental data and underline the physical systems. The relationship of calculated properties and their experimental phenomena will be explored. The computational results are useful for informatics materials to elucidate the formation of TMPc/graphene complex for both experimental conditions and industrialized synthesis.

In this work, different kinds of TMPc layers attracted on graphene sheet were selected as modeling systems for simulations. The central metallic ion dominating the physical and chemical characteristics of TMPc so the metallic ion will behave as 'anchor' for attracting to a specific site onto the graphene sheet, as mentioned in the subsection 2.2.2. The scheme is illustrated in Figure 4.1. Bond lengths and angles acquired from different functionals deployed in this dissertation are provided as electronic supplementary materials.

The present work aims to investigate the molecular structure, interlayered formation, stability, and binding energies of TMPc/graphene by using the Materials Studio software package. The details of these computational methods are provided in section 4.2. The qualitative differences between these functionals have been observed, and the pros and cons of utilizing these functionals are critically investigated to describe interfaces between TMPcs and graphene, summarized in the section 4.2.1 The effects of three different exchange and correlation functionals on the computational electronic structure of TMPcs and comparison of the computed results and the experimental data are systematically discussed in section 4.3.

4.2 Computational Method

In this research work, the reported DFT calculations were performed by utilizing the Materials Studio$^{®}$ v7.0.200 by Accelrys Software Inc. The method of choice of the exchange-correlation (XC) functionals were selected according to the considerable quality of the results because it would mainly depend on these selected approximation. The XC formalisms, spin treatment, and configurations are presented in the subsection 4.2.1, 4.2.3, and 4.2.2, respectively.

The core treatment with all-electron scheme within DMol^3 are used. Then, the double numerical (DN) basis set was also used, along with the 3.5-basis file for all the simulations. The convergence tolerance for the maximum force and maximum displacement for normal geometry optimization were set to 0.02 Ha $\mathring{A}^{-1}$ and 0.05 $\mathring{A}$, respectively.

The computational results in this dissertation expect the binding energies of TMPcs on a graphite surface, and the bond length and angle of each TMPc molecular structures. The constructed molecule of a TMPc/graphene surface would be the representative structure in the case of physical-layered contact, presented that the attracted site, as focusing on the central cavity of metal ion is within or approaching to the central carbon groups, the H-site as predicted similarly in the case of a metal atom on graphene sheet.

4.2.1 Exchange-Correlation

In this work, the prediction for evaluating the stability of these systems are strongly depended on the choice of exchange-correlation (XC) which are seriously concerned in general, therefore, the examination are using three different XCs. The functionals of LDA, GGA, and B3LYP were used to describe and predict the energies and formations of graphene and TMPcs interlayers, and also the individual geometries of graphene and TMPcs.

The reasons that the above three functionals are deployed for this study because for the case of LDA and GGA, they are chosen for their well-known credits with less resource consumption, and have been used in many series of electronic structure calculations for similar evaluation [195, 196]. The results obtained from LDA and GGA are contentedly for several organic molecules [197]. As references, they are included in this work to make contrast. If their results for this study turn out to achieve satisfied accuracy, then it would have saved large amount of computational cost and time, which are quite important factors for material informatics or automated materials searching.

On the other hand, B3LYP, hybrid functional is an improvement of LDA and GGA. While LDA and GGA yield their total energies from just the electronic density, B3LYP has corrected that and improved its approximation to the XC energy term of the total energy over system of electrons. B3LYP may have the benefits of more accuracy in calculating the actual total energy because it has also included a nearly exact expression for the exchange components. So B3LYP is often the selected method for calculating standard chemical models for many applications [198]. In this study, the predictions by B3LYP would be most reliable for examining the evaluated interlayers among the three selected functionals within this work for the stacking layers. Even though the computed results are more accurate with B3LYP, but that would come
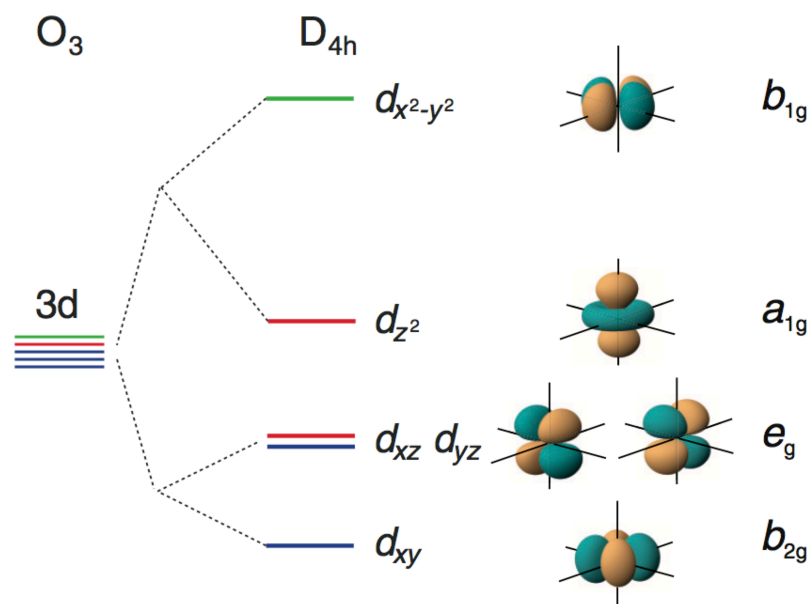
Figure 4.2: The sketch of the energy splitting of the $3d$ metal orbital configuration embedded in D_{4h} symmetry. Brown and green indicate the different phases of wavefunction, re-printed from [3].

with the expensive price of computational cost and time.

In a symposium paper containing an overview by Baker *et al.* [199] stated that B3LYP marginally consumes computational cost more than standard DFTs. Later, Lynch *et al.* also reported their investigation for test cases and compared the cost and accuracy of various computational methods. They found that B3LYP yielded remarkably accuracy for geometries and energies [200], but have to tradeoff with performance-to-cost ratio.

Note that for extent within this study on the stacking, the van der Waals interactions were neglected, but it should be included into account for better evaluations of the systems in the future work. The additional information about vdW-DF method is included in the section D.3.4 of Appendix D.

4.2.2 Spin Configuration

The TMPc molecules are evaluated under D_{4h} symmetry, where their d-orbitals can be classified as the square-planar ligand-field. So, the ground state electronic configurations of isolated TMPc molecules are investigated under the D_{4h} symmetry. With these 5 metal d-orbitals are reduced symmetry and transformed to the degenerated $3d$ orbitals as a_{1g} (d_{z^2}), b_{1g} ($d_{x^2-y^2}$), and b_{2g} (d_{xy}) in singlet states, and e_g (d_{zx}, d_{yz}) in doublet state, as shown in Figure 4.2. The electron filling scheme for each selected TMPc with total spin are displayed in Figure 4.3. The each different metal supplies the electrons filled these states. The information of d-electron ground states for the α and β phases of TMPcs from the experiment and calculations are shown in
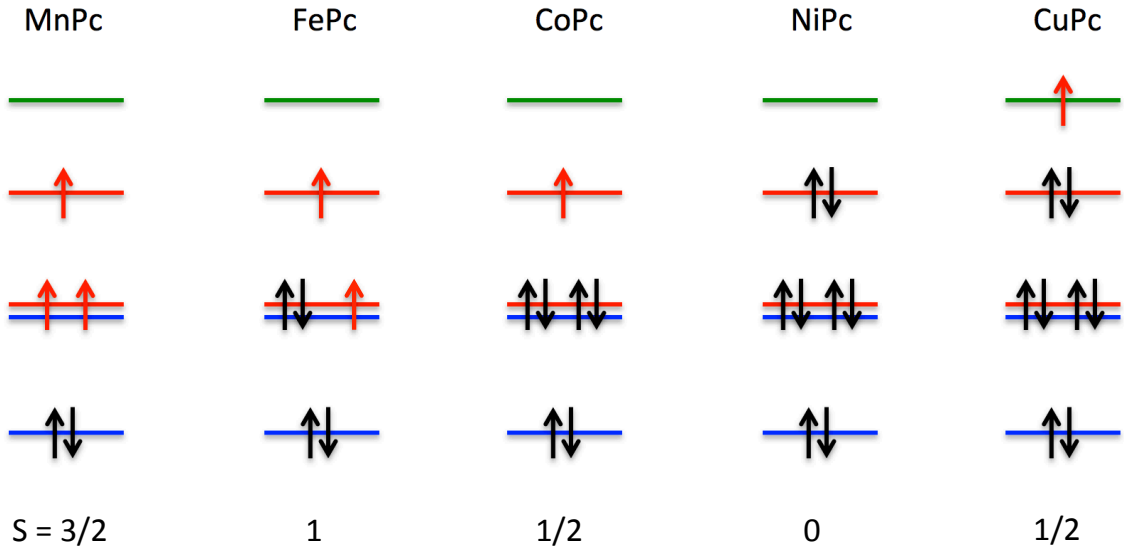
Figure 4.3: Schematic of paired and unpaired electrons of MnPc, FePc, CoPc, NiPc, and CuPc. Black indicates paired electrons, and red indicates the unpaired ones. The total spin due to unpaired electrons are at the bottom.

Table 4.1: Ground state orbital occupancy and total spin of TMPc molecules determined from series of experiments.

TMPcs	Ground State Occupancy	Total Spin	Refs.
α-MnPc		3/2	[201]
β-MnPc	$(b_{2g})^2(e_g)^2(a_{1g})^1$	3/2	[201, 202]
α-FePc	$(b_{2g})^2(e_g)^3(a_{1g})^1$	1	[203]
β-FePc	$(b_{2g})^2(e_g)^3(a_{1g})^1$	1	[204]
β-FePc	$(a_{1g})^2(e_g)^3(b_{2g})^1$	1	[205]
α-CoPc	$(e_g)^{3.8}(b_{2g})^2(a_{1g})^{1.2}$	1/2	[206]
β-CoPc	$(b_{2g})^2(e_g)^4(a_{1g})^1$	1/2	[207]
β-NiPc	$(b_{2g})^2(e_g)^4(a_{1g})^2$	0	[208]
α-CuPc		1/2	[201]
β-CuPc	$(b_{2g})^2(e_g)^4(a_{1g})^2(b_{1g})^1$	1/2	[201]

Table 4.2: Ground state orbital occupancy and total spin of TMPc molecules obtained from a series of computational methods. ^{i} refers to isolated molecule.

TMPcs	Ground State Occupancy	Ground State	Total Spin	Method	Refs.
MnPc^i		^4E_g	3/2	GGA	[209]
β-MnPc	$(b_{2g})^1(e_g)^3(a_{1g})^1$	^4E_g	3/2	*ab initio*	[52]
β-FePc		$^3B_{2g}/^3A_g$	1	PBE, B3LYP	[196]
β-FePc	$(b_{2g})^2(a_{1u})^2(a_{1g})^2(1e_g)^2$	$^3A_{2g}$	1	LDA	[210]
β-FePc	$(b_{2g})^2(a_{1u})^2(a_{1g})^2(1e_g)^2$	$^2A_{1g}$	1	*ab initio*	[52]
CoPc^i		$^2A_{1g}$	1/2	GGA	[209]
β-CoPc	$(b_{2g})^2(e_g)^4(a_{1g})^1$	$^2A_{1g}$	1/2	*ab initio*	[52]
β-CoPc	$(a_{1g})^2(a_{1u})^2(1e_g)^3$	^1E_g	1/2	LDA	[210]
β-NiPc		$^1A_{1g}$	0	LDA	[210]
β-CuPc		$^2B_{1g}$	1/2	LDA	[210]

Table 4.1 and 4.2, respectively.

1. **Manganese Phthalocyanine**

   The ground state configuration of MnPc molecule was investigated under D_{4h} symmetry reported from the experimental technique (see Table 4.1) and the theoretical calculation (see Table 4.2). The five electrons are accommodated in $3d$-shells from Mn. For α phase, it was confirmed by Heutz *et al.* with the simulation of the Brillouin function for a spin, S = 3/2 [201].

2. **Iron Phthalocyanine**

   The orbital configuration of Fe from experimental data is E_{gA} $(b_{2g})^2(e_g)^3(a_{1g})^1$, see Table 4.1. The $(e_g)^3$ orbital doublet is triply occupied with a full and a half filled orbital as depicted in Figure 4.3, where S = 1.

3. **Cobalt Phthalocyanine**

   Both α and β phases of CoPc are paramagnetic were determined using electron spin resonance (ESR). The neighboring N atoms that are adjacent to the central Co position have impacted on the quadrupole splitting, and it is greater in β phase [211]. Co presents planar anisotropy, and Co atom surrounded in the Pc monomer evidenced by magnetic susceptibility with S = 1/2.

4. **Nickel Phthalocyanine**

   For β phase of NiPc, its spin is S = 0 for both obtained from experiment and calculation, refered to Table 4.1 and 4.2.

5. **Copper Phthalocyanine**

   For α phase, it was confirmed by Heutz *et al.* with the simulation of the Brillouin function for a spin, S = 1/2 [201]. The β phase of CuPc is paramagnetic, and with the usage of the nuclear magnetic resonance (NMR) proton spectroscopy [212], it was determined that its spin is S = 1/2.
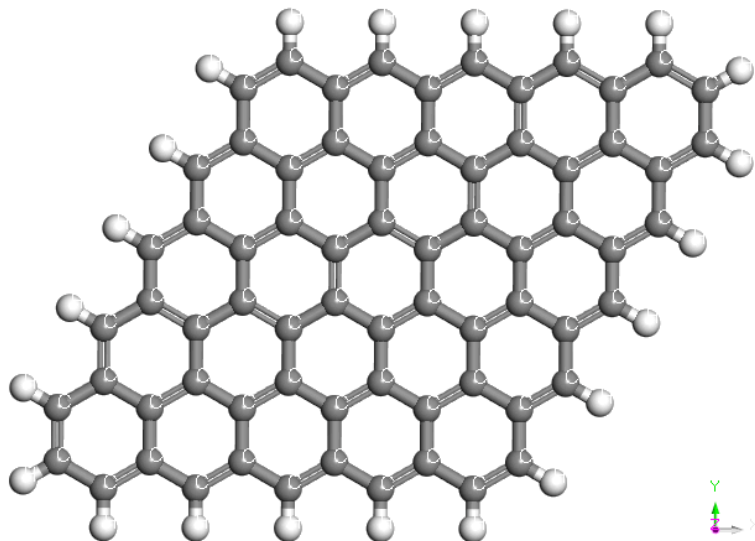
Figure 4.4: Schematic view of the pristine graphene (25 benzene rings), with the terminal hydrogen atoms at the edge.

4.2.3 Spin Treatment

The treatments of spin polarization in many calculations have been different. Most calculations have utilized the spin-unrestricted configuration; however, other cases may have taken the spin-restricted approach. In the case of CuPc, Cu atom is not generally participated with magnetic properties because only single occupied $4s$ orbital of a Cu atom significantly direct this to spin splitting [45]. Consequently, CuPc has to be treated in the case of the spin-unrestricted condition. Therefore, spin unrestricted calculations were carried out throughout the entire investigation, and the geometries were optimized independently for each structure: graphene, CuPc, and graphene/CuPc, where pristine graphene with 25 benzene rings, with the terminal hydrogen atoms at the edges, was used, as shown in Figure 4.4.

As the molecular size getting larger, complexity of the molecules are demanded to reach the convergence; therefore, an optimization procedure has to be carried out. In order to acquire the equilibrium geometry for this complex, first, the isolated graphene model needs to be optimized; then, applying this obtained geometry as a starting point to proceed, the monomer of CuPc has been supplied originally in the middle structure of graphene sheet models, and afterward this whole structure has again been re-optimized. Then, the adsorption of CuPc on the graphene layer is performed, for optimizing the entire system. Afterward, geometry optimization, vibrational frequency calculations have been performed to assure that the optimized systems corresponds to minimum energetic structures.

4.3 Results and Discussion

After geometry optimized with the same computational setup, the molecular structure of TMPc monomer is obtained as depicted schematically in Figure 2.11. The monomer of TMPc consists of a central cavity ion, which in case metal atoms of Mn, Fe, Co, Ni, and Cu. They are bridged
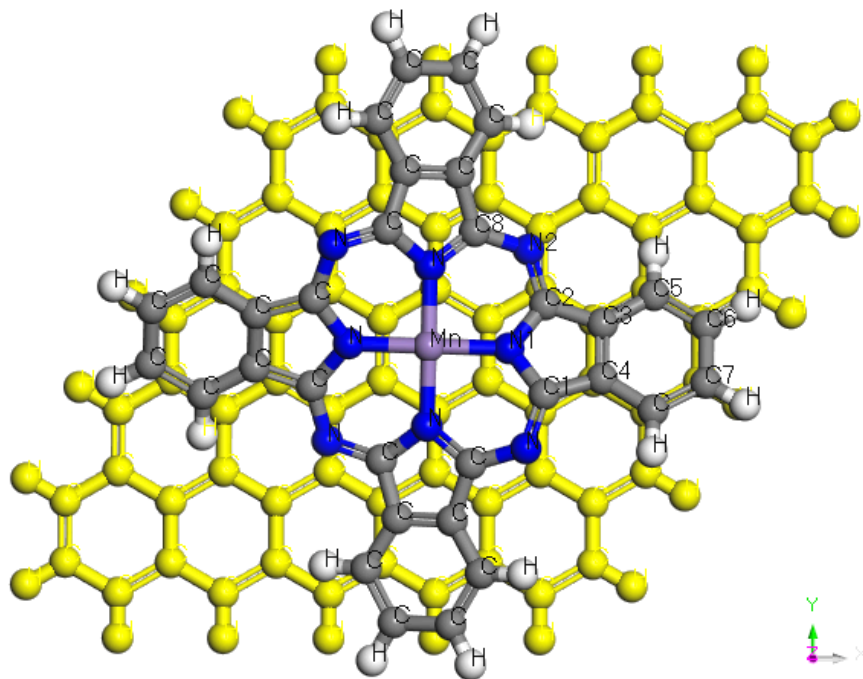
Figure 4.5: The top-view structure of the TMPc molecule overlayer graphene sheet. The central metal atom is located in the middle of benzene ring, where the highlighted molecule in yellow represents the graphene layer. From the observation, the central ion of Mn and Cu atom deviate a little off the center of benzene ring.

with other four N atoms surrounded by four pyrrole groups that each individually attached to other 4 benzenes as mentioned in subsection §2.3.1. The following subsections are individually provided the computational results of MnPc, FePc, CoPc, NiPc, and CuPc, accordingly.

By analyzing if these metal phthalocyanines can adsorb onto graphene plane. This aims to investigate the structure of these molecular complexes from the related parameterized geometries. Then, the optimization of molecular structures will be revised. According to the energetic point of view, the adsorption between these interlayers would direct to the stability of these complexes needed to be considered. For the obtained structural stabilities, it is remarkable to gain knowledge whether the structural interaction between monolayer of graphene and attracted layer of each TMPc.

4.3.1 Manganese Phthalocyanine on Graphene

The molecular structure of manganese phthalocyanine (MnPc) is similar to other metal-substituted Pcs that have planar molecules as D_{4h} symmetry. The numbering atoms are shown in Figure 2.11, where the central metal atom is manganese (Mn) atom, which is in a +2 oxidizing state. The Mn center has a formal $3d^5$ electronic configuration. Monomer structure of MnPc is depicted in Figure 2.11 where exhibits the arrangement of discrete, planar MnPc molecule like other selected TMPcs. For the rigidity of MnPc molecule, a geometrical optimization are computationally performed to examine the all possible positions of these atoms, resulting in
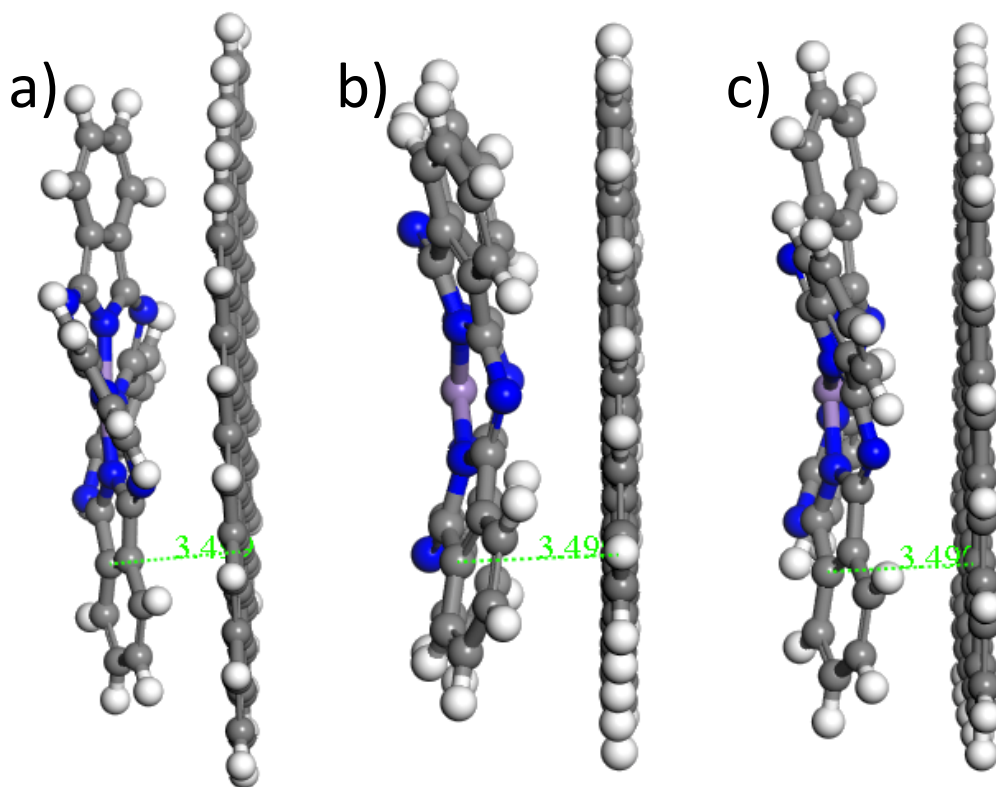
Figure 4.6: The interplane distance between graphene and MnPc calculated by (a) LDA, (b) PBE, and (c) B3LYP. The graphene plane is on the right, and MnPc is one the left of each figure.

Table 4.3.

Table 4.3: Selected bond length in Å and bond angle in degree (°) of MnPc calculated with different exchange-correlation functionals; Atom labeled in Figure 2.11, and experimental data from Reference [10]. Parenthesis indicates deviation from the experiment.

Properties	Experiment [10]	Computational Results		
		LDA	PBE	B3LYP
Mn-N1	1.937	1.874[3.25]	1.916[1.08]	1.905[1.65]
N1-C2	1.388	1.438[3.60]	1.438[2.88]	1.421[2.38]
C2-N2	1.323	1.339[1.21]	1.345[1.66]	1.378[4.16]
C2-C3	1.450	1.458[0.55]	1.463[0.90]	1.421[2.00]
C3-C4	1.392	1.431[2.80]	1.435[3.09]	1.433[2.95]
C3-C5	1.396	1.398[0.14]	1.393[0.21]	1.423[1.93]
C5-C6	1.380	1.402[1.59]	1.402[1.59]	1.371[0.65]
C6-C7	1.391	1.409[1.29]	1.403[0.86]	1.437[3.31]
C2-N1-C1	107.6	104.71[2.69]	105.87[1.61]	104.23[3.13]
N1-C2-N2	127.7	126.45[0.98]	126.26[1.13]	125.62[1.63]
N1-C2-C3	109.6	110.54[0.86]	109.98[0.35]	111.31[1.56]
C2-N2-C8	N/A	119.81[-]	119.31[-]	120.16[-]
C2-C3-C4	N/A	106.90[-]	106.88[-]	106.55[-]
C4-C3-C5	N/A	120.89[-]	120.85[-]	120.32[-]
C3-C5-C6	N/A	117.80[-]	117.84[-]	118.19[-]
C5-C6-C7	N/A	121.31[-]	121.31[-]	121.49[-]

Table 4.4: Binding (E_{Bind}) energies and the distance between layers of graphene, MnPc, bilayer graphene, and MnPc-graphene.

System	E_{Bind} (eV)			Distance (Å)		
	LDA	PBE	B3LYP	LDA	PBE	B3LYP
G	-684.02	-587.07	-559.84	-	-	-
MnPc	-566.19	-535.50	-536.02	-	-	-
G-G	-1339.56	-1199.53	-1077.19	3.35	3.47	3.16
MnPc-G	-909.81	-906.78	-911.27	3.42	3.34	3.49

4.3.2 Iron Phthalocyanine on Graphene

The crystallite data of FePc [11] has systematically been deployed to construct a single layer of thin film on behalf of FePc planar model, as depicted in Figure 2.11. Similarly to NiPc molecular model [72]. The molecular geometry of the FePc monomer as D_{4h} symmetry. The selected 3d lattice is the P4/mmm symmetry, where the numbering atoms as shown in Figure 2.11. For
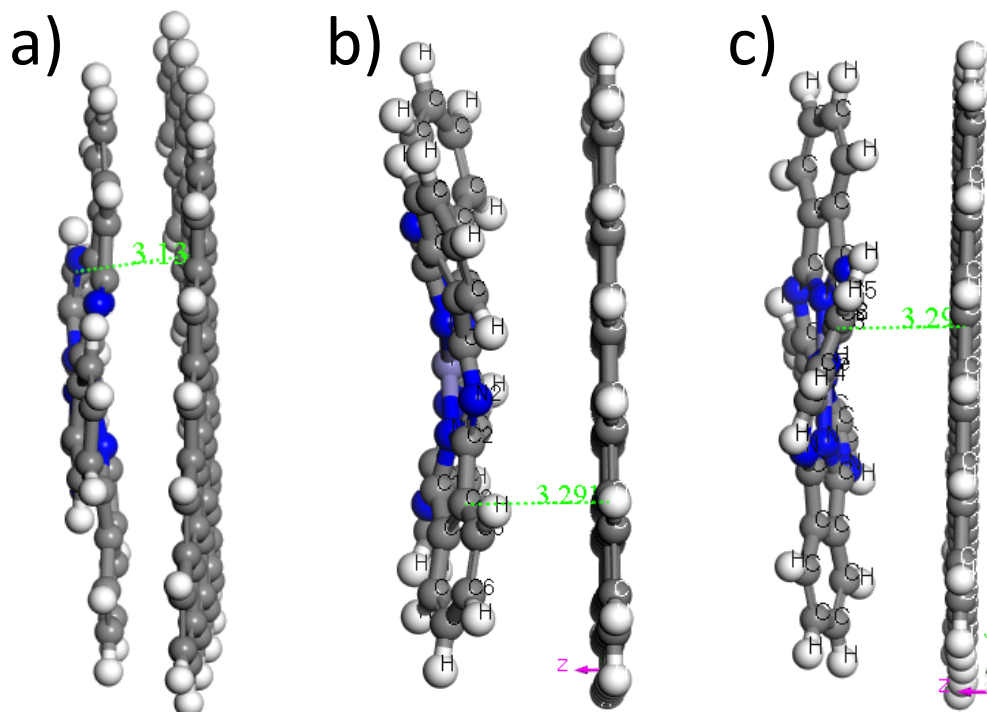
Figure 4.7: The interplane distance between graphene and FePc, where graphene plane is on the left of each figure, and FePc is one the right, calculated by (a) LDA, (b) PBE, and (c) B3LYP.

the rigidity of FePc molecules, a geometrical optimization are also computationally performed for internally examining the all possible positions of these atoms, resulting in Table 4.5.

4.3.3 Cobalt Phthalocyanine on Graphene

The computational setup for CoPc geometry optimization is as the same as procedure of MnPc and FePc, repeatedly. Its final molecular structure is illustrated in Figure 4.5.

4.3.4 Nickel Phthalocyanine on Graphene

The computational setup for NiPc geometry optimization is as the same as procedure of those TMPc, repeatedly. Its final molecular structure is illustrated in Figure 4.5.

4.3.5 Copper Phthalocyanine on Graphene

The detailed experimental structure of each TMPc in the crystalline states are demonstrated and is consistent with the calculations. The optimized bond lengths and bond angles, calculated with three different functionals deployed in this dissertation, are presented in the Table 4.3, 4.5, 4.7, 4.10, and 4.13 along with their experimental correlations. The results indicate that the type of functionals has significantly no remarkable effects upon the calculations of geometry, and the computational outcomes are in good agreement with former experimental measurements.

Table 4.5: Selected bond lengths in Å and bond angles in degree (°) of FePc calculated with different exchange-correlation functionals. Atoms labeled in Figure 2.11, and experimental data [11]. Parenthesis indicates deviation from the experiment.

Properties	Experiment [11]	Computational Results		
		LDA	PBE	B3LYP
Fe-N1	1.927	1.849[4.05]	1.851[3.94]	1.911[0.83]
N1-C2	1.378	1.425[3.41]	1.413[2.54]	1.430[3.77]
C2-N2	1.322	1.330[0.61]	1.352[2.27]	1.323[0.08]
C2-C3	1.450	1.479[2.00]	1.466[1.10]	1.487[2.55]
C3-C4	1.392	1.422[2.16]	1.426[2.44]	1.426[2.44]
C3-C5	1.395	1.385[0.72]	1.395[0.00]	1.380[1.08]
C5-C6	1.390	1.401[0.79]	1.396[0.43]	1.414[1.73]
C6-C7	1.394	1.396[0.14]	1.407[0.93]	1.391[0.22]
C2-N1-C1	107.3	106.70[0.56]	106.40[0.84]	105.84[1.36]
N1-C2-N2	127.8	127.33[0.37]	125.72[1.63]	127.74[0.05]
N1-C2-C3	109.7	109.63[0.06]	110.20[0.27]	110.40[0.64]
C2-N2-C8	N/A	119.44[-]	121.53[-]	121.02[-]
C2-C3-C4	N/A	106.93[-]	106.57[-]	106.68[-]
C4-C3-C5	N/A	121.07[-]	120.89[-]	121.21[-]
C3-C5-C6	N/A	117.65[-]	117.80[-]	117.58[-]
C5-C6-C7	N/A	121.29[-]	121.31[-]	121.21[-]

Table 4.6: Binding (E_{Bind}) energies and the distance between layers of graphene, FePc, bilayer graphene, and FePc-graphene.

System	E_{Bind} (eV)			Distance (Å)		
	LDA	PBE	B3LYP	LDA	PBE	B3LYP
G	-684.02	-587.07	-559.84	-	-	-
FePc	-347.44	-345.05	-375.79	-	-	-
G-G	-1339.56	-1199.53	-1077.19	3.35	3.47	3.16
FePc-G	-912.25	-912.22	-909.77	3.13	3.26	3.29
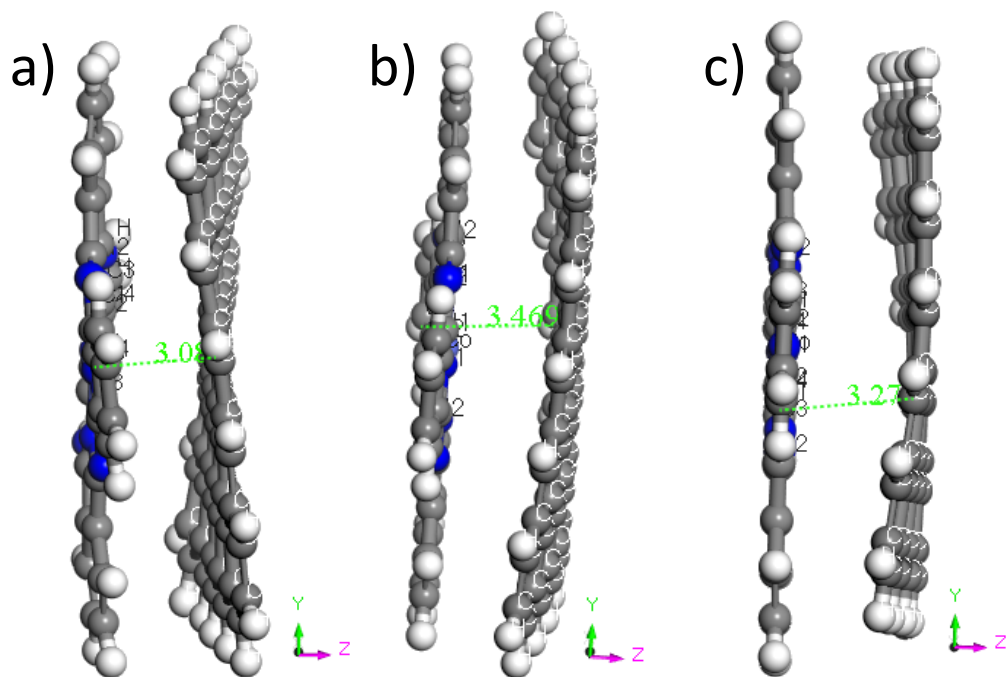
Figure 4.8: The interplane distance between graphene and CoPc, where CoPc is on the left of each figure, and graphene plane is one the right, calculated by (a) LDA, (b) PBE, and (c) B3LYP.
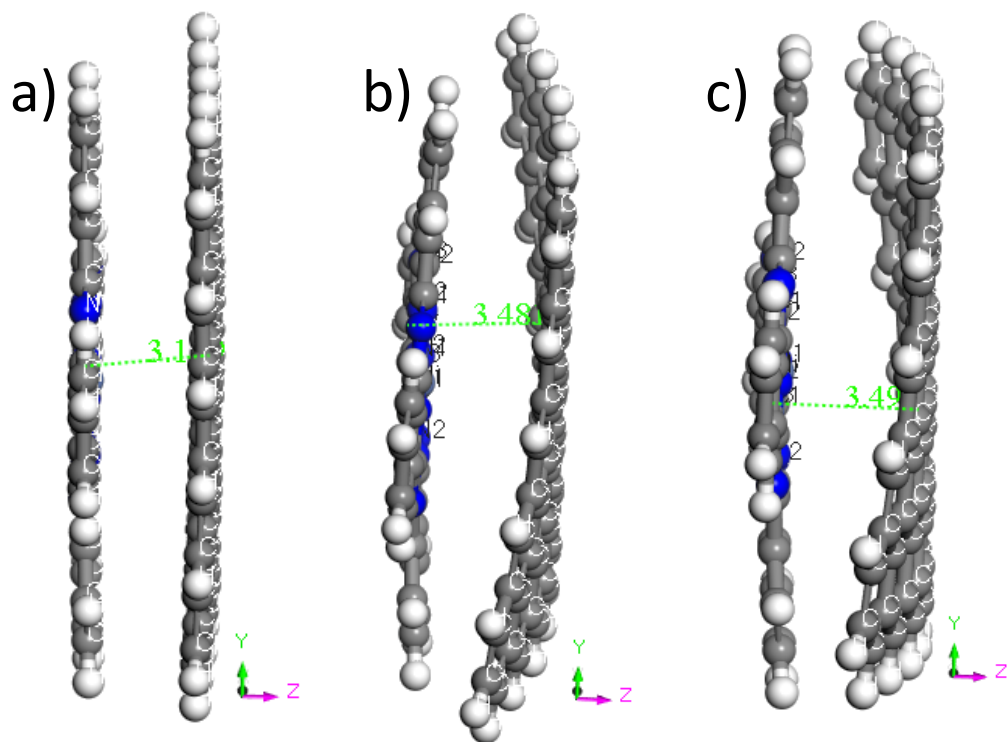
Figure 4.9: The interplane distance between graphene and NiPc, where NiPc is on the left of each figure, and graphene plane is one the right, calculated by (a) LDA, (b) PBE, and (c) B3LYP.

Table 4.7: Parameters of CoPc structure calculated with different exchange-correlation functionals, where the bond length in Å and bond angle in degree (°). Their atoms labeled from Figure 2.11, and experimental data [12] presented for comparison. Parenthesis indicates deviation from the experiment.

Properties	Experiment [12]	Computational Results		
		LDA	PBE	B3LYP
Co-N1	1.912	1.97[2.77]	2.00[4.34]	1.98[3.30]
N1-C2	1.381	1.41[2.32]	1.40[1.45]	1.40[1.59]
C2-N2	1.317	1.33[1.14]	1.34[1.75]	1.34[1.52]
C2-C3	1.459	1.43[1.85]	1.44[1.10]	1.44[1.23]
C3-C4	1.400	1.43[2.00]	1.44[2.57]	1.43[2.07]
C3-C5	1.394	1.41[0.86]	1.42[1.51]	1.41[1.00]
C5-C6	1.401	1.41[-]	1.42[-]	1.41[-]
C6-C7	1.405	1.42[-]	1.42[-]	1.42[-]
C2-N1-C1	107.1	106.47[0.59]	107.31[0.77]	106.89[0.10]
N1-C2-N2	127.9	125.13[2.21]	125.32[1.49]	125.45[1.59]
N1-C2-C3	109.7	109.60[0.11]	109.28[0.30]	109.57[0.03]
C2-N2-C8	N/A	126.19[-]	126.43[-]	125.49[-]
C2-C3-C4	N/A	106.94[-]	107.08[-]	106.96[-]
C4-C3-C5	N/A	120.95[-]	120.86[-]	120.86[-]
C3-C5-C6	N/A	117.88[-]	117.87[-]	117.66[-]
C5-C6-C7	N/A	121.15[-]	121.27[-]	121.51[-]

Table 4.8: HOMO, LUMO, (ΔHL) energies of graphene, CoPc, bilayer graphene, and CoPc-graphene.

System	E_{HOMO} (eV)			E_{LUMO} (eV)			ΔHL (eV)		
	LDA	PBE	B3LYP	LDA	PBE	B3LYP	LDA	PBE	B3LYP
G	-3.80	-3.63	-3.82	-3.52	-3.36	-3.54	0.28	0.27	0.28
CoPc	-5.25	-5.20	-5.03	-3.79	-3.81	-3.37	1.46	1.39	1.66
G-G	-3.74	-3.56	-3.76	-3.51	-3.35	-3.45	0.23	0.21	0.31
CoPc-G	-4.01	-3.92	-4.00	-3.93	-3.76	-3.90	0.08	0.16	0.10

Table 4.9: Binding (E_{Bind}) energies and the distance between layers of graphene, CoPc, bilayer graphene, and CoPc-graphene.

System	E_{Bind} (meV)			Distance (Å)		
	LDA	PBE	B3LYP	LDA	PBE	B3LYP
G	-684.02	-587.07	-559.84	-	-	-
CoPc	-359.14	-332.14	-404.98	-	-	-
G-G	-1339.56	-1199.53	-1077.19	3.35	3.47	3.16
CoPc-G	-1019.96	-932.38	-1000.19	3.09	3.28	3.47

Table 4.10: Parameters of NiPc structure calculated with different exchange-correlation functionals, where bond length in Å and bond angle in degree (°). Atom labeled from Figure 2.11, and experimental data [13] reported for comparison. Parenthesis indicates deviation from the experiment.

Properties	Experiment [13]	Computational Results		
		LDA	PBE	B3LYP
Ni-N1	1.83	1.97[7.87]	2.01[9.73]	1.97[7.60]
N1-C2	1.38	1.41[2.32]	1.42[3.19]	1.41[2.17]
C2-N2	1.38	1.33[3.41]	1.35[2.10]	1.33[3.41]
C2-C3	1.46	1.43[1.85]	1.45[0.89]	1.44[1.64]
C3-C4	1.38	1.43[3.55]	1.44[4.57]	1.43[3.48]
C3-C5	1.39	1.41[1.15]	1.42[2.23]	1.41[1.08]
C5-C6	N/A	1.41[-]	1.42[-]	1.41[-]
C6-C7	N/A	1.42[-]	1.43[-]	1.41[-]
C2-N1-C1	99.0	106.83[7.91]	107.31[8.39]	106.89[7.97]
N1-C2-N2	126.0	125.13[0.69]	125.32[0.54]	125.45[0.44]
N1-C2-C3	115.0	109.60[4.70]	109.28[4.97]	109.57[4.72]
C2-N2-C8	N/A	126.19[-]	126.43[-]	125.49[-]
C2-C3-C4	N/A	106.94[-]	107.08[-]	106.96[-]
C4-C3-C5	N/A	120.95[-]	120.86[-]	120.86[-]
C3-C5-C6	N/A	117.88[-]	117.87[-]	117.66[-]
C5-C6-C7	N/A	121.15[-]	121.27[-]	121.51[-]

Table 4.11: HOMO, LUMO, HOMO-LUMO gap (*Δ*HL) energies of graphene, NiPc, bilayer graphene, and NiPc-graphene.

System	E_{HOMO} (eV)			E_{LUMO} (eV)			*Δ*HL (eV)		
	LDA	PBE	B3LYP	LDA	PBE	B3LYP	LDA	PBE	B3LYP
G	-3.80	-3.63	-3.82	-3.52	-3.36	-3.54	0.28	0.27	0.28
NiPc	-5.26	-5.06	-5.21	-3.84	-3.71	-3.40	1.42	1.35	1.81
G-G	-3.74	-3.56	-3.76	-3.51	-3.35	-3.45	0.23	0.21	0.31
NiPc-G	-4.03	-3.80	-3.99	-3.91	-3.62	-3.75	0.13	0.18	0.24

Table 4.12: Binding (E_{Bind}) energies and the distance between layers of graphene, NiPc, bi-layer graphene, and NiPc-graphene.

| System	E_{Bind} (meV)			Distance (Å)		
	LDA	PBE	B3LYP	LDA	PBE	B3LYP
G	-684.02	-587.07	-559.84	-	-	-
NiPc	-380.96	-318.60	-412.48	-	-	-
G-G	-1339.56	-1199.53	-1077.19	3.35	3.47	3.16
NiPc-G	-1007.57	-898.13	-963.46	3.14	3.48	3.50
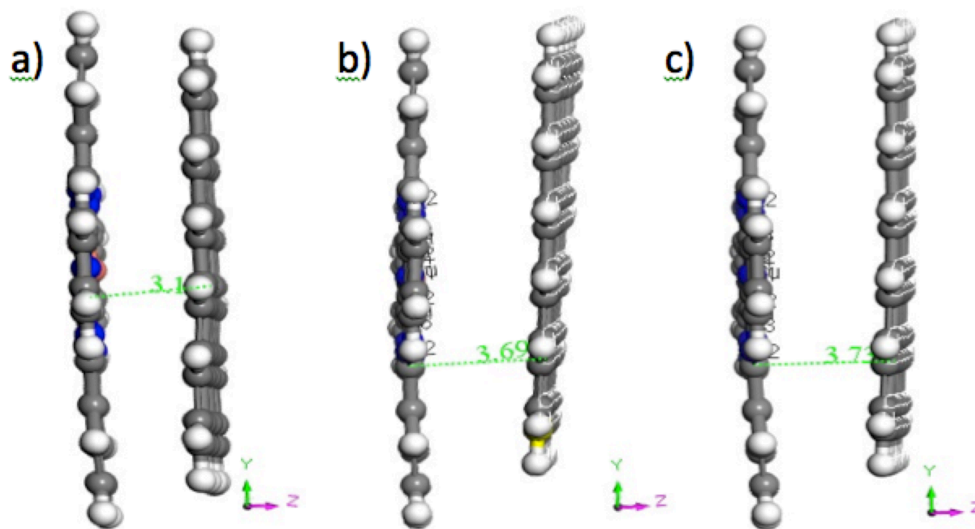
Figure 4.10: The interplane distance between graphene and CuPc, where CuPc is on the left of each figure, and graphene plane is one the right, calculated by (a) LDA, (b) PBE, and (c) B3LYP.

Table 4.13: Parameters of CuPc molecular structure calculated with indicated different exchange and correlation functionals, referring to atom labeled from Figure 2.11, where bond length measured in Å and bond angle in degree (°). Experimental data reported for comparison [14]. Parenthesis indicates deviation from the experiment.

Properties	Experiment [14]	Computational Results		
		LDA	PBE	B3LYP
Cu-N1	1.935	1.99[2.84]	2.02[4.60]	2.01[3.67]
N1-C2	1.366	1.41[3.15]	1.42[4.03]	1.41[3.29]
C2-N2	1.328	1.34[0.53]	1.35[1.88]	1.35[1.28]
C2-C3	1.453	1.44[1.24]	1.45[0.21]	1.44[0.69]
C3-C4	1.400	1.43[2.21]	1.45[3.29]	1.44[2.57]
C3-C5	1.388	1.41[1.30]	1.42[2.38]	1.41[1.66]
C5-C6	1.377	1.41[2.61]	1.42[3.34]	1.41[2.61]
C6-C7	1.400	1.42[1.14]	1.43[2.00]	1.42[1.29]
C2-N1-C1	107.3	107.48[0.17]	107.85[0.52]	107.89[0.55]
N1-C2-N2	127.6	125.18[1.90]	125.41[1.71]	125.80[1.41]
N1-C2-C3	110.4	109.21[1.07]	108.94[1.32]	108.96[1.30]
C2-N2-C8	N/A	126.71	126.83	126.90
C2-C3-C4	N/A	107.01	107.05	107.09
C4-C3-C5	N/A	120.94	120.77	120.86
C3-C5-C6	N/A	117.91	117.92	117.68
C5-C6-C7	N/A	121.14	121.31	121.49

Table 4.14: HOMO, LUMO, HOMO-LUMO gap (ΔHL) energies of graphene, CuPc, bilayer graphene, and CuPc-graphene.

System	E_{HOMO} (eV)			E_{LUMO} (eV)			ΔHL (eV)		
	LDA	PBE	B3LYP	LDA	PBE	B3LYP	LDA	PBE	B3LYP
G	-3.80	-3.63	-3.82	-3.52	-3.36	-3.54	0.28	0.27	0.28
CuPc	-4.88	-4.88	-4.83	-3.87	-3.71	-3.47	1.01	1.18	1.36
G-G	-3.74	-3.56	-3.76	-3.51	-3.35	-3.45	0.23	0.21	0.31
CuPc-G	-4.04	-3.81	-4.01	-3.93	-3.59	-3.73	0.11	0.22	0.28

Table 4.15: Binding (E_{Bind}) energies and the distance between layers of graphene, CuPc, bilayer graphene, and CuPc-graphene.

System	E_{Bind} (meV)			Distance (Å)		
	LDA	PBE	B3LYP	LDA	PBE	B3LYP
G	-684.02	-587.07	-559.84	-	-	-
CuPc	-375.79	-336.44	-421.83	-	-	-
G-G	-1339.56	-1199.53	-1077.19	3.35	3.47	3.16
CuPc-G	-1003.16	-894.26	-959.31	3.16	3.69	3.73

Table 4.16: Binding (E_{Bind}) energies and the distance between layers of bilayer graphene, and TMPc/graphene from calculation results.

System	E_{Bind} (eV)			Distance (Å)		
	LDA	PBE	B3LYP	LDA	PBE	B3LYP
G-G	-1339.56	-1199.53	-1077.19	3.35	3.47	3.16
CuPc-G	-1003.16	-894.26	-959.31	3.16	3.69	3.73
NiPc-G	-1007.57	-898.13	-963.46	3.14	3.48	3.50
CoPc-G	-1019.96	-932.38	-1000.19	3.09	3.28	3.47
FePc-G	-912.25	-912.22	-909.77	3.13	3.26	3.29
MnPc-G	-909.81	-906.78	-911.27	3.42	3.34	3.49

In the first row, the metal-nitrogen (M-N1) distance from experiment is notably shorter than from LDA, PBE, and B3LYP calculations. Considering the bond of N1-C2 with its length inside the Pc molecule, it shows the same tendency. These are the practical behaviors of these functionals for such organic compounds [109]. The LDA functional results in slightly closer bond lengths, the PBE functional provides with slightly extended bond lengths, and the conventional hybrid functional is between those two. The C2-N2 bond length is more distant from the central metal atom. On the other hand, the bond distances and bond angles from experiment are slightly different than from the calculations.

Full-optimized geometry of TMPcs under D_{2h} symmetry restrictions directs to molecular structures that are approached to the prospective D_{4h} symmetry. Geometry optimization leads to planar structures that have relatively not been affected in which indicate that the geometry of CuPc (see Figure 4.10), and slightly twisted or bent graphene in CoPc and NiPc (see Figure 4.8 and 4.9, respectively). On the other hands, there are distorted in molecular structures of MnPc and FePc (see Figure 4.6 and 4.7, respectively)., while graphene sheet is clearly kept lying flat.

The summarized results for calculated E_{bind} are presented in Table 4.16. From the relative binding plots depicted in Figure 5.1, it indicate that CoPc layer attracted on basal graphene sheet is the most stable structure because its binding energy has the lowest one among the other selected TMPcs. CoPc layer behaves as a guest molecule with π-domain, strongly physical contact to the π-π stacking onto graphene sheet that also behaves as a host electrode. The further discussion will be carried on in the next chapter.

Chapter 5

Summary and Further Discussion

5.1 Limitation of Spin-Restricted Conditions

The treatments of spin polarization in most calculations have been different. where many calculations have used an spin-unrestricted configuration, but some have taken a spin-restricted approach. In the case of the TMPcs in this initial work, it was first started with the computational study of CuPc, where copper atom resided in the central cavity of Pc, and Cu atom is not generally associated with magnetic properties because the single occupied $4s$ orbital of the Cu atom significantly leads to spin splitting [45]. Consequently, the monomer of CuPc has been treated in a spin-unrestricted manner in the previous study [186]. Therefore, spin-unrestricted calculations should be employed throughout on the other calculations of TMPcs as well, in order to keep consistency and fair evaluations in comparison.

5.2 Limitation of Exchange and Correlation

In this current study, the functionals of LDA, GGA, and hybrid were used to describe and predict the energies and formations of graphene and TMPcs interlayers, and also the individual geometries of graphene and TMPcs. The computational results in this dissertation expect the binding energies of TMPcs on a graphite surface, and the bond length and angle of each TMPc molecular structures whereas experiment and calculation results are in good agreement. The constructed molecule of the TMPc/graphene interlayer would be the representative structure in the case of physical-layered contact, presented that the attracted site, as focusing on the central cavity of metal ion is within or approaching to the central carbon groups, the H-site as predicted similarly in the case of a metal atom on graphene sheet from Section §2.2.2.

The three functionals are deployed for this work because LDA and GGA have gained credits with less consumption of computing resources. The results obtained from LDA and GGA are contentedly for several organic molecules [197]. If LDA/GGA results turn out to achieve satisfied accuracy, then they would have saved large amount of computational cost and time, which are quite important factors for material informatics or automated materials searching.

On the other hand, B3LYP functional is an improvement of LDA and GGA. While LDA and GGA yield their total energies from just electronic density, B3LYP has corrected that and

improved its approximation to the XC energy term of the total energy over the system of electrons. B3LYP may have the benefits of more accuracy in calculating the actual total energy because it has also included a nearly exact expression for the exchange components. Moreover, B3LYP is often the selected method for calculating standard chemical models for many applications [198]. Therefore, among the three functionals within this work, the predictions by B3LYP would be considered as the most reliability.

However for the interpretations of sparse systems or layered structures as conducted in this dissertation, strong local bonds and the weak non-local van der Waals (vdW) interactions, with containing separated empty space between interlayers, should also be included and taken into account [213] because the conventional local (LDA) and semilocal (GGA) approximations are limited to described the vdW forces [214]. In contrast to LDA or GGA, the correlation energy of vdW-DF also possesses with the non-local dependent term on the density. This non-local correlation is added to the exchange and correlation energy while using the correlation term of LDA and exchange term of GGA [214]. For extent within this study on the stacking, the van der Waals functional must be required for better evaluations of the systems. The additional information about vdW-DF method is included in the section §D.3.4 of Appendix D.

5.3 CoPc as Stable Attracted Material

From the present calculations, the formation results of CoPc layer attracted on basal graphene sheet shown the most stability which will be further discussed in subsection §5.3.1 and §5.3.3.

5.3.1 Plots of Relative Binding Energy

The binding energies from computational results of TMPcs on graphene sheet, as depicted in Figure 5.1. The attractions of each TMPc layer on the graphene sheet have been evaluated in term of the binding energies (E_{bind}) between them. The general expression for the E_{bind} calculation is defined as

$$E_{bind} = E_{MPc/G} - [E_{MPc} + E_G] \tag{5.1}$$

The results for calculated E_{bind} are previously summarized in Table 4.16, and displayed as relative binding energy in Figure 5.1. In order to describe proper trend and for comparison of their stabilities, the energy differences were relatively taken with respect to those of CoPc/G since the results shown in Table 4.16 pointed out that, under same XC functional, CoPc/G possesses the lowest among selected TMPcs, except the B3LYP results of MnPc/G. Therefore, the binding energy of CoPc/G is chosen as a reference where the 'zero' value placed within the plot. The positive larger values of binding energy obtained from the same XC functional indicate that the binding energies of other TMPcs/G are higher than that of CoPc/G which lead to less stable structures. From the plots, CoPc attracted on graphene sheet, thus, is the most stable structure suggesting that these would be stable in experimental conditions.

From the plot, it can be seen that the prediction depends on the choice of selected XC functionals, where the results obtained from PBE and B3LYP share similar trend while those from
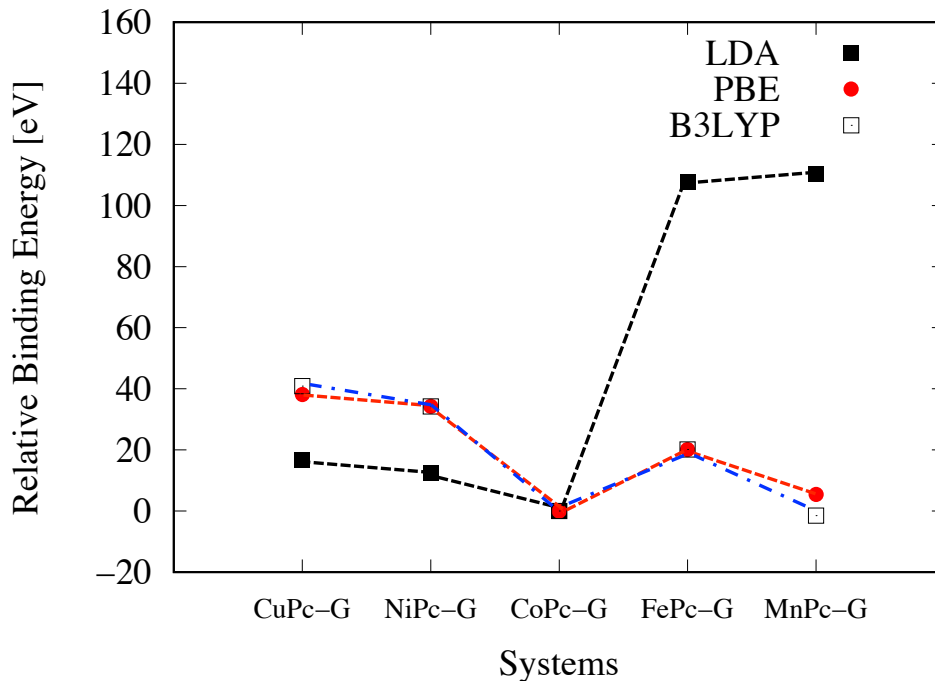
Figure 5.1: The plots of relative binding energies of metal phthalocyanines on graphene sheet from the prediction of different exchange-correlation functionals. The relative stability among MnPc, FePc, CoPc, NiPc, and CuPc over the graphene sheet are predicted. The lower the more stable, where zero is defined for comparative energy respected to CoPc/G.

LDA shows several fluctuated ones. This might due to the scattered evidence in the literature that lead toward LDA may provide the good estimation for σ but either overestimated or underestimated for layered structures where weakly vdW interactions are considerably involved. The role of XC functionals in this work for evaluated stability of TMPc/G must be taken this into account. While method of choice in this approach may be less satisfactory for the intellectual point of views, but it may gain pragmatic informatics. The more accurate choices of specific functionals could be deployed to cover what have left behind by this work.

For a series of experimental works, CoPc behaves, as an active-guest material with π-domain, is strongly attracted to the π-π stacking onto graphene sheet, as a host electrode, interaction. Yang *et al.* reported that both of their former experimental productions of CoPc with the extended π-electron system could be adsorbed onto graphene-layered materials [215, 216]. They stated that their composite-layered material was characterized by UV-vis absorption spectroscopy, indicating a strong π-π interaction between CoPc and graphene.

In another work, Cui *et al.* prepared the CoPc/G by layer-by-layer (LBL) technique, and analyzed the surface morphology of this composite film that performed the characterization by using the atomic force microscope (AFM) and the scanning electron microscopy (SEM). They have found that CoPc/G had showed the satisfaction in long-term stability [217].

Zagal *et al.* have experimentally produced many aspects of CoPc complexes on different types of graphite surfaces with various preparation of processes for graphite-based electrodes,

Figure 5.2: The HOMO-LUMO orbital distributions of the completely isolated CuPc and CoPc before their interactions onto graphene sheet. The results obtained from LDA calculation.

such as glassy carbon electrode (GCE), ordinary pyrolytic graphite electrodes (OPGE), basal-plane pyrolytic graphite (BPG), vitreous carbon electrode (VCE), screen printed carbon electrode (SPCE), and carbon microelectrode (CME). CoPc has shown its strongly adsorption and immobilization on the basal graphite electrodes. They stated in their finding that the CoN_4 in the central cavity of CoPc is significantly influent the chemical reaction, and this influence is also true for other metals in the TMPcs, but CoPc yields the good adsorption [45].

Therefore from the prediction of CoPc for the strongest anchoring on graphene, the production of CoPc/G electrode process would lead to the possible construction of these electrodes in the laboratory scale with self-assembled monolayers (SAMs) technique. Even though in the typical productions, the attractions of monolayers of TMPc are simply fabricated by submerging the target electrode into appropriate solutions that containing TMPc complexes, or adding this solution directly on the surface of the target electrode. Then, the TMPc layers that are not attracted or unnecessary wanted on the surface can be cleansed and eliminated by rinsing them off with ethanol solvents [45].

5.3.2 Comparation of CoPc and CuPc

The spin state of both Co and Cu are S = 1/2, and then both CoPc and CuPc posses a single unpaired d electron, and then there are two possibilities of the self-spin states, α and β, for each of them as mentioned in subsection §4.2.2. Under D_{4h} point group, the metal d orbitals transform as $a_{1g}(d_{z^2})$, $b_{1g}(d_{x^2-y^2})$, $e_g(d_{zx}, d_{yz})$, and $b_{2g}(d_{xy})$. The molecule would lie in the xy plane, the d_{xz}, d_{yz} orbitals have π type and the rest may be considered of σ one.
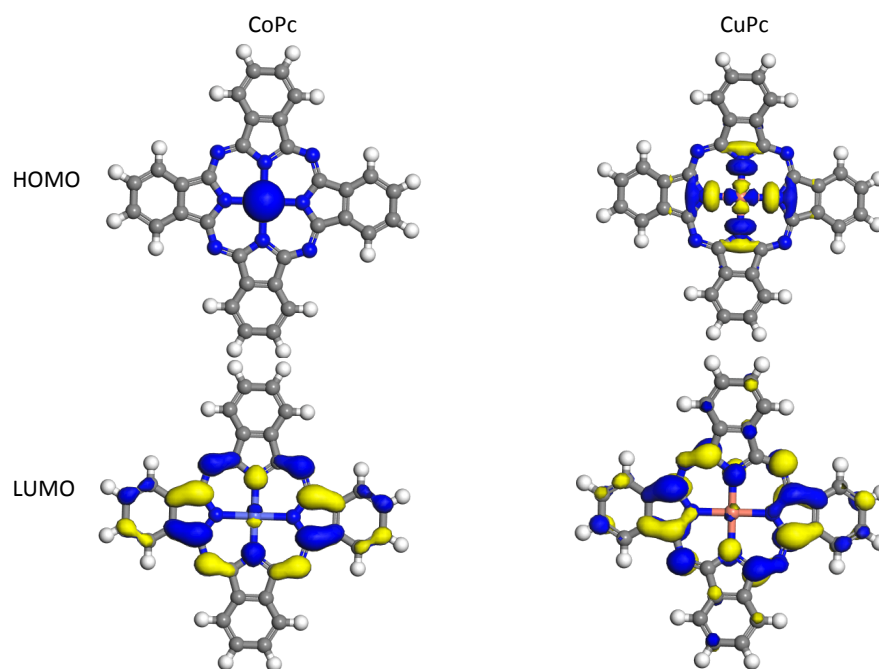
Figure 5.3: The HOMO-LUMO orbital distributions of the completely isolated CuPc and CoPc before their interactions onto graphene sheet. The results obtained from PBE calculation.
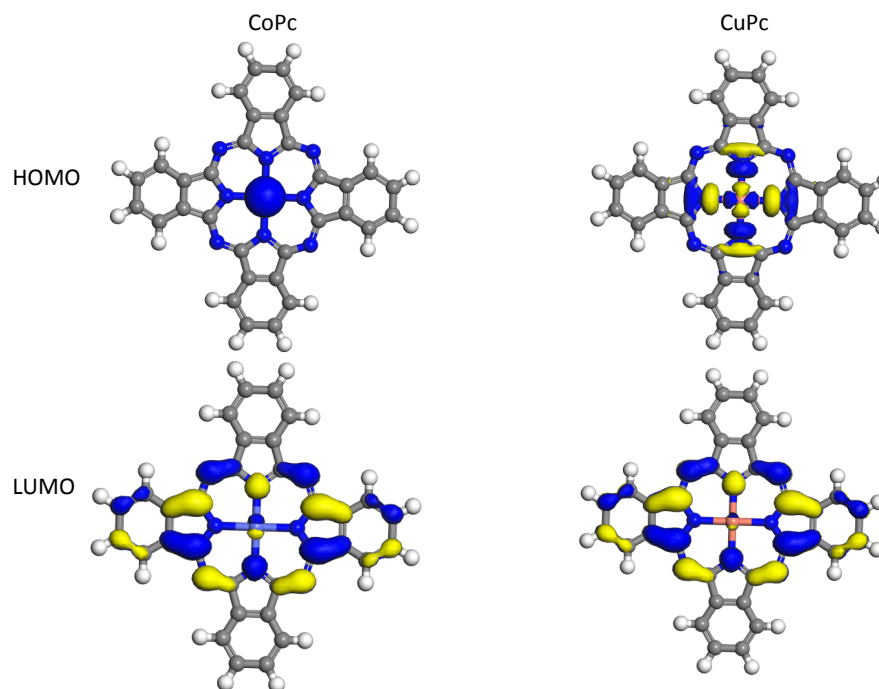
Figure 5.4: The HOMO-LUMO orbital distributions of the completely isolated CuPc and CoPc before their interactions onto graphene sheet. The results obtained from B3LYP calculation.
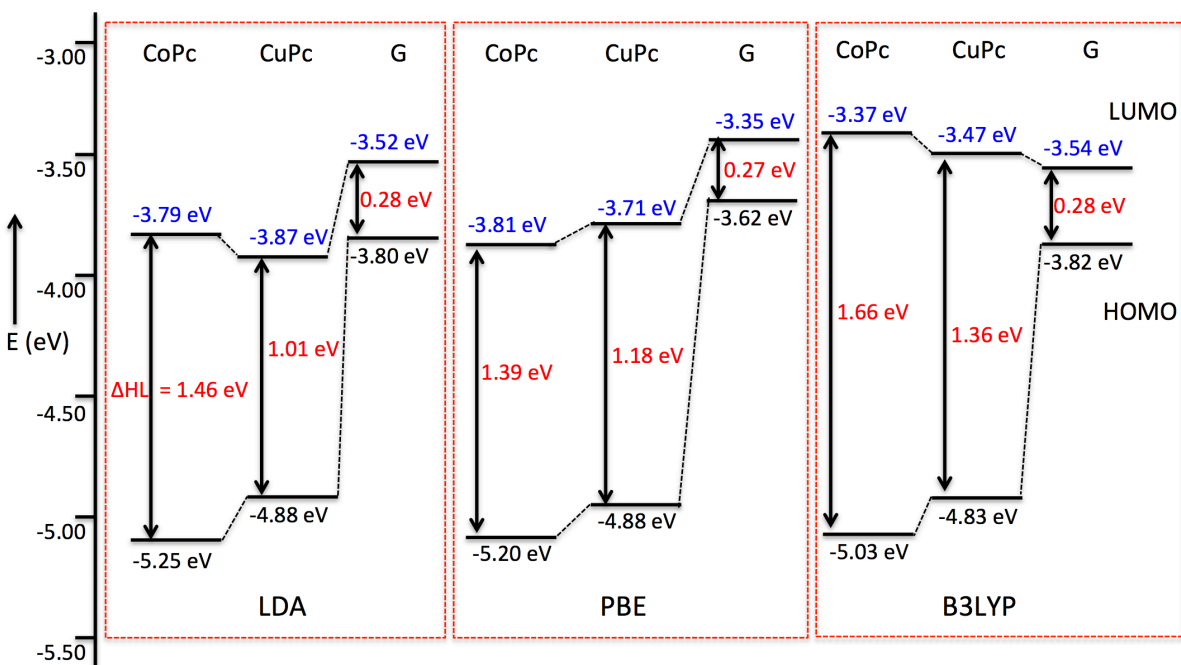
Figure 5.5: The energy level alignment diagrams of the completely isolated CoPc, CuPc, and graphene before their interactions. The HOMO-LUMO gaps (*ΔHL*) of CoPc are larger than CuPc in all obtained results from selected different exchange-correlation functionals. G is graphene that optimized for couple system.
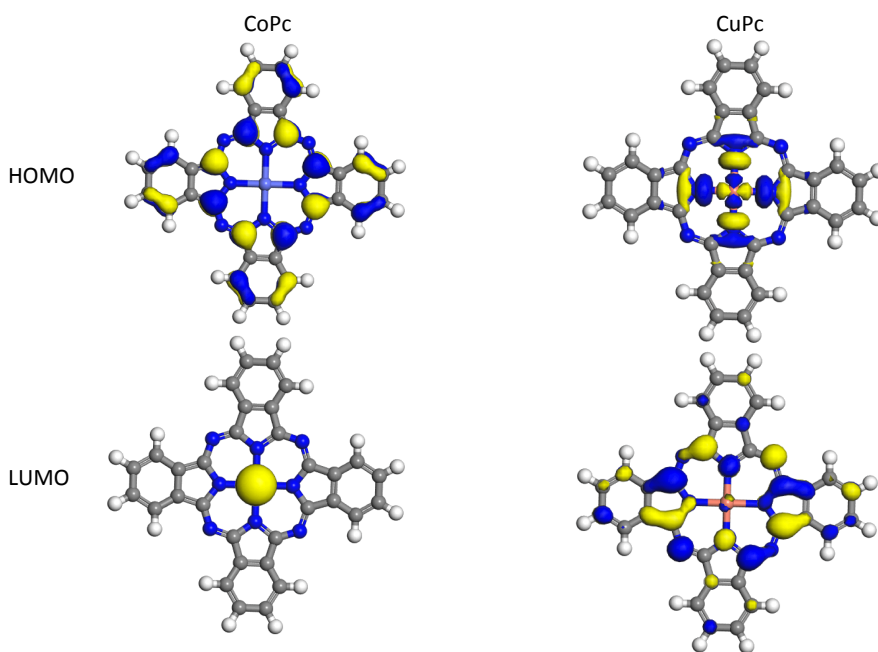
Figure 5.6: The HOMO-LUMO orbital distributions of the isolated CuPc and CoPc after their interactions onto graphene sheet. The results obtained from LDA calculation.

51
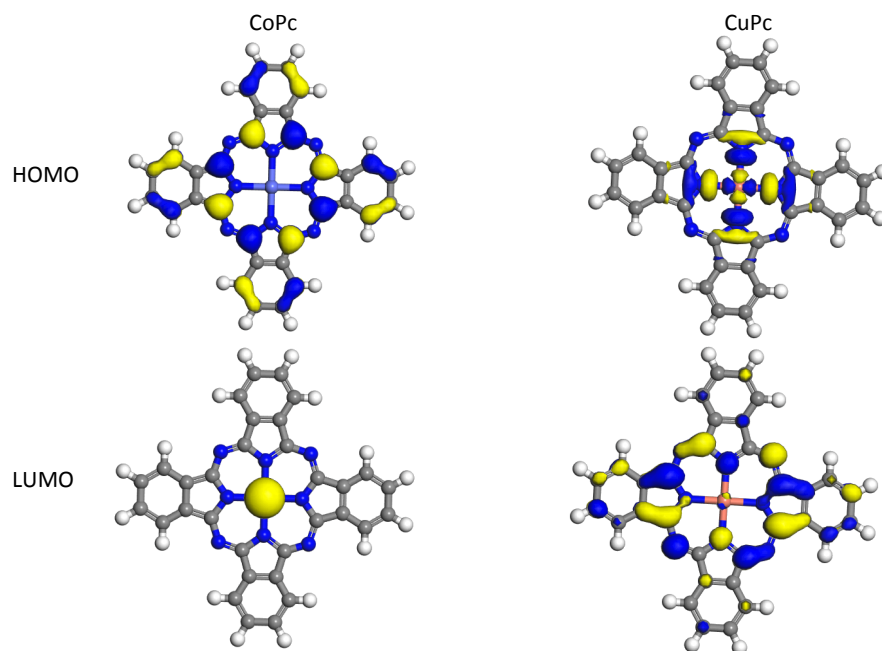
Figure 5.7: The HOMO-LUMO orbital distributions of the completely isolated CuPc and CoPc after their interactions onto graphene sheet. The results obtained from PBE calculation.
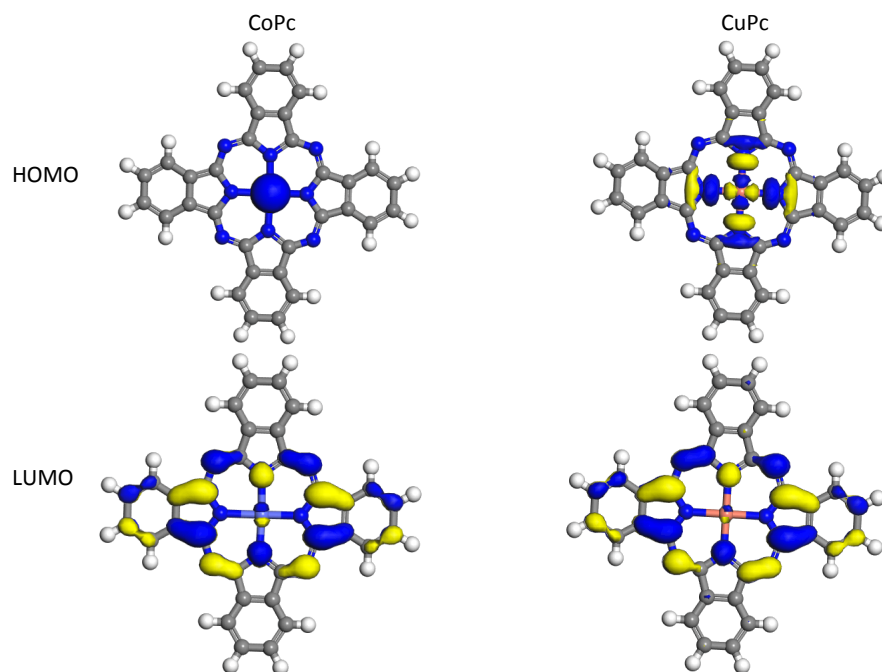
Figure 5.8: The HOMO-LUMO orbital distributions of the completely isolated CuPc and CoPc after their interactions onto graphene sheet. The results obtained from B3LYP calculation.
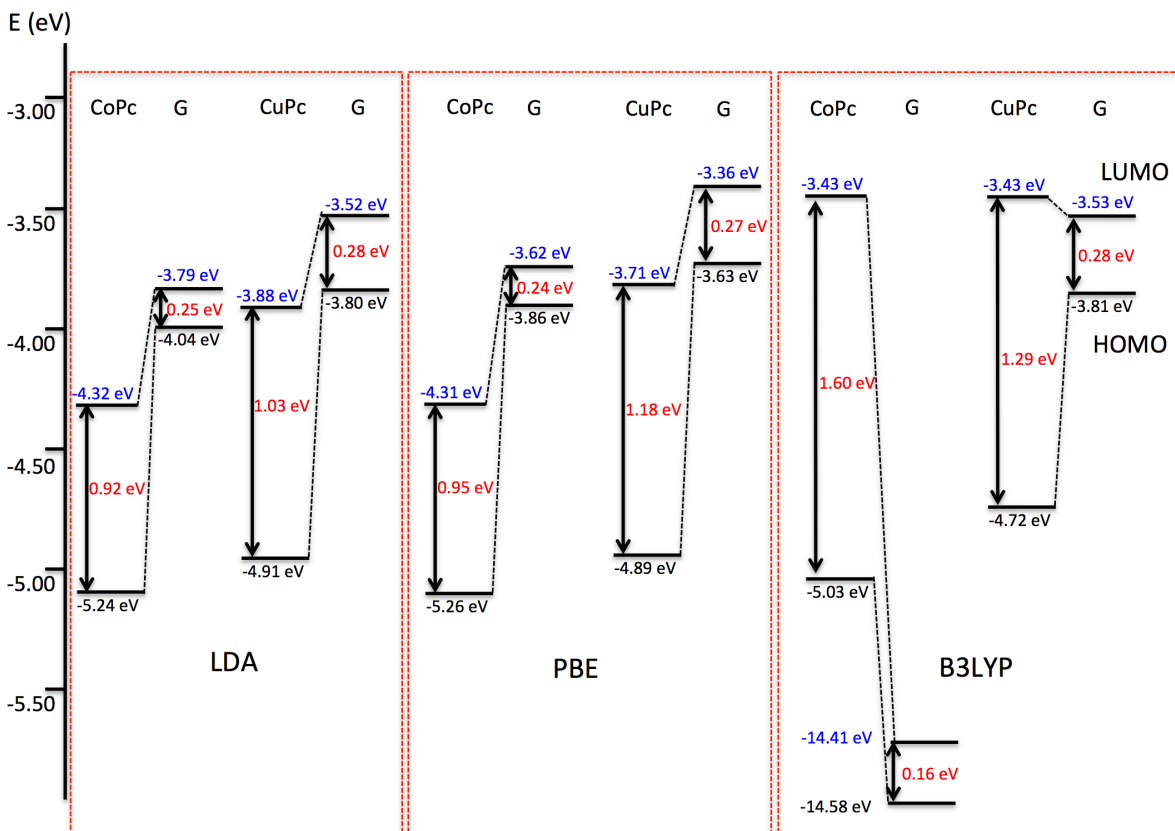
Figure 5.9: The energy level alignment diagrams of the isolated CoPc, CuPc, and graphene after their interactions obtained results from selected different exchange-correlation functionals. G is graphene that optimized for couple system.
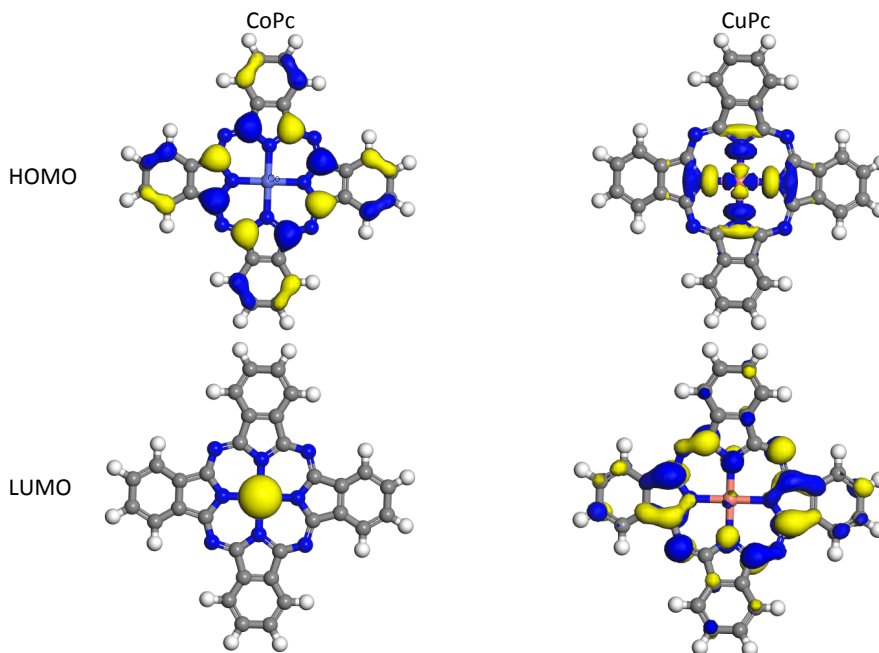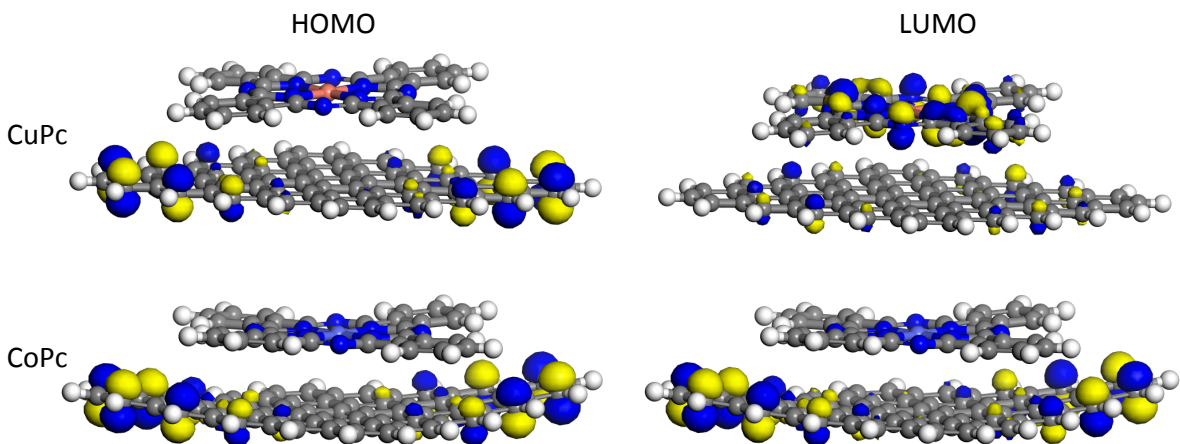
Figure 5.10: The HOMO-LUMO orbital distributions of CuPc and CoPc on graphene sheet for observation due to their obvious differences in relative energy for CoPc/G is more stable, and the other is less. The isosurfaces of the HOMO-1 (top) and LUMO (bottom) are included, where the color mapping that blue indicates positive, and yellow indicates negative.

From the Figure 5.5, the larger HOMO-LUMO gaps (ΔHL) lead to the possibility of the more stable formation. The Figure 5.5 indicates that the completely isolated CoPc molecules have larger ΔHL gap than all those of CuPc. The HOMO and LUMO distributions of the completely isolated CuPc before-graphene interaction are in good agreement with the after-graphene case within all the three XC functionals (see Figure 5.2, 5.3, 5.4 5.6, 5.7, and 5.8 for comparison).

In contrast, CoPc has one of the $a_{1g}(d_{z^2})$ electron is available, and the empty b_{1g} orbital, which is largely composed of $d_{x^2-y^2}$. The HOMO-LUMO distribution of CoPc obtained from B3LYP functional in after-graphene interaction (see Figure 5.8) is able to reproduced the $a_{1g}(d_{z^2})$ electron in HOMO state as same as the PBE and B3LYP results from the before-graphene cases (see Figure 5.3 and 5.4). This may possibly lead to the reliability of B3LYP functional in our calculations. However, the computational HOMO-LUMO results from LDA has noticeably failed to represent the $a_{1g}(d_{z^2})$ of CoPc, but PBE and B3LYP achieved to reproduce this state so LDA may not be a preferable XC choice for calculation of both energy and orbital distribution.

5.3.3 HOMO Orbital Distributions

The sp^2 orbitals on graphene sheet, the σ bonds are formed in parallel to the graphene surface, and each carbon atom are connected and arranged in hexagonal lattice. The p_z orbitals, perpendicular to the graphene sheet, are left to rise in delocalized π bonding and π^* antibonding states. From the plot of relative binding energy in Figure 5.1, the CuPc/G is considerably picked for further evaluation and in comparison with CoPc/G because it is clearly observed that the trend in all three XC functionals show in similar direction.

Molecular orbital energies, highest occupied molecular orbital (HOMO) and lowest unoccupied molecular orbital (LUMO) distributions, calculated with the selected functionals for
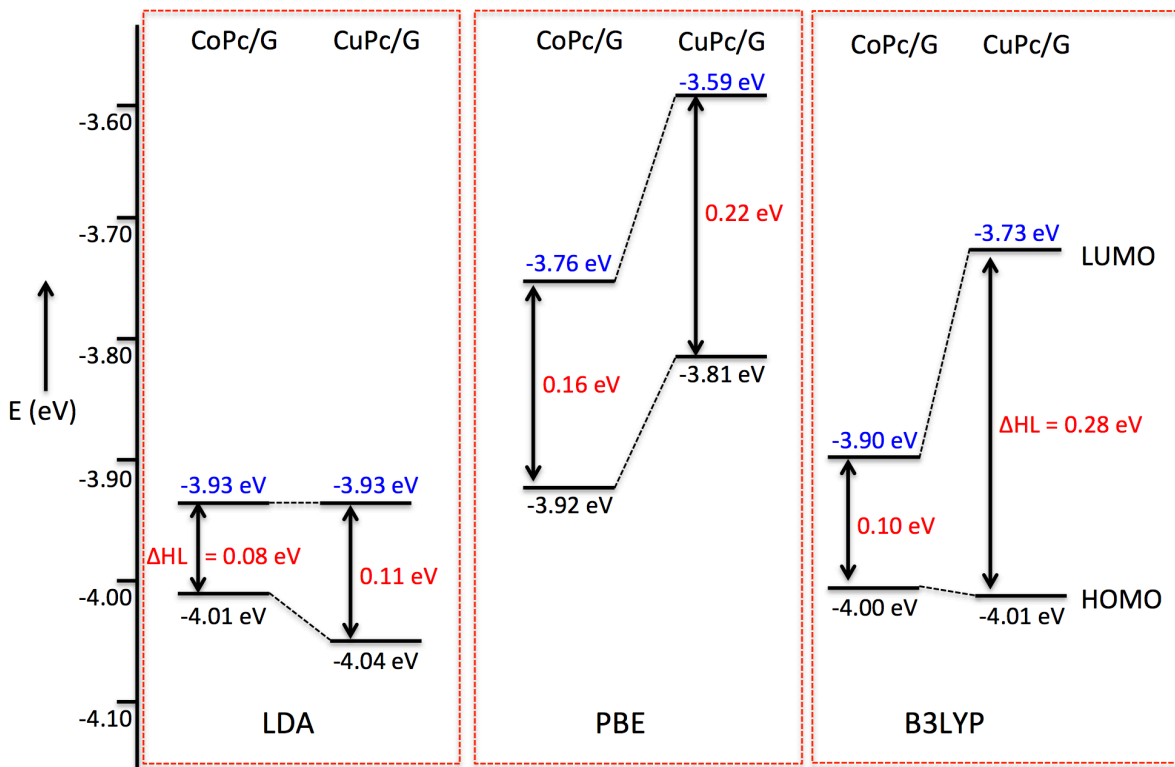
Figure 5.11: The energy level alignment diagrams of the CoPc/G and CuPc/G interlayers. The HOMO-LUMO gaps (*ΔHL*) of CoPc/G are smaller than CuPc/G in all obtained results from selected different exchange-correlation functionals.
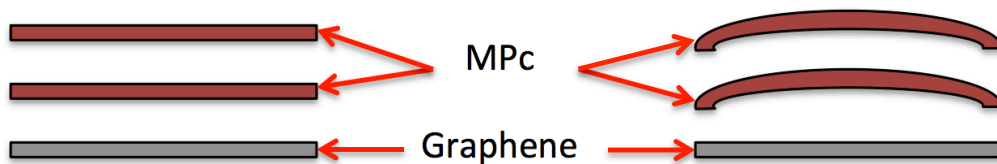
Figure 5.12: The considerable deformation in TMPc stacking layers on graphene sheet.

CoPc/G and CuPc/G. While HOMO-LUMO gaps are listed in Table 4.8 and 4.14, respectively. Then, their molecular isosurfaces are visualized in Figure 5.10. The HOMO of CuPc/G is mainly on the graphene sheet where surrounded the edge of Pc ring, while its LUMO is localized on the Pc ring.

CoPc has one of the $a_{1g}(d_{z^2})$ electron is available, and the empty b_{1g} orbital, which is largely composed of $d_{x^2-y^2}$. The CoPc states e_g are mixed due to hybridization, the interaction between the CoPc and graphene, one electron from the $a_{1g}(d_{z^2})$ would transferred from graphene. This suggestion comes from the charge transfer between the d^7 Co configuration and graphene through the d_{z^2} orbital. This may lead to one of the possible reason for intermediate formation between CoPc and graphene strong interaction. In contrast, CuPc is also having one electron available, but in the $b_{1g}(d_{x^2-y^2})$ orbital. This implies that for a considerable CuPc and the graphene in π-π band by the LUMO of CuPc and localized to the central Cu atom of the molecule and Pc ring, see Figure 5.10. This might also imply that an electron transfer from graphene to the Cu-related LUMO state of CuPc upon adsorption. Therefore, CoPc gains more benefit of its $a_{1g}(d_{z^2})$ orbital for such π-π interactions better than CuPc or other TMPcs. The finding is very good agreement with the experiment conducted by Jarvinen *et al.* [195].

The schematic of energy level diagrams obtained from these results are shown in Figure 5.11. The HOMO-LUMO gaps (ΔHL) of two TMPc/G interlayers are 0.08 (LDA), 0.16 (PBE), and 0.10 (B3LYP) eV for CoPc and 0.11 (LDA), 0.22 (PBE), and 0.28 (B3LYP) eV for CuPc. LDA gap is underestimated; this is consistent with the common understanding or expectations. The model leads the relation between the gap and energy level alignment at CoPc/G interfaces has the comparatively lower values than those of CuPc/G in all results, indicating that the latter is more difficult to accept electrons. These differences in energy between the HOMO-LUMO gaps can be used to predict the strength and stability of these evaluated complexes. Due to the interaction is proportional to the HOMO-LUMO energy gap inversely, the interaction of CoPc layer on basal graphene sheet is in favor with more attraction and stability as its energies of HOMO-LUMO gaps are smaller than other selected TMPcs/G. Note that the larger HOMO-LUMO gap also leads to more difficult in charge transfer, and also poorer reactivity [218].

5.4   Distortion Estimations

From the computational results and experimental data [215, 216], they indicate that TMPcs can be settled on graphene sheet as discussed in the previous section 5.6. Most of the TMPcs will be attracted and immobilized at the hexagonal site, centering in one of the benzene ring except CuPc and MnPc that are slightly off the central grid.
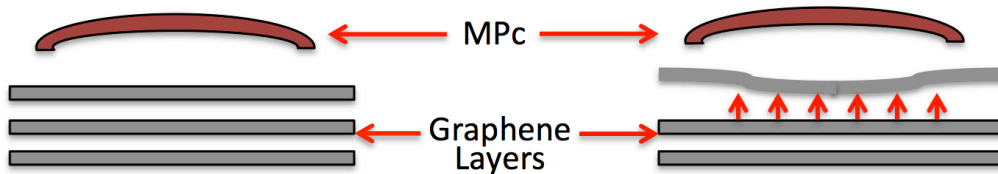
Figure 5.13: The deformation of TMPc layers lead to damaging in graphene substrate.

In addition, the geometry optimization of TMPcs/G from computational results shows that the initial planar structures of TMPcs/G interlayered electrodes have been deformed in some cases. For the case of NiPc/G, the edges of graphene sheet are bent toward the NiPc monomer from the PBE and B3LYP results while there are no such noticeably change in NiPc structures from all other obtained results. This might be possibility to have strong artifact on the distortion estimations due to too small size of graphene fragment, only 25 benzene rings. However in contrast, there are also some cases that the graphene sheets are still in flat shape, but TMPcs structures are distorted after their geometry have been optimized, such as FePc and MnPc.

In order to overcome such a problem for the next calculation, one of the possibilities is to increase the size of graphene sheet to be much greater than this current setup. At least more than 81 benzene rings would probably be more appropriate to place TMPc within the sheet. Another possibility is to perform TMPc geometry optimization on a finite fragment but larger graphene sheet than the current one. However, the planar structure of graphene fragment should be fixed as an electrode substrate because the production of TMPcs/G in reality, the graphene sheet would be stationary attached to metal sheet while additional layer of TMPcs will be attracted later during their fabrication process. There is also a feasibility for the calculations of periodic boundary condition by using CASTEP software package. It might be easier to achieve the convergence than the treatment in the current work.

The evaluation of their structural distortion is important and required for taking into account because the deformation of the graphene fragment in calculation modeling in this work would lead to the deformation of the composite materials in reality, and the life span/cycle of electrodes will be shortened. A quick approach possibly suggested to investigate for layer stacking is to perform geometry optimization of each TMPcs/G layer. If there are considerable deformations in TMPc structure, then more stacking of TMPc get difficult, as depicted in Figure 5.12.

On the other hand, when the deformation occurred as spatially non-uniform force to graphene substrate, this particular case would lead to substrate damaging where graphene would be eventually peeled off by TMPc layer, and then shortened in electrode life span, as illustrated Figure 5.13.

5.5 Twisted Angle between TMPcs and Graphene

In the recent review by Zhong *et al.* [219], they reported on the molecular orientation investigating the alignment of CuPc and graphite. As a confirmation that the π-π interactions have aided
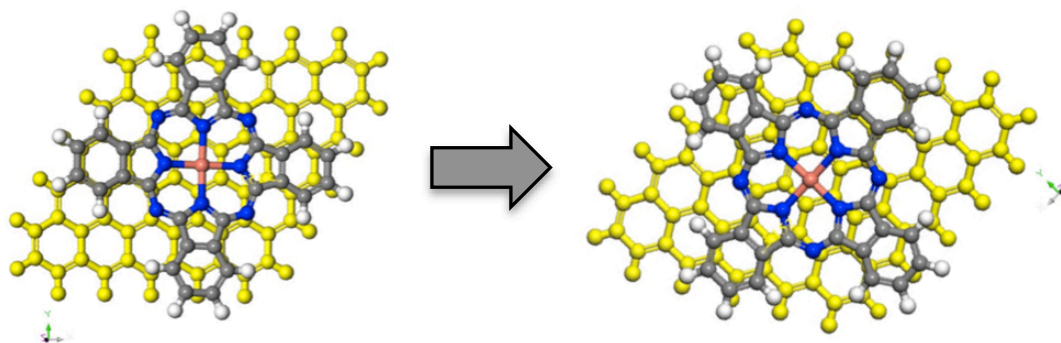
Figure 5.14: The twisted-angle model between TMPc and graphene that will be used for further investigation.

in keeping the interlayered configuration of molecule-substrate plane at lying flat directly from the interfacial interactions CuPc and graphite, and this results also caused from dominating by weakly van der Waals forces. They also confirmed that instead of graphite, even just monolayer of graphene, it would realize the same outcome affecting to manipulate their orientations.

The work has been supported the results from the investigation by Salzmann *et al.* on the epitaxial growth of π-stacked molecule on graphene coated quartz, as the substrate [220]. They observed that the standing configuration of π-stacked molecules on bare substrate can be prevented by the adding of graphite/graphene sheet upon the formation of physical contact between the basal layers of coated graphene and the attracted layer.

Even though the former experimental works [219, 220] indicate the strong interlayered formations in 'lying-flat' shapes, but those were meant to investigate the interfaces in the vertical direction of molecules and substrates. In this dissertation for further study, the twisted angle between TMPc molecules and graphene plane should also be taken into account in order to examine whether the prediction in the current work will be kept unchanged. Figure 5.14 is the twisted-angle model of TMPc/graphene that will be used for further investigation.

5.6 Functionalized Graphene

There are several approaches to continuous the research within this dissertation. One approach is to investigate about functionalized graphene or graphene oxide (GO) as depicted in Figure 5.15, and vacancy graphene as depicted in Figure 5.16. They are known to be available and occurred during graphene preparation and production processes. These functionalized graphene models will used as basal substrate where CoPc as an attracted layer, and perform
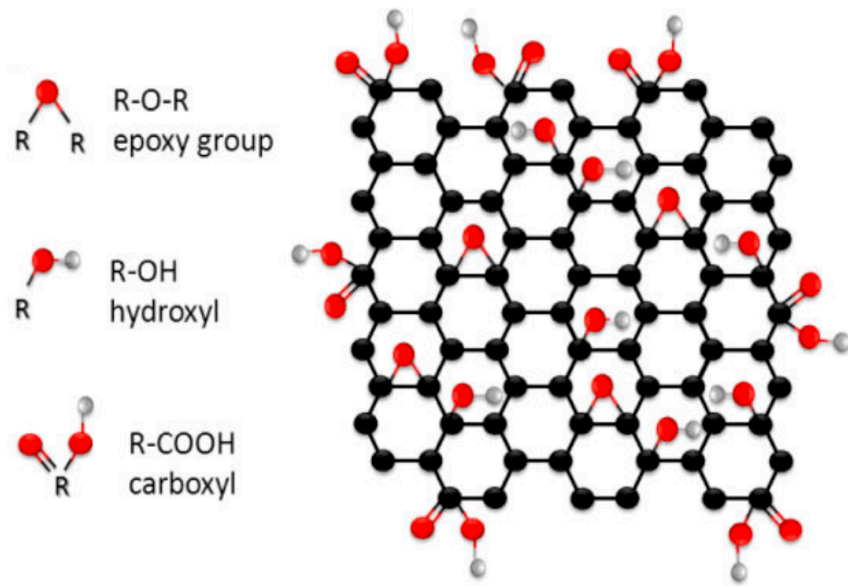
Figure 5.15: Graphene oxide with epoxy, hydroxyl, and carboxyl group.
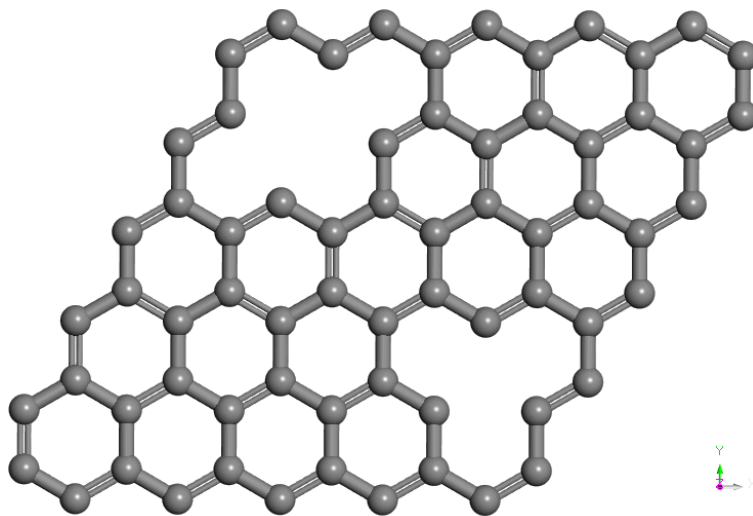
Figure 5.16: Molecular structure of vacancies in graphene sheet.

the re-calculations in comparison with pristine graphene case.

And last, the information of TMPcs and graphene interlayered formation obtained within this dissertation and further work will be used to produce these composite electrodes in laboratory scale. The experimental measurement of their surface stability will also be examined and evaluated in comparison with our computational data.

Appendix A

Symbols and Units

In this appendix A, the conversion factors between atomic units and SI units are presented in Table A.1 and A.2. The tabulations of all symbols that have been used throughout this thesis, are categorized and presented in the following tables.

Table A.1: Conversion from SI units to atomic units.

Quantity	SI value	Atomic Units
Mass	$9.109\ 534 \times 10^{-31}$ kg	$m_e = 1$
Charge	$1.602\ 189\ 2 \times 10^{-19}$ C	$|e| = 1$
Angular Momentum	$1.054\ 588 \times 10^{-34}$ J s	$\hbar = 1$
Permittivity	$1.113\ 65 \times 10^{-10}$	$\kappa = 4\pi\epsilon_0 = 1$
Length	$5.291\ 772\ 49 \times 10^{-11}$ m	$\kappa\hbar^2/me^2 = a_0 = 1$ (Bohr)
Energy	$27.211\ 4$ eV	$e^2/\kappa a_0 = 1$ (Hartree)
Electric Potential	27.11 V	$e/\kappa a_0 = 1$

Table A.2: Conversion factors for energy units.

Joule	kJ·mol^{-1}	eV	au	cm^{-1}	Hz
1 Joule = 1	6.022×10^{20}	6.242×10^{18}	2.2939×10^{17}	5.035×10^{22}	1.509×10^{33}
1 kJ·mol^{-1} = 1.661×10^{-21}	1	1.036×10^{-2}	3.089×10^{-4}	83.60	2.506×10^{12}
1 eV = 1.602×10^{-19}	96.48	1	3.675×10^{-2}	8065	2.418×10^{14}
1 au = 4.359×10^{-18}	2625	27.21	1	2.195×10^{5}	6.580×10^{15}
1 cm^{-1} = 1.986×10^{-23}	1.196×10^{-2}	1.240×10^{-4}	4.556×10^{-6}	1	2.998×10^{10}
1 Hz = 6.626×10^{-34}	3.990×10^{-13}	4.136×10^{-15}	1.520×10^{-16}	3.336×10^{-11}	1

Table A.3: Symbols of variables.

Symbol	Quantity
C	Capacitance
Q	Store positive charge
V	Applied voltage
A	Surface area
D	Distance between electrodes
E	Energy stored in capacitor
P	Power of capacitor
R	External load resistance
A_{uc}	Area of unit cell
E_0	Electric field strength
$\vec{r}$	Spatial coordinate
r_0	Equilibrium internuclear distance
$\hat{H}$	Hamiltonian operator
$\hat{T}$	Kinetic energy
$\hat{V}_{int}$	potential energy due to the internal forces
$V_{ext}(r)$	Potential energy due to the external forces
$\hat{T}_s$	Kinetic energy of the independent particles
$E_{Hartree}$	Self interaction energy of the electronic density
E_{xc}	Exchange-correlation energy

Table A.4: Symbols of constants.

Symbol	Quantity
a_0	Bohr radius
ϵ_0	Dielectric constant or permittivity of free space
ϵ_r	Dielectric constant of insulating material
$\hbar$	Planck's constant
k_B	Boltzmann constant

Appendix B

Supercapacitors

In general for conventional capacitors, they typically have two conducting electrodes. These electrodes are insulated and separated by an dielectric insulator in each cell as illustrated in Figure B.1. The opposite charges will accordingly be collected on the each surface of electrodes as a potential was presented across capacitor. As those charges are separated by dielectric material; therefore, an internal electric field is produced in such that the capacitor is able to store the produced energy. The occurrence of this phenomenon is demonstrated in Figure B.1.

The capacitance C can be fundamentally defined as the proportion of the stored positive charge Q and the applied voltage V. Their relationship can be indicated as

$$C = \frac{Q}{V} \tag{B.1}$$

Furthermore, for capacitance C, its magnitude is also mainly depending on each surface area A of the two electrodes, and it is inverse to the distance D between those two electrodes:

$$C = \epsilon_0 \epsilon_r \frac{A}{D} \tag{B.2}$$

On the right-hand side, the equation B.2 shows the product of the first two factors is the constants, where ϵ_0 is the dielectric constant of free space, and ϵ_r is the dielectric constant of the insulator between the two electrodes.

The energy and power density are outstanding characteristics of a capacitor. For the case of energy E, it can be measured its value by per unit volume or mass. Then, the stored energy E of a capacitor is mainly depending on its capacitance magnitude as in the equation B.3:

$$E = \frac{1}{2}CV^2 \tag{B.3}$$

And for the power P, it can be calculated as the energy per unit time. In order to calculate power P for a capacitor, the capacitors are generally considered to be presented as a seried circuit with a load resistance R, illustrated in Figure B.1.

The internal elements of a conventional capacitor, for example electrodes, dielectric material, and current collectors, can together be contributed to the internal resistance determined in
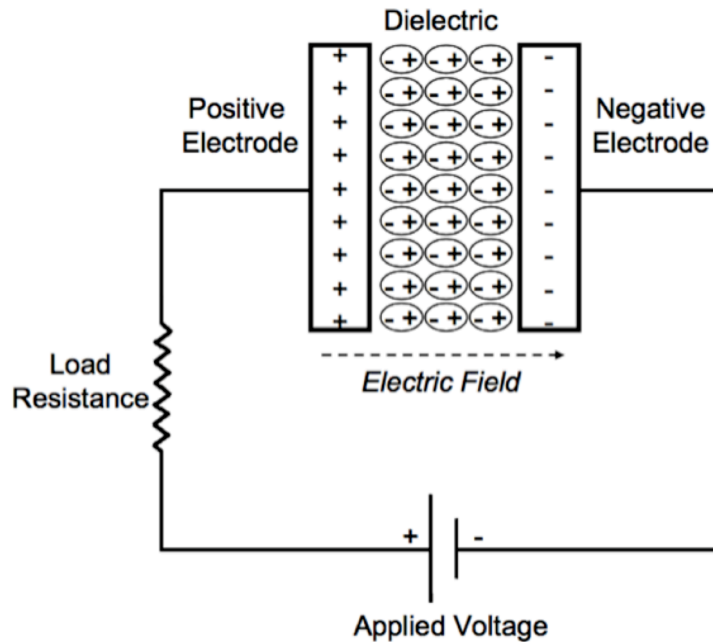
Figure B.1: Schematic of the separated charges between parallel-plate of electrodes, causing an electric field in capacitor.

conclusion by a quantitive values as the equivalent series resistance (ESR). During discharging, the voltage is assigned by this ESR. For measurement of the impedance as $R = ESR$, the maximum value of P_{max} in a capacitor [15, 16] can be calculated by:

$$P_{max} = \frac{V^2}{4ESR} \tag{B.4}$$

This relationship can also lead to the suggestion that how the ESR has a significant impact that can limit the capacitance power to achieve its true potential.

In most cases, the capacitors have normally high power densities; however, they also have relatively low energy densities in comparison to fuel cells and those electrochemical batteries. In principle, a battery is able to store its total energy as high as a capacitor and more, unfortunately, it cannot discharge itself fast enough. It is meaning that the power is comparatively low than the expectation. Besides, the capacitors can keep lower energy per unit volume (per unit mass); however, their electrical energy storage should be delivered promptly to reach excessive power; therefore, their power is normally high.

In general, supercapacitors are determined by the fundamental principles as same as the capacitors. But somehow, their incorporated electrodes possess larger and larger surface areas A along with their dielectrics have smaller gap in which have directly affected on decreasing the distance D between the electrodes. Therefore, from previous equations B.2 and B.3, they initiatively lead to both the increase in the capacitance and elevated the energy.

By intentionally keep the resistance ESR of capacitors at low values; supercapacitors should expectedly be able to reach the comparative power densities. In addition, supercapacitors have
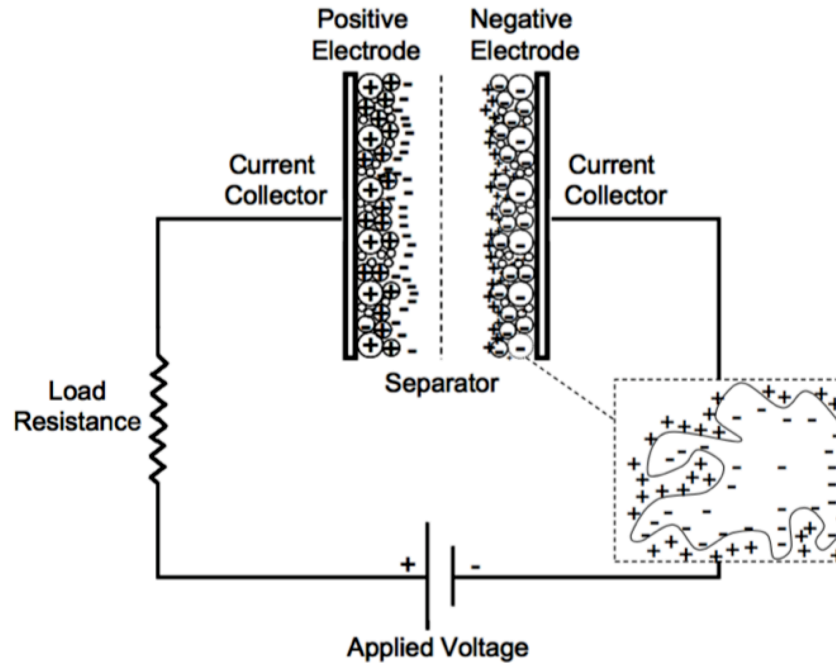
Figure B.2: Electrical double layer capacitors (EDLC).

several other advantages above fuel cells or electrochemical batteries including that they possess larger power density, longer cycle life, shelf life, and shorter charging times [4, 15]. The diagrams of supercapacitor described previously are provided in Figure B.2.

The improvement and performance for supercapacitors shown according to a plot of energy storage amongst different devices are presented in Figure B.3. This type of the Ragone plot represents the energy density measured in Wh/kg in the horizontal axis versus the power densities measured in W/kg along the vertical axis of various energy storage devices. Figure B.3 demonstrates that supercapacitors have occupied in a region between batteries and conventional capacitors [4]. Even though supercapacitors have larger capacitance than regular capacitors, they are still not matched in the range of energies from the middle to high-end fuel cells and batteries yet. Therefore, the main goal of many research groups expectedly aims to develop the improved types of supercapacitors for producing the better energies comparatively with batteries. Therefore, these details and tendency are notably shown as the reflection in the classification of supercapacitors presented in this Appendix B.

Based upon the tendencies of recent studies, supercapacitors can typically be categorized into 3 general classes: electrochemical double-layer capacitors (EDLCs), pseudocapacitors, and hybrid supercapacitors as shown as the chart of graphical classification in Figure B.4. These types of supercapacitors are classified by each of their outstanding characteristics for collecting charges. These are faradaic, non-faradaic, and together of these two, respectively. Faradaic processes the oxidation-reduction reactions with related to the charge transfer between electrolyte and electrodes. On the other hand, the non-faradaic processes are not involved with any chemical reactions, but its charges are physically gathering on surfaces of electrodes instead of involving neither creating nor breaking of any chemical bonds.
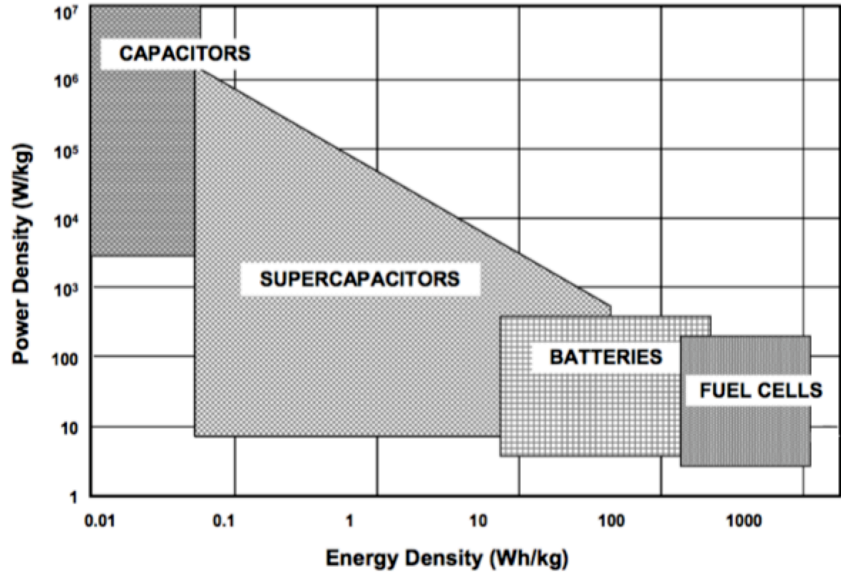
Figure B.3: Ragone plot of energy storage devices, reprinted from reference [4].

In the next subsections, each of these classes of supercapacitors and subclasses will be distinguished and summarized which based on their electrode materials. Figure B.4 presents the graphical classification with the different classes of supercapacitors.

1. **Electrochemical Double-Layer Capacitors**

   The electrochemical double-layer capacitors (EDLC) have been main sources for various energy storage devices. Carbon materials are known to possess a very high specific surface area (SSA). For EDLCs, it is considered to be important factor leading to a greater gravimetric capacitance (C_g) [221]. Due to the fact, energy of EDLCs is less than recharged batteries. The EDLC capacitance is needed to upgrade to be increased. Therefore, to optimize the porous structures with size distributions and surface factors would be one of the main target researches of EDLCs.

   An EDLC is typically built from two carbon-based electrodes, an electrolyte solution, and a separator. Figure B.2 in previous section demonstrates a diagram of this capacitor. Similar to typical capacitors, EDLC stores charges electrostatically, or non-faradaically, and there is no charge transfer between electrodes and electrolyte. EDLC utilizes an electrochemical double-layer of charges to produce the energy. When applied voltage across electrodes, charges are collected on the surface of each electrodes. By attracted force of different charges, the electrolyte ions will be diffused through separator and then resided in the porous electrode of opposite charges. The electrodes are designed to block these ions from recombining. Consequently, the double-layered charges is created on the surface of each electrodes. They would be coupled along not only increased surface areas of electrodes but also decreased gap between them. That will effectively lead the EDLC to reach higher energies than those typical capacitors [4, 15].
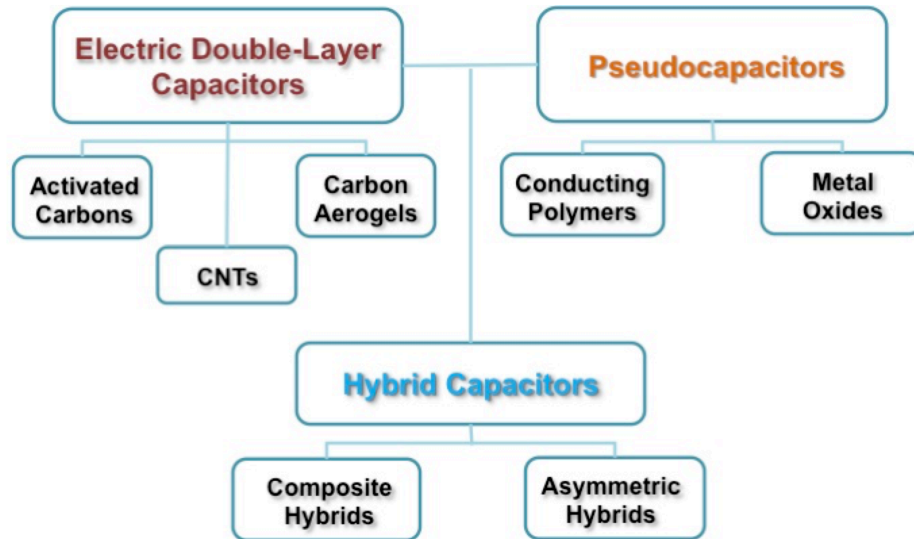
Figure B.4: Classification of supercapacitors.

There are no composition or chemical changes associated with non-faradaic methods since there is no charge transfer between electrodes and electrolyte. Due to this reason, stored charge in the EDLC can be greatly reversible, but that lead them to reach more effective cycling stabilities. The EDLC is typically operated with stable performance of charge or discharge, and even more than 10^6 cycles. In contrast, electrochemical battery restricted with constrain up to as many as only around 10^3 cycles. The EDLC is suitable to serve for employments and applications that do not require user in the harsh service-able environments because of this cycling stability, for example, in the deep sea or high mountains [4, 15].

Because the EDLC is able to utilize either an organic or an aqueous electrolyte, then the performance of the EDLCs are modified by customizing the manner of electrolyte solution itself. Generally, the aqueous electrolytes, i.e., KOH and H_2SO_4, have lower ESR and also smaller minimum requirements for pore size, on the other hand, compared to the organic electrolytes, for example acetonitrile (CH_3CN). Aqueous electrolytes generally possess with poor breakdown voltages. Thus, for the consideration between an organic or aqueous electrolyte, the trade-offs of capacitance, voltage, and ESR must also be taken into account [4, 15, 222]. Due to the above reasons for these trade-offs, the intended particular applications of the supercapacitor will predictably be the final judge to pick the appropriate electrolyte solution.

While the type of the electrolyte play important role in the supercapacitor mean, the subordinate classes of EDLC is primarily differentiated by the carbon-based materials used as electrodes. Carbon-based electrode materials typically possess larger surface area, cheap productions, and well fabrication than kinds of electrodes, i.e., conducting polymers or metal oxides [4, 15, 222]. Different types of carbon-based materials that considered to be used as preference for storing charges in the electrodes in EDLCs, such as activated carbons, carbon aerogels, and carbon nanotubes will be accordingly mentioned.

(a) **Activated Carbons**

This type of carbon is the mostly used material as electrodes in EDLCs because it is not only lower cost compared to other forms of carbon but also possesses larger surface area among carbon-based electrodes. It has generally utilized the complex of porous structure that consist of different microporous size which is less than 20 Å wide, mesopores within the range of 20-500 Å wide, and macropores which larger than 500 Å wide, accordingly, in order to attain as larger surface areas as possible. Even though capacitance proportionally depends to its surface area as demonstrated previously in equation B.2, experiential evidence advocated that in the case of activated carbons, not all surface areas are truly contributed to the capacitance of the device [222–225]. This disagreement is determined that causing by the size of electrolyte ions that larger than the pore sizes and cannot diffuse into smaller micropores. As a result, they are blocking porous reside for contributions of collecting charges [225–227].

The relationship between the distribution of pore sizes, the power and the energy density of capacitors are observed that smaller pore sizes related with greater energies and bigger pore sizes related with also greater power. According to this factor, the pore size distribution of activated carbon electrodes can also be another major research in the EDLC development, especially, focusing on determining for the optimal porous sizes to aim for specific sizes of target ions in electrolyte and also on regaining the methods deployed to customize the porous size during production processes [222, 223, 225–227].

(b) **Carbon Aerogels**

Carbon aerogel is also considered to be a potential candidate as one of the electrode materials for the EDLC family. Carbon aerogel is produced from the conductive carbon with the interspersed mesopore nanoparticles. Because of its uninterrupted structure and stability of chemical bond to the current collectors, this type of carbon does not need any additional adhesive-binding agents to electrodes. As being the binderless electrodes, carbon aerogel has effectively been exhibited to offer a lower ESR than any other forms of activated carbons [222, 228]. Because of this reduction in ESR, it leads to achieve higher power, referred to equation B.4 in previous section.

(c) **Carbon Nanotubes**

For EDLCs, different kinds of single-walled nanotubes (SWNTs) and multi-walled nanotubes (MWNTs) materials are regarded as active electrodes for the energy storage. According to the tendency of several former researches [222, 229–233], it has suggested that there has been a great amount of attention in an increasing usage of these types of carbon nanotubes (CNTs) in EDLCs. The electrodes that fabricated from CNTs are typically produced as binding material in continuous network of mesoporosity. Because of the extraordinary mesoporosity, they do possess a great ability in charge accumulation between interfaces of electrolyte and electrode. Furthermore, MWNTs do greatly supply capacitance values much larger than SWNTs.
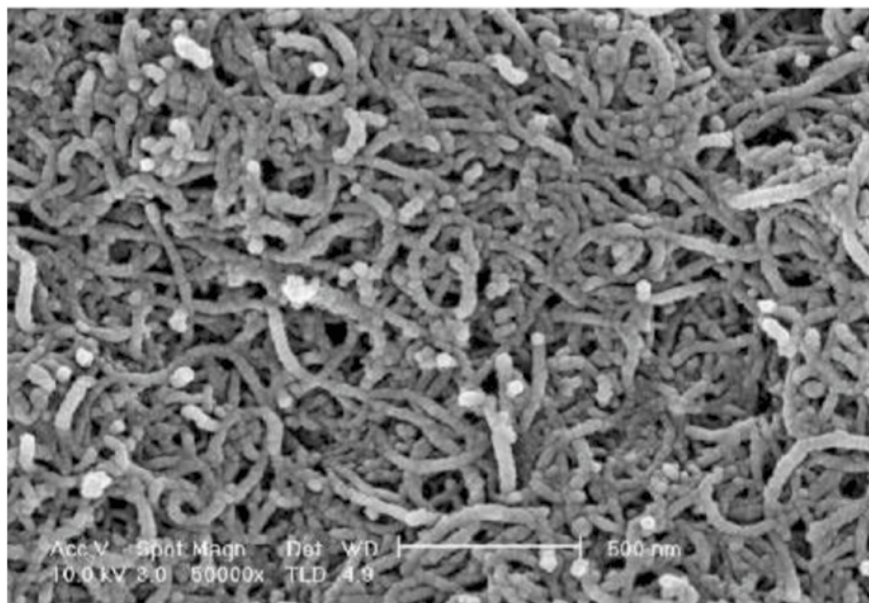
Figure B.5: Scanning electron microscope (SEM) image of carbon nanotubes (CNTs), reprinted from [5].

The unique structure of CNTs is illustrated in Figure B.5. The mesopores in the CNT-based electrodes are interconnected, unlike any other carbon-based electrodes, which let the charge distribution continuously. And that uses almost all of the available surface areas efficiently. As a result, the overall surface areas have been utilized more effectively to achieve higher magnitude values of capacitances in comparison with those of activated carbon-based electrodes, CNT-based electrodes do possess the less surface areas in comparison to other kinds in its family [222, 234].

In addition, CNT electrodes possess the ESR resistance lower than other activated carbon because the electrolyte ions can be diffused more easier into the mesoporous network [232, 235, 236]. Furthermore, there are several techniques for CNT fabrication that developed in order to further decreases the ESR magnitudes. CNTs can directly be produced into the current collectors with subjected to high temperature treatment, or even colloidal-suspension thin films [230, 235–237]. The CNTs structure efficiently leads to an improvement of energy densities comparable to other carbon-based materials. Because of the reduction of ESR, it is able to reach better power density, referring to equation B.4.

2. **Pseudocapacitors**

Pseudocapacitors faradiacally store and transfer their charges between electrolyte and electrodes while the EDLC supercapacitors store charge electrostatically which can be accomplished through intercalation processes reduction-oxidation reactions, and electrosorption [238, 239]. These would be advantages of faradaic processes that may lead pseudocapacitors to reach much higher energy densities and capacitances than those of EDLCs [240–242]. In pseudocapacitors, there are typically 2 electrode materials that

generally deployed to store charges. They are conductive polymers and metal oxides.

(a) **Conductive Polymers** are a type of pseudo-capacitive materials that the bulk of the material withstands the rapid reduction-oxidation reaction to present the capacitive response. They have exhibited larger energies in comparison to other EDLCs [243]. In addition to relatively high capacitance and conductivity, Conductive polymers have relatively both lower ESR and also cheap-price production in comparison to other of its own family materials [223]. For the n- and p-type configuration in particular, a negative charge, n-doped, and a positive charge, p-doped, conductive polymer electrodes possess the highest power densities and potential energy.

In contrast, conductive polymers are generally more conductive than the inorganic materials. They, therefore, possess higher power capability. They do have disadvantage that they have less efficient n-doped conductive polymers. They have limited these pseudo-capacitive materials to achieve their true potentials [241, 244]. In addition, it is also considerable that the stability of these pseudocapacitors through large amount of charge and discharge cycles are possibly limited by their physical mechanism of conducting polymers in the reduction-oxidation reactions [4, 223, 245]. In other words, they reside and reduce substantially during charge/discharge processes, respectively. Then, their life cycles would be inferior to EDLCs which only charging through the desorption-adsorption of ions. This issue has created difficulties in the development of conductive polymer pseudocapacitors.

Among the conductive polymers, there are several materials that are worth to mention in this review, and they are polyaniline, polypyrrole, and poly(3,4- ethylene-dioxythiophene) (PEDOT).

i. **Polyaniline** (PANI) has been widely studied as an electrode material in battery or supercapacitor applications [242, 246, 247]. The desirable properties of PANI have many benefits to supercapacitor devices, such as high electroactivity, high doping level, and its outstanding stability. It possesses the most variable specific capacitance of all other conductive polymers. The specific capacitance is achievably within the range from 400 to 500 F g^{-1} in an acidic medium [248]. One of the main disadvantage of polyaniline, it has required proton to charge and discharge. Thus for the protic solvent, acidic solution, or a ionic liquid should be presented [243].

ii. **Polypyrrole** (PPy) provides many aspects for its flexibility schemed in electrochemical processes than the rest of conducting polymers [249]. It has agreeably been the main topic research as electrode in supercapacitors or batteries [250]. On the downside, polypyrrole cannot be an n-doped material. It was found that to be used as a cathode one. Because of its high density, PPys have capacitance as high as around 400 to 500 F cm^{-3}). The disadvantage of the dense growth is found that would lead to the restricted access to the poorer sites for doped ions. Due to this reason, it decreases the capacitance values per unit mass, specifi-

cally, for the case the bulk of coatings process [251].

iii. **Poly(3,4-ethylenedioxythiophene)** (PEDOT) are commonly known to have a mass specific capacitance, around 210 F g^{-1} [251], relatively lower than other conductive polymers, for example, polypyrrole possesses around 620 F g^{-1}, and while PANI is about 750 F g^{-1} [252]. However, PEDOT can be potentially and statically grown into the thicker films, up to 0.5 mm [251], were porous nanoparticles. These bulky PEDOT films have led them to exhibit the electrode specific capacitance C_E, in F cm^{-2}, growing linearly with the film deposited charge which astonishingly higher than formerly reported for PPy and even PANI, electrode specific capacitance. Even though they are known to possess a few degrees higher in mass specific capacitance, in F g^{-1} [251].

(b) **Metal Oxides**

Metal oxides have previously been studied as the possible electrodes for pseudo-capacitors because of their high conductivities [4, 15, 240, 253, 254]. The majority of relevant researches have been focusing on ruthenium oxide. This is due to the main reason that other metal oxides have not obtained the comparable capacitances. Typically, the capacitance of ruthenium oxide (RuO$_2$) is gained through either the intercalation, or insertion and removed protons to amorphous structure. The capacitance not only exceeds that of carbon-based but also that of conductive polymer materials in hydrous form of ruthenium oxide [253, 254]. Furthermore, the hydrous RuO$_2$ has ESR lower than other electrodes; therefore, this would allow pseudocapacitors with ruthenium oxide to achieve both higher in power and energy densities than other conductive-polymer pseudocapacitors or other EDLCs. Unfortunately, RuO$_2$ is limited to be a useful material by the excessive cost. Therefore, the next challenge of research in this area is to find progressive methods in fabrication processes and possibly composites to keep the cost of RuO$_2$ lower than present day, but without losing the high performance of pseudocapacitors [4, 15, 240].

3. **Hybrid Capacitors**

The research of hybrid capacitors has been attempted to both take the advantages and also moderate the disadvantages of the pseudocapacitors and EDLCs to comprehend the improved performance of their characteristics and mechanisms. By governing faradaic and non-faradaic processes for charge storages, hybrid supercapacitors may have gone far greater than EDLCs in aspects of achieving higher power and energy densities without losing former benefits as mentioned before. Those are known to barricade the success of pseudocapacitors. The research and development in this area has concentrated on two different classes of hybrid supercapacitors. They are classified by configurations of their electrodes: composite and asymmetric.

(a) **Composite Materials**

Supercapacitor electrodes that utilized conductive polymers or metal oxide materials are designed to connect available carbon-based supercapacitors to construct

rapid charge devices of specific energy [243]. By fabricating the composite materials for electrodes may have take advantages of integrating carbon-based one with either conductive polymer, or metal oxide materials. It has incorporated both physical and chemical charging storage combined into one electrode. The carbon-based one will be employed to uphold a capacitive double-layer of charges. It offers larger surface areas while increasing the contact surface between electrolyte and the deposited pseudo-capacitance. Thus, with throughout faradaic reactions, pseudocapacitive materials would be able to undergo and then increase the capacitance of composite electrodes [245, 255].

Composite electrodes can be constructed from CNTs and conducting polypyrrole (PPy), or the other conductive polymers have been particularly successful process. Former experiments in previous synthesizing research have demonstrated that these electrodes are able to accomplish the capacitances that higher than the stand alone of only CNTs or PPys polymer-based electrode [239, 245, 255, 256]. For example, in 2001, Frackowiak et $al.$ found that the value of capacitance obtained from CNTs modified by PPy can reach 172 F/g, that is about twice value that given either by pure CNTs (80 F g^{-1}), or by pure PPy (90 F g^{-1}) [256]. The typical TEM image of resulting CNTs-PPy is shown in Fig. B.6. The surface area of CNTs was observed to be uniformly coated with PPy [6]. This is accounted for the structure of entangled CNTs uniformly approves the coating process of PPy and charge distribution. In addition, the structure has been demonstrated to set the boundary of the mechanical stress that resulting in the removing or inserting ions from PPy deposition. These composite materials would be able to reach the stable cycles in comparison to EDLCs unlike former conductive polymers [245, 255].

As listed in Table B.1, the PPy and PANI composites with CNTs in aqueous solutions have shown great values in specific capacitance ranged from 200 to 700 F g^{-1}. They have expectedly proven as the potential candidate for applications in supercapacitor electrodes.

Table B.1: The experimental measurement of polymer and carbon composites by chemical polymerization, where C_m is the mass specific capacitance, and C_E is the electrode specific capacitance.

Electrode	Electrolyte	C_m (F/g)	C_E (F/cm^2)	Reference Electrode	Reference
PPy/MWNTs (20 wt%)	1 M H$_2$SO$_4$	506	3.09	Hg/Hg$_2$SO$_4$	[257]
PANI/MWNTs (20 wt%)	1 M H$_2$SO$_4$	670	2.30	Hg/Hg$_2$SO$_4$	[257]
PPy/MWNTs	1 M H$_2$SO$_4$	172		Hg/Hg$_2$SO$_4$	[256]

(b) **Asymmetric Hybrids**
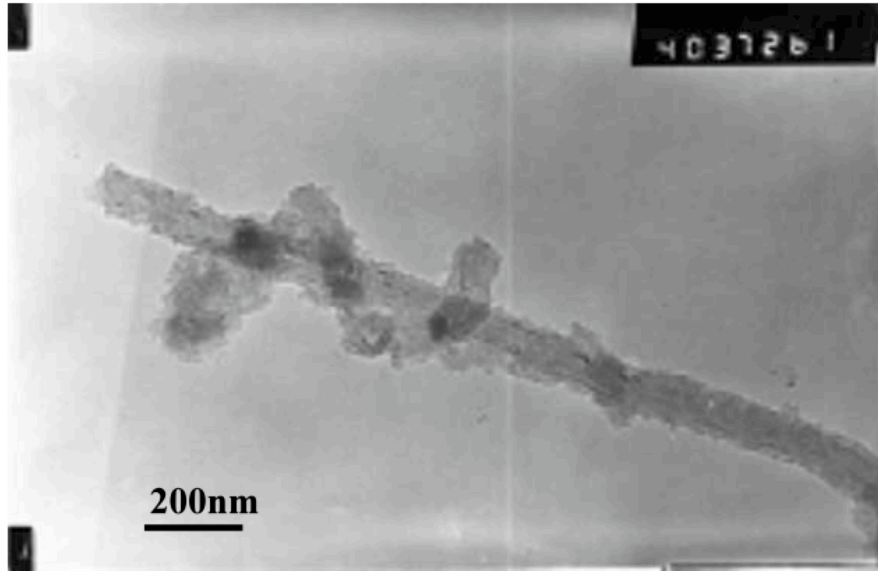
Figure B.6: Transmission electron microscopy (TEM) images of CNTs coated with polypyrrole, re-printed from [6].

Asymmetric hybrids capacitors have proposed the combination of the faradaic and non-faradaic methods by coupling pseudocapacitor electrodes with EDLC ones. The coupling of positive conductive polymer with negative activated carbon, in particular, has gained greatly attention in this research field conducting by many groups [223, 258, 259]. However, due to the restriction of efficient conductive polymers have not been able to reach the success of conductive polymer pseudocapacitors. By relying on the approach of implemented negative charge, the activated carbon gained possibility to overcome such obstruction. While conductive polymer electrodes generally not only possess with more magnitudes of capacitances and less internal impedance than activated carbon electrodes, but also have less cycling stabilities and lower maximum voltages. Because of coupling these two electrodes, asymmetric hybrid capacitors achieve both more energies and power densities than the comparative EDLCs. They additionally possess more stable cycles than the pseudocapacitors [223, 258, 259].

Hybrid supercapacitors have exhibited the recombination of improved characteristics in performances and mechanisms originally could not be attained. They have been attempted to combine the integrated features of both pseudocapacitors and EDLCs all together into one unified supercapacitor. Even though hybrid capacitors have previously been studied less than pseudocapacitors or EDLCs, the available researches have proposed that they might possibly be able to outperform comparable pseudocapacitors and EDLCs [223, 229, 241]. As a result, many researches make the efforts to fabricate the better hybrid supercapacitors, and the development of models with more accuracy. These area have been continued to expand intensively [255, 258–265]. Besides the increasing interests of development in higher life cycles and also higher energy supercapacitors, adapting their flexible models and their performance are hopefully to overcome those of EDLCs as the highly potential

74

class in the near future.

Appendix C

Graphene and Hybridizations of Carbon

Carbon is the number 6th element in the periodic table. Therefore, its atom consists of 6 protons, 6 electrons, and x neutrons, where x can possibly be 6, 7, or 8. For the stable isotopes ^{12}C and ^{13}C, x is 6 and 7, respectively, and when x is 8, it characterizes the radioactive isotope ^{14}C. With a nuclear spin $I = 0$, the isotope of ^{12}C is existing the most common one. There are around 99% of all carbon atoms existing in the nature, whereas only about 1% is ^{13}C with the nuclear spin $I = \frac{1}{2}$. There are traces of ^{14}C, which is approximately 10^{-12} of carbons, whereas the β decay into nitrogen ^{14}N. Even though ^{14}C rarely occurs in the nature, but it is an essential carbon isotope that used for identifying ages of historical subjects as a radioactive carbon. The ^{14}C has its half-life approximately 5,700 years, and for instance, the ^{14}C determined concentration of an organic substances, i.e., especially tree. Then, researchers can roughly measure the date of biological ages up to maximum 8×10^4 years. As one has already known that carbon is generally the fundamental element for every organic molecules. Thus, it is basically regarded as most element in all lives on Earth.

The 6 electrons are in the configuration of $1s^2 2s^2 2p^2$ in the atomic ground state, such that 2 electrons will first fill the inner shell $1s$, which is the closest to the nucleus. It will interact with any chemical reactions. Then, its other four electrons are occupied in the the shell of $2s$ and $2p$ orbitals, respectively. In the $2p$ orbitals, with $2p_x$, $2p_y$, and $2p_z$, they are around 4 eV higher than the adjacent $2s$ orbital. The leftover two electrons are energetically placed into the $2s$ orbital, and then other two of them are left in the $2p$ orbitals, referrong Fig C.1. However, it turns out that, in order to form covalent bonds with the presence of other elements, it is required to excite an electron in the $2s$ orbital to the 3rd of $2p$ orbital, The output energy of covalent bond is actually greater than 4 eV, and that was originally input in excited state.
As a result, 4 quantum states, $|2s\rangle$, $|2p_x\rangle$, $\left|2p_y\right\rangle$, and $|2p_z\rangle$, are equivalent in the electronic excited state, A superposition of the state $|2s\rangle$ with $n \left|2p_j\right\rangle$ states is called sp^n hybridization. In covalent carbon bonds, it will play a very important role.

C.1   sp^1 Hybridization

For the sp^1 hybridization, the $|2s\rangle$ state is possessing with one of the $2p$ orbitals. If the $|2p_x\rangle$ state is chosen for a demonstration, the state possesses equally the same from original states acquired by symmetric and anti-symmetric as
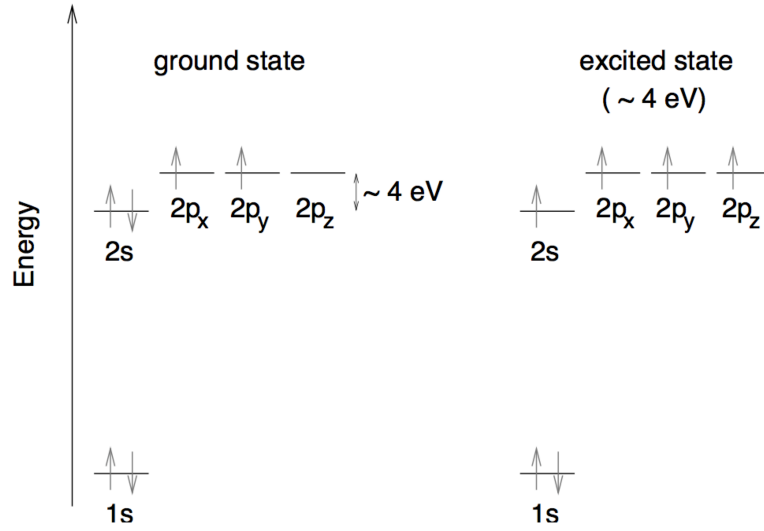
Figure C.1: Left: electronic configurations for carbon in the ground state. Right: in the excited state.

$$|sp_+\rangle = \frac{1}{\sqrt{2}}(|2s\rangle + |2p_x\rangle), \tag{C.1}$$

$$|sp_-\rangle = \frac{1}{\sqrt{2}}(|2s\rangle - |2p_x\rangle) \tag{C.2}$$

While the other states, sucha as $|2p_y\rangle$ and $|2p_z\rangle$, will be left out by the occurance of this superposition. In this case, the electronic density of the hybridization orbitals would be stretched along direction of the $+x$ or $-x$ axis for the $|sp_+\rangle$ or $|sp_-\rangle$ states, respectively. It has the form of a club as shown in Figure C.2(a)]. This hybridization plays an essential role in the formation of; for example, the acetylene with H-C≡C-H bonding in which the intersection of sp^1 orbitals as 2 carbons forming covalent σ bond as depicted in Figure C.2(b). While $2p$ orbitals are left and unhybridized, they would, furthermore, be additionally related to π bonds whereas they are noticeably not as strong as the σ bond formation.

C.2 sp^2 Hybridization

For the $2s$ and two $2p$ orbitals, the $|2p_x\rangle$ and the $|2p_y\rangle$ states may be chosen, the planar sp^2 hybridization is obtained. The three quantum-mechanical states can be specified as

$$\left|sp_1^2\right\rangle = \frac{1}{\sqrt{3}}|2s\rangle - \sqrt{\frac{2}{3}}|2p_y\rangle, \tag{C.3}$$

$$\left|sp_2^2\right\rangle = \frac{1}{\sqrt{3}}|2s\rangle + \sqrt{\frac{2}{3}}\left(\frac{\sqrt{3}}{2}|2p_x\rangle + \frac{1}{2}|2p_y\rangle\right), \tag{C.4}$$

77
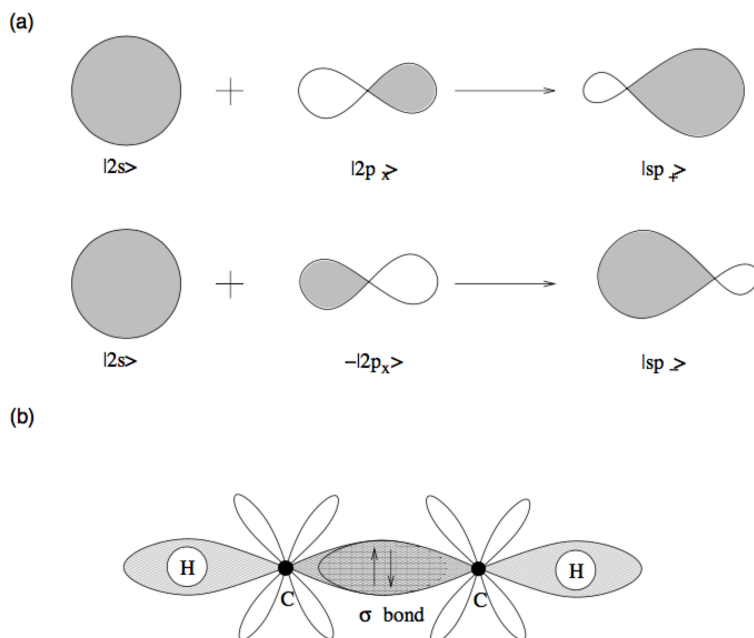
Figure C.2: (a) Schematic of the sp^1 hybridization. Right: the electronic density of $|2s\rangle$ and $|2p_x\rangle$ orbitals. Left: hybridized ones. (b) Example of acetylene molecule (H-C≡C-H). The propeller shape of $2p_y$ and $2p_z$ orbitals consists of 2 C atoms.

$$\left|sp_3^2\right\rangle = -\frac{1}{\sqrt{3}}|2s\rangle + \sqrt{\frac{2}{3}}\left(-\frac{\sqrt{3}}{2}|2p_x\rangle + \frac{1}{2}|2p_y\rangle\right). \tag{C.5}$$

The orbitals are relatively aligned in the xy-plane, and they have mutually formed the angles of 120° as illustrated in Figure C.3 (a). The remaining unhybridized electrons in $2p_z$ orbital would be perpendicular to the plane.

The molecular structure of benzene can also be used as a notable example for chemical hybridization. It consists of 6 atoms of carbon forming a hexagon structure, and all C atoms are bonded together by σ bonds as shown in Figure C.3 (b). Furthermore, each C atom has a covalent bond with H atoms individually which pointed from the hexagon structure. Besides the 6 σ bonds, the remaining electrons in the $2p_z$ orbitals form π bonds, and result in double bonds with just a single σ bonds surrounding all linked corners.

Due to the fact that a single σ bond is weaker than a double bond. A double bond of C would yield a distance of 1.35 Å, while a single σ bond is longer with length of 1.47 Å. In fact, the measured distance of C-C bond length in benzene is actually 1.42 Å for all bond types. It is approximately an average of single and double bond length. In 1931, Linus Pauling explained the equivalence of bonds in benzene within a quantum-mechanic manner of the benzene molecule [266]. The ground state of the benzene is actually treated as superposition of the 2 possible configurations varied by π bonds position. Thus, π electrons would be delocalized top and bottom of benzene structure as schematically depicted in Figure C.3 (c).

Under the chemical point of view, graphene sheet would still remained as the fundamental
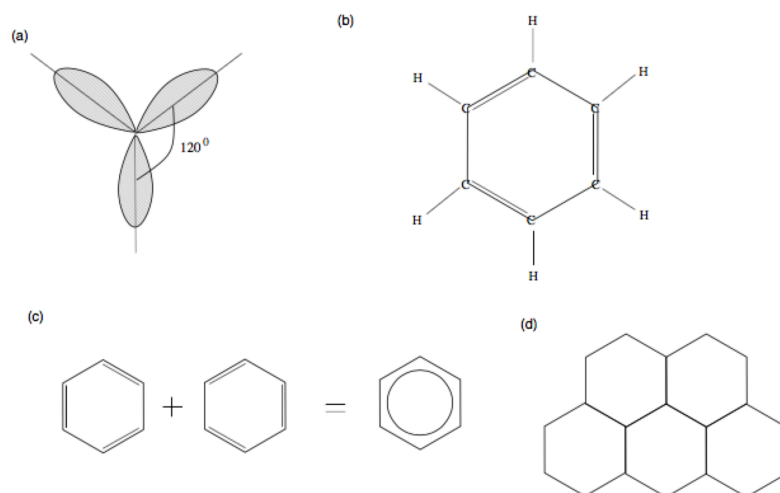
Figure C.3: (a) Schematic of sp^2 hybridization with orbitals formation of 120° angles. (b) Schematic of benzene molecule (C_6H_6). (c) The quantum-mechanical ground state of the benzene. (d) Graphene depicted as building blocks of benzene hexagons.

constituent in graphitic structures. It is the youngest allotrope from an experimental consideration, and only available to physical measurements since 2004, and simply considered as basic building tiles from benzene molecule, whereas C atoms take places of H atoms at the cornered edges of hexagons. The π electrons are delocalized over top and bottom of structure, shown in Figure C.3 (d).

The longest known allotrope is the 3D graphite structure as depicted in Figure 2.2. Historically in the 16th century, graphite was first discovered in a mine in England. In the early day, it was mainly used for graphical and marking purposes; for instance, the farmers nearby the graphite mine used it for marking sheep. During a long time, graphite was mistakenly considered as another particular type of lead because of its dark color and softness. As a result, named lead pencil has been the evidence of this historical error, and even now the center core of the pencil has still been called pencil lead.

As a perspective point of view, graphite may be seen as the stack of many graphene sheets, see Figure 2.2. Each graphene sheet is mounted together though the van der Waals interaction, which considerably weaker than inplane covalent bonds. This physical property of graphite can obviously be perceived when a piece of graphite in the pencil scratched over the surface sufficiently, i.e., on paper. The couple stacks of graphene layers are gradually exfoliated from graphite and left on the paper. It is mostly because of the van der Waals interaction between the graphene layers.

The other discovery of carbon allotrope or fullerenes, i.e., In 1985, Curl, Kroto, and Smalle have been discovered the 0D graphitic allotrope [267]. It is a buckyball, the form of a football structure, the most prominent representative of the C_{60} molecule. It also consists of graphene sheet as the basic constituent. However, instead of hexagon structure, some are replaced by pentagons, which have caused crumble layer and formed into a spheric structure, refer to Fig-

(a) 109.5° **(b)** 0.357nm
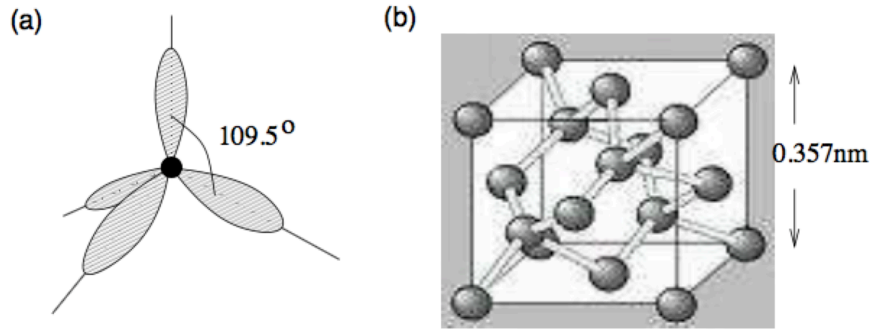
Figure C.4: (a) sp^3 hybridization with angles between the 4 orbitals are 109.5°. (b) Structure of crystallite diamond.

ure 2.2.

Then, the CNT is the 1D allotrope where graphene sheets are rolled up into its final formation with a diameter of several nm. SWNTs and MWNTs could be distinguished by the number of rolled up graphene sheets. The discovery of CNTs is often attributed to Iijima and referred to his Nature publication [268]. Even though it seems that CNTs had a history in the community of material science longer than that [269]. However, it is mostly due to Iijima's paper that attracted the interest of the scientific community to CNTs and initiated an intense research on this compound globally.

C.3 sp^3 Hybridization

If the $2s$ and 3 of $2p$ orbitals are superposed, the sp^3 hybridization is otained. It consists of four club-shaped orbitals formed a tetrahedron structure. The orbitals formation with angles of 109.5°, refer to Figure C.4 (a). Methane (CH_4) would certainly be a good example for sp^3 hybridization, where 4 hybridized orbitals are formed covalent bonds with the $1s$ hydrogen atoms. For the formation diamond, carbons in liquid state are condensed under very high pressure, and then $2p^3$ hybridization is formed. In Figure C.3 (b), The crystallite structure of diamond has two face-center-cubic (fcc) where the lattice spacing is 0.357 nm.

Although the 3D graphite and diamond crystals are physically extremely different, they consist of the same C atoms. Due to its layered structure, graphite is considerably a soft material, whereas diamond is the hardest material in the nature because of their covalent σ bonds in all bonds. In the outer atomic shell of diamond, their 4 valence electrons have all been used in σ bond formations. This is one of the reasons why diamond is a good insulator with the 5.47 eV band gap, which is a large value [270]. For the case of graphite systems, the π bonds are weaker than that σ bond of diamond. Thus, it yields an excellent conducting property than diamond.
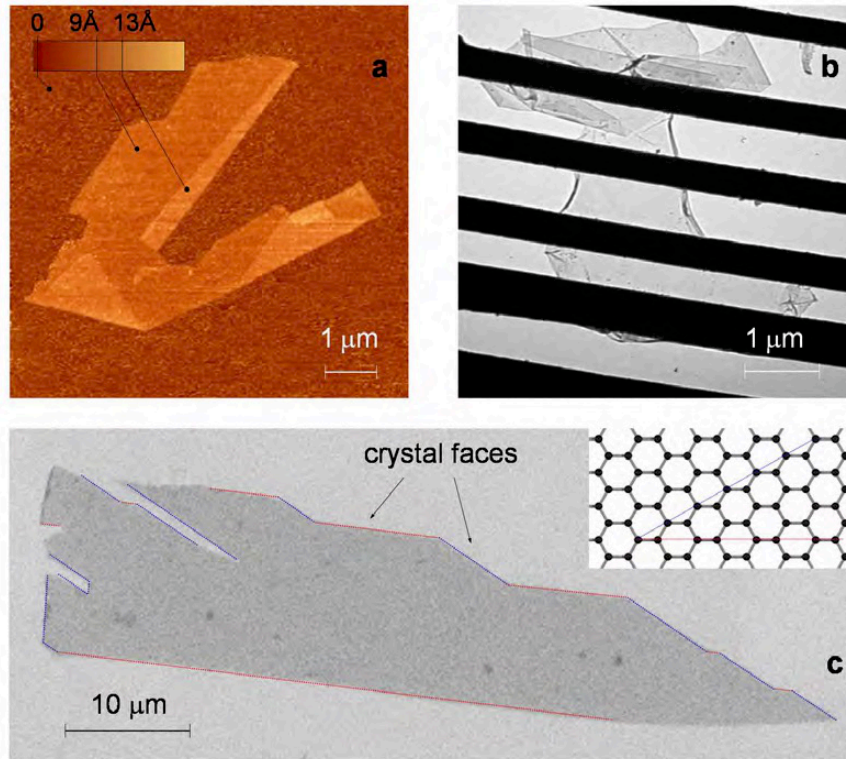
Figure C.5: (a) Atomic force microscopy (AFM) image of graphene [7]. (b) Transmission electron microscopy (TFM) image is adapted from [8]. (c) Scanning-electron micrograph of the crystal faces, most are zigzag and armchair edges.

C.4 Graphene

Actually, graphene had already been studied long before since 1947 by P. R. Wallace [271]. He has theoretically used graphene as an example in the textbook for the calculation in the field of the physics. He studied and predicted that its electronic structure and the linear dispersion relation. Almost 4 decades later in 1984, G. W. Semenoff [272] reported its similarity in the Dirac equation as during that time he named monatomic of graphite lattice.

Long before 2004, a graphene production with stable structure was considered that would be impractical. Therefore, it completely got full attention after A. K. Geim, K. S. Novoselov at the University of Manchester, and their colleagues from Institute for Microelectronics Technology, Russia, have successfully accomplished. They published what they have discovered in Science issued in 2004 [20]. In this work, they reported how they fabricating, extracting, identifying, and characterizing of graphene properties. An effective exfoliation was simply conducted by using the Scotch tape method to extract a few layers of graphene from graphite. Then, the obtained layers of graphene were transferred to silicon substrate. In addition, these research groups were successfully able to analyze a few layers of graphene flakes by using the optical method. An atomic force microscope (AFM) image of graphene is depicted in Figure C.5. A single layer of such graphene fragments sometimes was also obtained and identified.

The development in the research area of graphene has literally exploded since 2005. A large
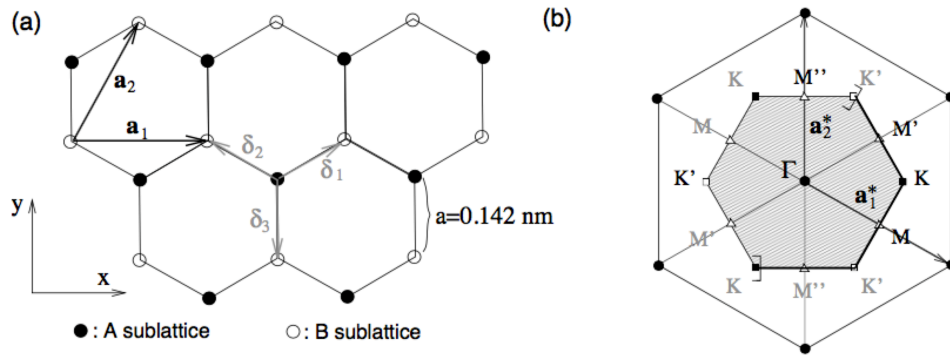
Figure C.6: (a) The honeycomb lattice of graphene formed by the carbon atoms. (b) Reciprocal lattice of the triangular lattice.
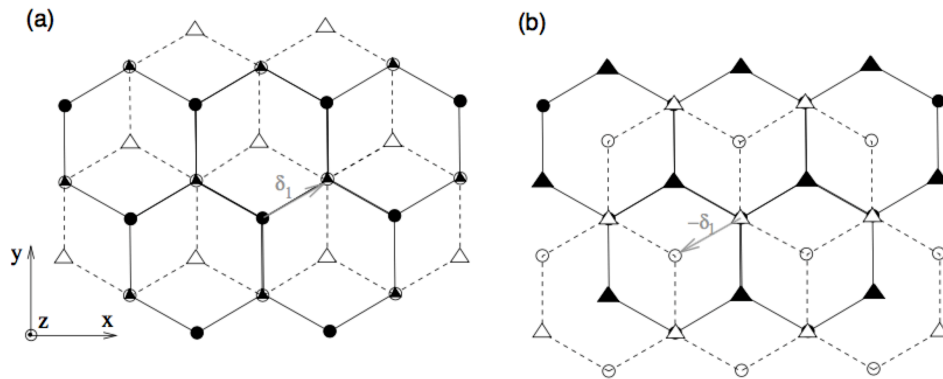
Figure C.7: Possibilities of bilayer graphene. Black symbols are lower and white ones are the upper layers. (a) The upper layer translated by δ_1 respect to the lower one. (b) The upper layer translated by $-\delta_1$ respect to the lower one

growing number of literatures related to graphene and its superlative properties have significantly been produced. The bilayers graphene has different properties in comparison to a single layer one has thoroughly been studied by many researchers [273–277]. From additional studies have shown that graphene is extremely stiffer than the strongest steel [278], and possesses many more superlative properties [279].

C.5 Structure of Graphene

1. **Honeycomb Lattice of Graphene**

   As it has already been presented briefly in the previous section that due to their sp^2 hybridization, the C atoms in graphene condense in a honeycomb-like structure. Two adjacent sites are not equivalently so honeycomb lattice structure is not a Bravais lattice as depicted in Figure C.6 (a). A triangular resides inside honeycomb lattice where a_1 and a_2 are basis vectors. The nearest neighboring sites on the sublattice A are in the north-east, the north-west, and the south corners, while the nearest neighborhoods on the sublattice B are in the south-east, the south-west, and the north. The vectors δ_1, δ_2, and δ_3 are con-

nected *nn* carbon atoms. The nearest neighboring C atoms are aparted by distance of $a = 1.42$ Å. The average length of the C-C and C=C σ bonds similar to benzene molecule.

The vectors δ_1, δ_2, and δ_3 are connected a site on sublattice A with *nn* on sublattice B are basically presented by

$$\delta_1 = \frac{a}{2}\left(\sqrt{3}e_x + e_y\right),\tag{C.6}$$

$$\delta_2 = \frac{a}{2}\left(-\sqrt{3}e_x + e_y\right),\tag{C.7}$$

$$\delta_3 = -ae_y,\tag{C.8}$$

and the triangular lattice spanned by vectors a_1 and a_2,

$$a_1 = \sqrt{3}ae_z\tag{C.9}$$

$$a_2 = \frac{\sqrt{3}a}{2}\left(e_x + \sqrt{3}e_y\right)\tag{C.10}$$

The modulus of vectors a_1 and a_2 produce the lattice space, where $\tilde{a} = \sqrt{3}a = 2.4$ Å. Area of a unit cell is given by $A_{uc} = \sqrt{3}\,\tilde{a}^2\,/2 = 0.51$ Å^2. Therefore, the density of carbon atoms is $n_C = 2/A_{uc} = 390$ Å$^{-2} = 3.9 \times 10^{15}$ cm^{-2}. There are more valence electrons than carbon atoms since there is only π electron per C atom that not actually related to the σ bond. Therefore, the density is principally $n_\pi = n_C = 3.9 \times 10^{15}$ cm^{-2}. As a result, this obtained density is not equal to the one in graphene that measured in electrical transport measurements.

The reciprocal lattice is defined with respect to the triangular Bravais lattice in Figure C.6 (b). The vectors are spanned as

$$a_1^* = \frac{2\pi}{\sqrt{3}a}\left(e_x - \frac{e_y}{\sqrt{3}}\right)\tag{C.11}$$

$$a_2^* = \frac{4\pi}{3a}e_y\tag{C.12}$$

Every site of a reciprocal lattice interchangeably presents equal wave vectors. Any wave that is vibrating, oscillating, or propagating waves on a mesh, the wave vector is differentiated by reciprocal lattice would actually have by same value by multiple of 2π phase that because the relationship is

$$a_i \cdot a_j^* = 2\pi\delta_{ij} \tag{C.13}$$

for i, j = 1, 2. Its original vector is a_1^* and a_2^*. The gray region in the center and border of the hexagon in Figure C.6 (b) denote the first Brillouin zone (BZ). The set of points is unequal in the reciprocal space of the point. Those that are not interconnected by reciprocal vectors or other different physical excitations. It center at Γ and the two sides are not equal at K and K' denoted in black and white, respectively. The excitations of long wavelengths will be in the vicinity of the first BZ central point. The thickest part of this region represented these scores as a definition in determining that no points are scored at the edges. Inequivalent points M, M', and M'' are depicted in white triangles. Furthermore, six corners possess the unequal points K and K', presented by the following carriers.

$$\pm K = \pm\frac{4\pi}{3\sqrt{3}a}e_x \tag{C.14}$$

In Figure C.6 (b), the four remaining corners depicted in gray may actually be connected to one of points with the aid of interpreting a reciprocal lattice vector. These points are very important to graphene in term of its electronic properties of graphene in the middle of points K and K' with low-energy excitations. The inequality of two corners is independent of the presence of sublattices A and B in the honeycomb.

2. **Stacking of Graphene**

Graphite is made by stacking multiple layers of graphene. The ordered graphite is typically distinguished by two different basic orders with a certain number of irregularities in stacked layer. The order of multi-layers can be illustrated in crystallite of graphite. First, bilayer graphene is considered. The interplane gap between these two layers is approximately $d = 3.4$ Å.

The order of stacking is that, in the upper layer, carbon atoms would be situated at the center of hexagon structure of the lower one. By doing so, the translation of layers are respected to each other. As demonstrated in Figure C.7, two different patterns are observably distinguished.

The displacement is described by σ_i or $-\sigma_i$, where any of the *nn* vectors, refer to equation C.10, with $i = 1, 2$, or 3 can be chosen. However, for the choice of σ_i, a configuration is obtained, as depicted in Figure C.7 (a) and (b). The two configurations are both containing the following A, B, A', and B' atoms per unit cell. They are equivalently when there is reflex in symmetry, $z \rightarrow -z$, perpendicular axis.

This difference in the stacking plays an essential role when considering crystal graphite with an infinite number of stacked layers, even though it is not related to the bilayer graphene. For situation that the next layer is translated with respect to the first one by δ_i, the 3rd layer would be translated with respect to the 2nd one by $-\delta_i$. And for its sites also concurrent with the 1st one by as same as δ_i, and that where the atomic configuration of the first one that has not been recovered. In general, two types of ordering can be distinguished by layers are translated with respect to the lower neighbor one by δ_i. An ABC stacking is obtained because three layers are needed to restore atomic configurations of the original one. Therefore, 6 atoms per unit cell possess the elongation of $3d$ toward the z-axis, or also called β-graphite.

During the stacking process of the graphene layers, the signs of the translation are alternated between positive and negative, for instance δ_i, $-\delta_i$, δ_i, $-\delta_i$, ..., a hexagonal stacking would be obtained mostly. There are 4 atoms per unit cell that possess $2d$ toward z-axis, called α-graphite. There principally are some random possibilities in graphene stacking, such as AB parts may randomly be substituted by ABC parts when considering α-graphite.

The turbostratic graphite is graphite in which there is quenched rotational misalignment between adjacent graphene sheets; for example, one sheet is rotated with respect to its neighbor. In this case, the translational disorder may be distinguished in rotated disorder in stacking. Graphene layers generally have a lesser amount of bound than crystal graphite. Because of this reason, the turbostratic graphite is a better lubricant.

For the rotational disorder case, bilayer graphene considered to rotate by an angle ϕ expressed as

$$\phi = \frac{a_1 \cdot a_1'}{|a_1||a_1'|} = e_x \cdot e_x' \tag{C.15}$$

where a_1' denotes lattice vector in upper layer of grpahene. It corresponds to a_1 in the lower layer. On condition that the angle satisfies the commensurable conditions, the Moire pattern would be achieved with bigger unit cell shown in Figure C.8 whereas the Moire pattern produces bigger honeycomb lattice.
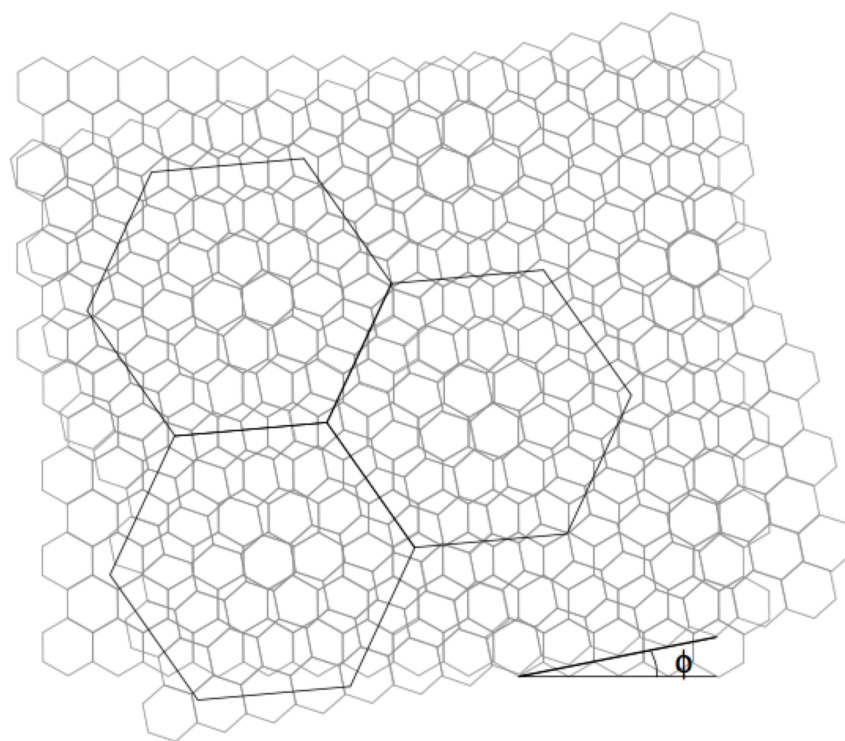
Figure C.8: Moire pattern obtained by stacking bilayer graphene with a relative angle of ϕ.

Appendix D

Density Functional Theory

There are several problems of computational properties for materials, but they can be carried out these by performing the calculation properties of the electrons in the material instead. However, in order to obtain the accurate results, electrons must be considered and taken into account that they are residing in the quantum world. Then, the next encountered problem will be to solve the famous Schrodinger equation. But such equation is, unfortunately, not able to be analytically solved, except for the case of one H atom.

In order to solve this particular equation, high performance computers are inevitably required. However, to get to the bottom line the many-particle problems, it is much complex too complex and too complicated calculation. With the system size eventually gets larger and larger, the calculation will terribly grow into more and more complex. Hence, solving such wave function with straightforward method is much difficult and trouble. It can only solve the few electrons in simple system. It will certainly cost excessive time and also massive resources. As a result for relevant materials problems, it seems quite impossible to perform the calculation. However, if other properties of the wave function are not required or needed to acquire, so by just investigating the electronic structure of particular system is adequate, then the full calculation of many-particle wave function is actually not needed to be performed. The electronic structure of the system is suggested to be comfortably treated by uncomplicated quantities. The electron densities in space just require a snapshot value of each point, neglecting the fact of how many particles involved. So in this way, the computation is much simpler to represent in comparison to the full many-body wavefunction.

From what has mainly been described above is a principle concept of density functional theory (DFT). It can express such many-particle problems by reformulating them into electron densities. DFT is principally based on the 2 famous theorems that firstly derived and proved by Hohenberg and Kohn in 1964 [154]. They state that it can express the energy of many-body systems as a functional of density. All system properties can be determined from the ground state one. Later, Levy [280] and Lieb [281] proposed a new way with generalization of the Hohenberg-Kohn theorem, and it is usually known as Levy-Lieb constrained-search formulation. An upholding theory is also usable for ground states degeneration.

In this section, in order to derive some formulas for energy density as a form of universal functional, they will be demonstrated by following the Levy-Lieb formulation since it is more clarifying and intuitive. The Coulomb interaction of the nucleus is already in DFT, except the

describing part of nucleus-nucleus interaction. It is more convenient to include it at the final expressions. However, the spin dependence in this brief derivation is dropped out just to help the expressions more clarified. A more information of spin dependent in DFT will be carried out later in the section D.4.

D.1   Universal Energy Functional

It is sufficiently required to understand Schrodinger equation, in order to describe the quantum system entirely. For a non-relativistic system, the many-particle Schrodinger equation is demonstrated as

$$\hat{H}\Psi = E\Psi \tag{D.1}$$

where $\hat{H}$ is the Hamiltonian operator and defined as

$$\hat{H} = \hat{T} + \hat{V}_{int} + V_{ext}(\vec{r}) \tag{D.2}$$

The above 3 terms on right-hand side are represented for kinetic energy ($\hat{T}$), potential energy due to the internal forces ($\hat{V}_{int}$), and the potential energy due to the external forces ($V_{ext}(\vec{r})$), respectively. Based on the quantum mechanics, the density is determined in term of the wave function as

$$n(r) = |\psi(\vec{r}_1, \vec{r}_2, \ldots, \vec{r}_N)|^2 \tag{D.3}$$

the total energy of the system in state Ψ is expressed as

$$E = \langle\Psi|\hat{H}|\Psi\rangle = \langle\Psi|\hat{T}|\Psi\rangle + \langle\Psi|\hat{V}_{int}|\Psi\rangle + \int d^3\vec{r}V_{ext}(\vec{r})n(\vec{r}) \tag{D.4}$$

In principle, the ground-state energy is also solved by minimizing the total energy equation with respect to all states $|\Psi\rangle$, for the case of minimization of the energy of states $|\Psi\rangle$ with density $n(r)$ equivalently. Within energy for density as a functional is at its lowest; for example, function of density in this particular case, as follows

$$E[n] = \min_{\psi\to n(r)}[\langle\Psi|\hat{T}|\Psi\rangle + \langle\Psi|\hat{V}_{int}|\Psi\rangle] + \int d^3\vec{r}V_{ext}(\vec{r})n(\vec{r})$$
$$\equiv F[n] + \int d^3\vec{r}V_{ext}(\vec{r})n(\vec{r}) \tag{D.5}$$

If the external potential V_{ext} and universal functional $F[n]$ are presented, the equation D.5 yields the energy for a specific density $n(\vec{r})$ at its minimum. In order to achieve ground-state energy of target system, the equation D.5 should also be minimized respect to densities $n(\vec{r})$ with all possibilities. $F[n]$ is a self-sufficient functional of external potential V_{ext}.

Next important issue would be how to actually find universal functional $F[n]$. This is a very hard question, and to acquire a right answer is also difficult. Because in order to find an actual expression $F[n]$, it is corresponding for solving many-particle in such Schrodinger equation. And on account of that, DFT would be staying in the mist if it was not the new approach of Kohn and Sham [155], which will be demonstrated in the next section §D.2.

D.2 Kohn-Sham Equation

D.2.1 Kohn-Sham Approach

Another preferable method was also proposed by Kohn and Sham in 1965 [155] to deal with puzzle of deriving an equation for $F[n]$, as mentioned in the Section §D.1. In the system, each electron obviously possesses its kinetic and Coulomb energies; however, due to the complications of many-body effects, it is quite difficult to derive the actual expressions for these quantities. On the account of the kinetic and Coulomb energies, they have to promote to internal energies. Then, $F[n]$ would harmonically unite these quantities in other manners or conditions.

In the quantum mechanical principle, it is quite difficult to understand how many-body effects, or exchange-correlation, would make an impact on such energies. Kohn and Sham had considered complications of many-body effects in interacting system which held in $F[n]$ visually perceive as few correction to total energy of auxiliary system with an absence of drawback in many-body effects. With approach proposed by Kohn and Sham, it can, therefore, take place the original with an identical system but less difficult. Simpler auxiliary system will not only possess identical number of electrons as same as the original, but also external potential.

Electrons individually possess their own kinetic energy for each single particle and that are independent from many-body effects. They have Coulomb repulsions from other electrons. Thus in auxiliary system, Hamiltonian $\hat{H}$ has to uphold Hartree energy, kinetic energy, and external potential terms. By deploying DFT, the expression is rewritten for ground-state energy as functional of density

$$E_{aux}[n] = T_s[n] + E_{\mathrm{H}}[n] + \int d^3\vec{r} V_{ext}(\vec{r}) n(\vec{r}) \tag{D.6}$$

The first and the second term on the right-hand side of equation D.6 can be calculated. The one-electron wave function ϕ_i of the auxiliary system can be derived as

$$\begin{aligned} T_s &= -\frac{1}{2} \sum_{i=1}^{N} \langle \phi_i | \nabla^2 | \phi_i \rangle \\ E_{\mathrm{H}} &= \frac{1}{2} \int d^3\vec{r} d^3\vec{r'} \frac{n(\vec{r}) n'(\vec{r})}{|\vec{r} - \vec{r'}|} \\ n(r) &= \sum_{i=1}^{N} |\phi_i'|^2 \end{aligned} \tag{D.7}$$

The Kohn-Sham approach to DFT based on assumption, within auxiliary system, it is assorted to possess the similar ground-state density to original system. In order to prove condition, the auxiliary system should be changed into the manners that present many-body effects. It will also be available in the real physical system. The new term should be expressed and show the differentiation between the original systems and the auxiliary ones. The DFT formalism is expressed as functional of density. To this additional term, Kohn and Sham have also given a name as the exchange-correlation functional $E_{xc}[n]$ which can express in terms of F as

$$F[n] = T_s[n] + E_{\mathrm{H}}[n] + E_{ext}[n] \tag{D.8}$$

The advantage about this, $E_{xc}[n]$ is now an universal realistically approximated such that by either quantum Monte Carlo (QMC) methods or many-body theories. On one condition that the last term $E_{xc}[n]$ on the right-hand side must have an exact expression. Then, the actual energy of original interacting system is actually calculated where total energy has finally transformed into

$$E[n] = T_s[n] + E_H[n] + \int d^3\vec{r} V_{ext}(\vec{r})n(\vec{r}) + E_{XC}[n] \tag{D.9}$$

where T_s is kinetic energy of independent particles, E_H is self-interacting energy of electron density, and E_{xc} is exchange-correlation energy. Before perform the calculations for any systems, first, in order to obtained single-particle wave functions ϕ_i required to create both kinetic energy and density.

For non-zero exchange-correlations, Hamiltonian of original auxiliary is not practicable for this case. However, before the single-particle wave functions can be obtained, $\hat{H}$ must be changed accordingly to the effect of exchange-correlation term. The method to acquire the $\hat{H}$ modification, it will be discussed more further in Section §D.2.2. Next is to find the expression of actual approximation for E_{xc}. There are many good approximations available which will also be discussed later in Section §D.3.

D.2.2 Kohn-Sham Equation

If the minimization with respect to density is performed, the Kohn-Sham equation will be obtained, but for exact derivation can be referred to a textbook by R. M. Martin, electronic structure: basic theory and practical methods [9]. The equation turns out proven to a similar case for auxiliary system. Because of the effects of the exchange-correlation, the potential possess the additional term as

$$h_{eff} |\phi_i\rangle = \left[-\frac{1}{2}\nabla^2 + v_H(\vec{r}) + v_{ext}(\vec{r}) + v_{XC}(\vec{r}) \right] |\phi_i\rangle = \epsilon_i |\phi_i\rangle \tag{D.10}$$

The solutions to the above equation are known as the Kohn-Sham orbitals ϕ_i for auxiliary system with correction approximation derived in exchange-correlation form.

The Kohn-Sham equations numerically derived in Section §D.2.2 are determined by iterating procedure namedly the self-consistent loop, and can be summarized in the flow chart as illustrated in Figure D.1. The procedure is in the following steps as follows:

1. The initial guess has to be made for electron density $n(r)$.

2. KS Hamiltonian based upon assumed density is constructed.

3. KS equations to acquire the KS orbitals are solved.

4. Construction of a new density from the KS orbitals.

5. The total energy of both the input-output densities by deploying the equation D.9. Now consider the following conditions that if energy differences are slightly and smaller threshold, then take final energy as ground-state energy. But, if tlarger than that, proceed to the next step.

6. Add the new density to the previous one to obtain new input density.

7. Then, proceed to the second step again.

In searching for the best method to combine the new and the old density for the last step significantly. Currently, several available methods are practical. Discussion in detail can directly refer to Chapter 9 of reference [9] for further information.

D.3 Exchange and Correlation

One of methods to solve the term is energy difference between full interacting system and simple auxiliary one. This also includes the exchange as well as correlated corrections. To derive an exact E_{xc} expression, it is not practical because it corresponds to solving the many-particle problem. However, it is feasible to presume it minimal, then, practicable approximation is sufficient. This is certainly the main reason that approximation was eventually developed. Most theoretical work within DFT focus to seek for improved approximation for E_{xc} within conditions of computational efficiency.

The local density approximation (LDA) was used in other former calculations at each point in reciprocal space, and it was an approximation per particle exchange and correlation energies by a homogenous electron gas plus the unchanged local density [44, 282]. Others [65, 210, 282, 283] deployed different aspects of generalized gradient approximations (GGA) by presenting density gradient corrections to the exchange and correlation energy. The Perdew-Burke-Ernzerhof (PBE) [157] exchange and correlation functional was adopted within GGA with fractions of the exact Hartree-Fock (HF) exchange, along with the combined fractions of exchange and correlated gradient correction.

D.3.1 Local Density Approximation

Kohn and Sham presented the first approximation for exchange-correlation energy in the same article [155], Kohn-Sham approach as discussed in previous section. The approximation is entitled by local density approximation (LDA), which is the simplest approximation to the exchange-correlation energy. It based on the assumption that exchange-correlation are not changed in homogeneous gas system. In LDA, the effects of exchange and correlation are local in manner, and the exchange correlation term is

$$E_{XC}^{LDA} = \int d\vec{r} n(\vec{r}) \epsilon_{XC}^{LDA}(n(\vec{r})) \tag{D.11}$$

where ϵ_{XC}^{LDA} is exchange-correlation energy of homogeneous gas with density n.

The LDA approximation has worked impressively and also yields exceptionally computational results for many atomic systems, such as in most of bulk metals, or even in less uniform systems, i.e. semiconductors, alloys, and ionic crystals. However, the main limits of the LDA is not taking into account the inhomogeneity in the density and non-local exchange-correlation

Self-consistent Kohn–Sham equations

Initial guess

$$n^{\uparrow}(\mathbf{r}), n^{\downarrow}(\mathbf{r})$$

Calculate effective potential

$$V_{\text{eff}}^{\sigma}(\mathbf{r}) = V_{\text{ext}}(\mathbf{r}) + V_{\text{Hartree}}[n] + V_{\text{xc}}^{\sigma}[n^{\uparrow}, n^{\downarrow}]$$

Solve KS equation

$$\left[-\frac{1}{2}\nabla^2 + V_{\text{eff}}^{\sigma}(\mathbf{r}) \right] \psi_i^{\sigma}(\mathbf{r}) = \varepsilon_i^{\sigma} \psi_i^{\sigma}(\mathbf{r})$$

Calculate electron density

$$n^{\sigma}(\mathbf{r}) = \sum_i f_i^{\sigma} \left| \psi_i^{\sigma}(\mathbf{r}) \right|^2$$

Self-consistent?

No

Yes

Output quantities

Energy, forces, stresses, eigenvalues, . . .
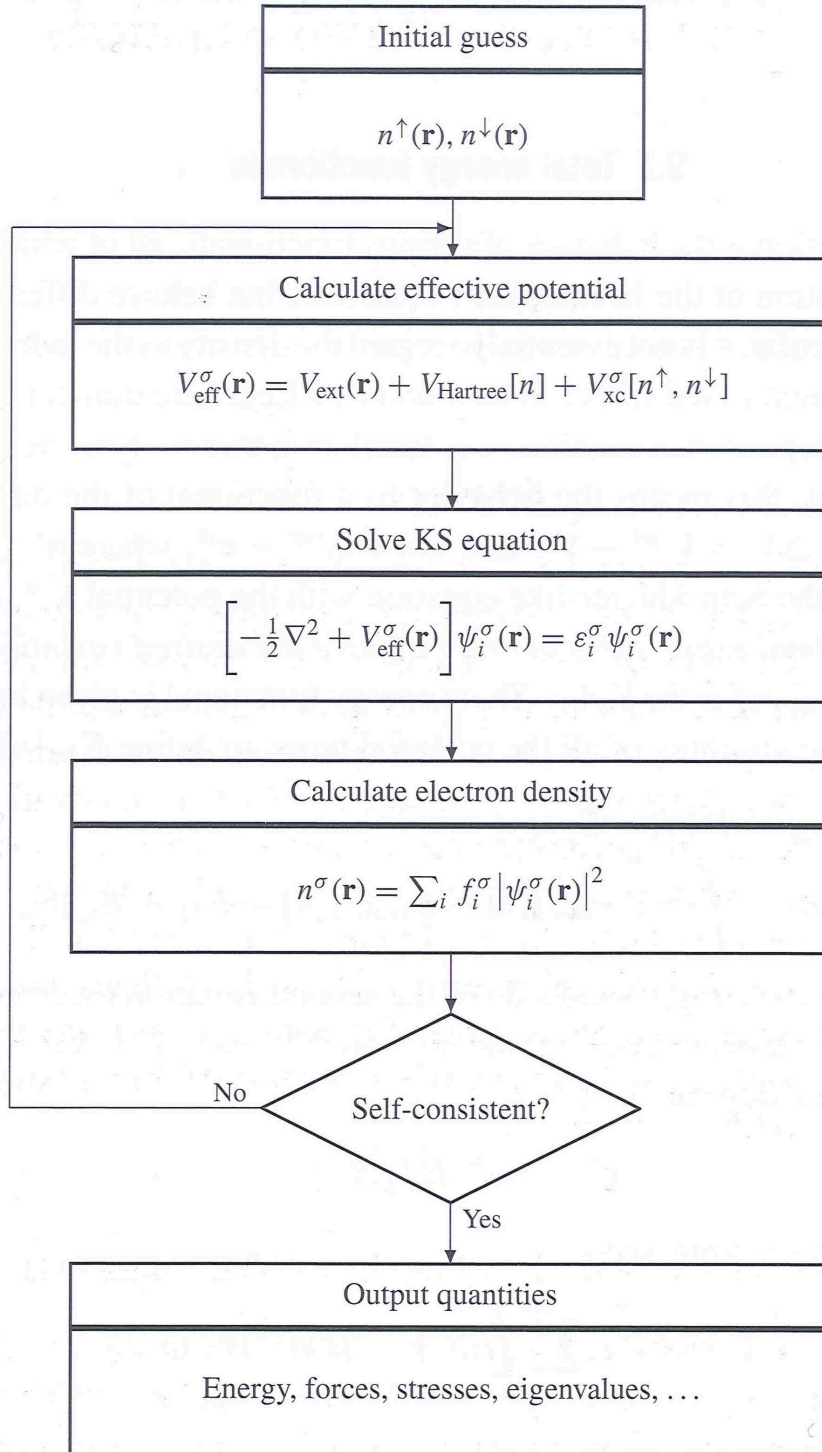
Figure D.1: Schematic of the self-consistent loop for solution of Kohn-Sham approach, adapted from reference [9].

effects. It has less accuracy for the systems in which the electronic density varies rapidly, such as in molecules and at surfaces. To address the issue of inhomogeneity in electronic density, an expansion of electron density in term of gradient of density similar to density at each point is used to improve the LDA will be discussed in the next subsection §D.3.2. For LDA and LSDA spin-dependence, refer to the textbooks, for example [9].

D.3.2 Generalized Gradient Approximations

After the accomplishment of the LDA, generalized gradient approximations (GGAs) has intimately proposed. Many approximations are functional of the density and the magnitude of the gradient of the density $|\nabla n|$. The general form of GGA functionals are expressed as

$$E_{XC}^{GGA} = \int d\vec{r} \epsilon_{XC}^{LDA} F(n, |\nabla n|, \dots)$$ (D.12)

where F is enhancement factor while various forms have been developed.

Normally, the GGA works very well for molecules, which improves over some of drawbacks of the LDA. The common used functional is composed of Becke [158], BLYP [159], Perdew-Wang 91 (PW91) [156], and its simplified version PBE [157]. In this thesis, the simplified PBE [157] is used for all self-consistent calculations. Additional discussion of GGA, referred to textbooks [9].

D.3.3 Hybrid Functionals

The hybrid density functionals describe a wide range of molecular systems more accurately. The basic idea is to incorporate amount of Hartree-Fock (HF) exchange with the exchange and correlation from LDA or GGA functional. In 1993, Becke proposed a semi-empirical exchange-correlation functional (B3P91) [284] with three parameters containing Hartree-Fock exchange, Becke exchange functional (B88) [158], and PW91 correlation [156], which are successful in describing many molecules.

$$E_{XC} = E_{XC}^{LSDA} + a_0(E_X^{HF} - E_X^{LSDA}) + a_X \Delta E_X^{B88} + a_C \Delta E_C^{PW91}$$ (D.13)

where the semiempirical coefficients are $a_0 = 0.20$, $a_X = 0.72$, $a_C = 0.81$.

They have been solved by data fitting of measured atomic energy. Alternatively, the B3LYP [158, 159] exchange-correlation functional uses the LYP correlation [159] instead of PW91 correlation [156], which is widely used in chemistry field.

Based on the arguments that exchange and correlation energy varies as a function of inter-electronic coupling, Perdew, Ernzerhof, and Burke [157] introduced the form as

$$E_{XC} = E_{XC}^{GGA} + \frac{1}{4}(E_X^{HF} - E_{XC}^{GGA})$$ (D.14)

They mixed 1/4 of Hartree-Fock exchange energy, and gave physical explanations.

Another hybrid DFT based on a screened Coulomb potential for exchange interaction was proposed by Heyd, Scuseria, and Ernzerhof (HSE) in 2003 [285].

$$E_{XC}^{SR,HFPBE0} = \frac{1}{4}E_X^{HF,SR} + \frac{3}{4}E_X^{PBE} + E_C^{PBE} \tag{D.15}$$

They used the screened short range (SR) HF exchange instead of the full HF exchange to construct this hybrid functional. Significant reduction in computational cost can be used in calculation for large molecules and clusters, in particular for systems with small band gaps, with reasonable accuracy.

D.3.4 van der Waals Functional

The other specific exchange-correlation energy E_{xc} that should be mentioned in this dissertation is the van der Waals density functional (vdW-DF) method. It is a non-local approximation for extending the limitation of other DFTs mentioned previously by taking the van der Waals (vdW) interactions into account.

This method was firstly proposed by Dion *et al.* with the strong benefit that vdW forces are treated in the similar manner as other kinds of interactions treated by conventional DFT methods [214]. The vdW-DF functional yielded considerable good results for layered-interaction structures [213].

In term of Kohn-Sham equation that outlined in Section §D.2.1, the vdW-DF functional has its total energy defined as

$$E^{vdW-DF}[n] = T_S[n] + E_{Hartree}[n] + \int d^3\vec{r} V_{ext}(\vec{r})n(\vec{r}) + E_{XC}^{vdW-DF}[n] \tag{D.16}$$

in which the standard Kohn-Sham equations are included with the kinetic energy (T_S) of the auxiliary system, the electrostatic energy ($E_{Hartree}$), and the interaction with an external potential (V_{ext}). In contrast to LDA or GGA, the correlation energy of vdW-DF also possesses with the non-local dependent term on the density. This non-local correlation is added to the exchange and correlation energy while using the correlation term of LDA and exchange term of GGA [214].

$$E_{XC}^{vdW-DF} = E_C^{LDA} + E_X^{GGA} + E_C^{non-local} \tag{D.17}$$

D.4 Spin Density Functional Theory

Up to this point, there is no discussion about characteristics of spin σ introducing in expressions that was interpreted previously in DFT yet. The electron density in ground state is considered as spin polarized, such as

$n(\vec{r}, \sigma = \uparrow) \neq n(\vec{r}, \sigma = \downarrow)$.

The occurrence of this manner is in the system that consists of a finite and odd number of electrons [9], In many systems, i.e. atoms with a finite and even number of electrons, keeping track of spin-polarization is not necessary. In general, the spin paired calculations is slightly

less time consuming. It generalize the DFT arguments to include particle density $n(r) = n(r, \uparrow)$ + $n(r, \downarrow)$ and spin density $s_\sigma(\vec{r}) = n(\vec{r}, \uparrow) - n(\vec{r}, \downarrow)$.

For total energy, the modified expressions depend on particle density and spin density [9].

Bibliography

[1] A. H. C. Neto, F. Guinea, N. M. R. Peres, K. S. Novoselov, and A. K. Geim, "The electronic properties of graphene," *Rev. Mod. Phys.*, vol. 81, pp. 109–162, Jan. 2009.

[2] K. Nakada and A. Ishii, "Migration of adatom adsorption on graphene using DFT calculation," *Solid State Commun.*, vol. 151, pp. 13–16, Jan. 2011.

[3] P. Gargiani, G. Rossi, R. Biagi, V. Corradini, M. Pedio, S. Fortuna, A. Calzolari, S. Fabris, J. C. Cezar, N. B. Brookes, and M. G. Betti, "Spin and orbital configuration of metal phthalocyanine chains assembled on the Au(110) surface," *Phys. Rev. B*, vol. 87, p. 165407(11), Apr. 2013.

[4] R. Kotz and M. Carlen, "Principles and applications of electrochemical capacitors," *Electrochim. Acta*, vol. 45, no. 15-16, pp. 2483–2498, 2000.

[5] I.-H. Kim, J.-H. Kim, and K.-B. Kim, "Electrochemical characterization of electrochemically prepared ruthenium oxide/carbon nanotube electrode for supercapacitor application," *Electrochem. Solid-State Lett.*, vol. 8, no. 7, pp. A369–A372, 2005.

[6] Q. Xiao and X. Zhou, "The study of multiwalled carbon nanotube deposited with conducting polymer for supercapacitor," *Electrochim. Acta*, vol. 48, pp. 575–580, Jan. 2003.

[7] K. S. Novoselov, D. Jiang, F. Schedin, T. J. Booth, V. V. Khotkevich, S. V. Morozov, and A. K. Geim, "Two-dimensional atomic crystals," *Proc. Natl Acad. Sci.*, vol. 102, pp. 10451–10453, Apr. 2005.

[8] J. C. Meyer, A. K. Geim, M. I. Katsnelson, K. S. Novoselov, T. J. Booth, and S. Roth, "The structure of suspended graphene sheets," *Nature*, vol. 446, pp. 60–63, May 2007.

[9] R. M. Martin, *Electronic structure: basic theory and practical methods*. Cambridge University Press, 2010.

[10] J. Janczak, R. Kubiak, M. Sledz, H. Borrmann, and Y. Grin, "Synthesis, structural investigations and magnetic properties of dipyridinated manganese phthalocyanine, MnPc(py)$_2$," *Polyhedron*, vol. 22, pp. 2689–2697, Aug. 2003.

[11] J. F. Kirner, W. Dow, and W. R. Scheidt, "Molecular stereochemistry of two intermediate-spin complexes. Iron(II) phthalocyanine and manganese(II) phthalocyanine," *Inorg. Chem.*, vol. 15, pp. 1685–1690, July 1976.

[12] G. A. Williams, B. N. Figgis, R. Mason, S. A. Mason, and P. E. Fielding, "Phthalocyaninato-cobalt(ii) (at 4.3°K, neutron study, β form) C$_{32}$H$_{16}$CoN$_8$," *J. Chem. Soc. Dalton Trans.*, pp. 1688–1692, 1980.

[13] J. M. Robertson and I. Woodward, "An x-ray study of the phthalocyanines: part III quantitative structure determination of nickel phthalocyanine," *J. Chem. Soc.*, pp. 219–230, 1937.

[14] C. J. Brown, "Crystal structure of β-copper phthalocyanine," *J. Chem. Soc. A*, pp. 2488–2493, 1968.

[15] A. Burke, "Ultracapacitors: why, how, and where is the technology," *J. Power Sources*, vol. 91, no. 1, pp. 37–50, 2000.

[16] A. Chu and P. Braatz, "Comparison of commercial supercapacitors and high-power lithium-ion batteries for power-assist applications in hybrid electric vehicles i. initial characterization," *J. Power Sources*, vol. 112, no. 1, pp. 236–246, 2002.

[17] Q. Ke and J. Wang, "Graphene-based materials for supercapacitor electrodes - a review," *J Materiomics*, vol. 2, pp. 37–54, Mar. 2016.

[18] C. Q. Sun, Y. Sun, Y. G. Nie, Y. Wang, J. S. Pan, G. Ouyang, L. K. Pan, and Z. Sun, "Coordination-resolved C-C bond length and the C 1s binding energy of carbon allotropes and the effective atomic coordination of the few-layer graphene," *J. Phys. Chem. C*, 2009.

[19] L. Pauling and L. O. Brockway, "Carbon-carbon bond distances. the electron diffraction investigation of ethane, propane, isobutane, neopentane, cyclopropane, cyclopentane, cyclohexane, allene, ethylene, isobutene, tetramethylethylene, mesitylene, and hexamethylbenzene. revised values of covalent radii," *J. Am. Chem. Soc.*, vol. 57, pp. 1223–1236, July 1937.

[20] K. S. Novoselov, A. K. Geim, S. V. Morozov, D. Jiang, Y. Zhang, S. V. Dubonos, I. V. Grigorieva, and A. A. Firsov, "Electric field effect in atomically thin carbon films," *Science*, vol. 306, pp. 666–669, Oct. 2004.

[21] K. S. Novoselov, A. K. Geim, S. V. Morozov, D. Jiang, M. I. Katsnelson, I. V. Grigorieva, S. V. Dubonos, and A. A. Firsov, "Two-dimensional gas of massless Dirac fermions in graphene," *Nature*, vol. 438, pp. 197–200, Nov. 2005.

[22] T. Ito and K. Shiraishi, "A theoretical investigation of migration potentials of ga adatoms near step edges on GaAs(001)-c(4×4) surface," *Jpn. J. Appl. Phys.*, vol. 35, pp. L1016–L1018, Aug. 1996.

[23] A. Braun and J. Tcherniac, "Uber die produkte der einwirkung von acetanhydrid auf phthalamid," *J. Ber. Dtsch. Chem. Ges.*, vol. 40, pp. 2709–2714, Mar. 1907.

[24] K.-Y. Law, "Organic photoconductive materials: Recent trends and developments," *Chem. Rev.*, vol. 93, pp. 449–486, Jan. 1993.

[25] S. A. Jenekhe and S. J. Yi, "Highly photoconductive nanocomposites of metallophthalocyanines and conjugated polymers," *Adv. Mater.*, vol. 12, pp. 1274–1278, Sept. 2000.

[26] J. M. Robertson, "An X-ray study of the phthalocyanines. part II. quantitative structure determination of the metal-free compound," *J. Chem. Soc.*, vol. 0, pp. 1195–1205, 1936.

[27] K. Sakamoto and E. Ohno-Okumura, "Syntheses and functional properties of phthalo-cyanines," *Materials*, vol. 2, pp. 1127–1179, Aug. 2009.

[28] K. Sakamoto and E. Ohno, "Synthesis of soluble metal phthalocyanine derivatives and their electron transfer prpperties," *J. Soc. Dyers Colour.*, vol. 112, pp. 368–374, Dec. 1996.

[29] K. Sakamoto and E. Ohno, "Synthesis and electron transfer property of phthalocyanine derivatives," *Prog. Org. Coat.*, vol. 31, pp. 139–145, May 1997.

[30] K. Lokesh, N. Uma, and B. Achar, "Synthesis and physico-chemical characterization of metal free, sodium and potassium phthalocyanine complexes," *J. Non-Cryst. Solids*, vol. 353, pp. 384–389, Mar. 2007.

[31] S. Senthilarasu, S. Velumani, R. Sathyamoorthy, A. Subbarayan, J. A. Ascencio, G. Can-izal, P. J. Sebastian, J. A. Chavez, and R. Perez, "Characterization of zinc phthalocyanine (ZnPc) for photovoltaic applications," *Appl. Phys. A*, vol. 77, pp. 383–389, Aug. 2003.

[32] S. Kera, H. Yamane, and N. Ueno, "First-principles measurements of charge mobility in organic semiconductors: Valence hole-vibration coupling in organic ultrathin films," *Progress in Surface Science*, vol. 84, pp. 135–154, May 2009.

[33] C.-L. Lin, C.-C. Lee, and K.-C. Ho, "Spectroelectrochemical studies of manganese phthalocyanine thin films for applications in electrochromic devices," *J. Electroanal. Chem.*, vol. 524-525, pp. 81–89, May 2002.

[34] S. R. Forrest, "Ultrathin organic films grown by organic molecular beam deposition and related techniques," *Chem. Rev.*, vol. 97, pp. 1793–1896, Oct. 1997.

[35] A. R. Gomez, C. M. Sanchez-Hernandez, I. Fleitman-Levin, J. Arenas-Alatorre, J. C. Alonso-Huitron, and M. E. S. Vergara, "Optical absorption and visible photolumines-cence from thin films of silicon phthalocyanine derivatives," *Materials*, vol. 7, pp. 6585–6603, Sept. 2014.

[36] O. A. Melville, B. H. Lessard, and T. P. Bender, "Phthalocyanine-based organic thin-film transistors: A review of recent advances," *ACS Appl. Mater. Interfaces*, vol. 7, pp. 13105–13118, May 2015.

[37] M. G. Walter, A. B. Rudine, and C. C. Wamser, "Porphyrins and phthalocyanines in solar photovoltaic cells," *J. Porphyrins Phthalocyanines*, vol. 14, pp. 759–792, Sept. 2010.

[38] Y. Tanaka, M. Ishikawa, N. Watanabe, Y. Takahashi, T. Naito, and T. Inabe, "Metal-lic one-dimensional conductors composed of axially ligated (phthalocyanato)Co^{III} with supramolecular cations of A(EtOH)$_4$ (A = Na and K)," *Crystals*, vol. 2, pp. 946–957, July 2012.

[39] E. Tosatti, M. Fabrizio, J. Tobik, and G. E. Santoro, "Strong correlations in elec-tron doped phthalocyanine conductors near half filling," *Phys. Rev. Lett.*, vol. 93, p. 117002(4), Sept. 2004.

[40] Y. Wang and D. Liang, "Solvent-stabilized photoconductive metal phthalocyanine nanoparticles: Preparation and application in single-layered photoreceptors," *Adv. Mater.*, vol. 22, pp. 1521–1525, Apr. 2010.

[41] M. Bouvet, "Phthalocyanine-based field-effect transistors as gas sensors," *Anal. Bioanal. Chem.*, vol. 384, pp. 366–373, Jan. 2006.

[42] I. Muzikante, V. Parra, R. Dobulans, E. Fonavs, J. Latvels, and M. Bouvet, "A novel gas sensor transducer based on phthalocyanine heterojunction devices," *Sensors*, vol. 7, pp. 2984–2996, Nov. 2007.

[43] P. Borker and A. V. Salker, "Synthesis, characterization and photocatalytic studies of some metal phthalocyanines," *Indian J. Chem. Technol.*, vol. 13, pp. 341–346, July 2006.

[44] Z. Shi and J. Zhang, "Density functional theory study of transitional metal macrocyclic complexes dioxygen-binding abilities and their catalytic activities toward oxygen reduction reaction," *J. Phys. Chem. C*, vol. 111, pp. 7084–7090, Apr. 2007.

[45] J. H. Zagal, S. Griveau, J. F. Silva, T. Nyokong, and F. Bedioui, "Metallophthalocyanine-based molecular materials as catalysts for electrochemical reactions," *Coord. Chem. Rev.*, vol. 254, pp. 2755–2791, Dec. 2010.

[46] N. Kobayashi, A. Muranaka, and K. Ishii, "Symmetry-lowering of the phthalocyanine chromophore by a C_2 type axial ligand," *Inorg. Chem.*, vol. 39, pp. 2256–2257, May 2000.

[47] R. P. Linstead and A. R. Lowe, "Phthalocyanines. part III. preliminary experiments on the preparation of phthalocyanines from phthalonitrile," *J. Chem. Soc.*, vol. 0, pp. 1022–1027, 1934.

[48] A. B. P. Lever, S. Licoccia, K. Magnell, P. C. Minor, and B. S. Ramaswamy, "Mapping of the energy levels of metallophthalocyanines via electronic spectroscopy electrochemistry and photochemistry," *Adv. Chem.*, vol. 201, pp. 237–252, June 1982.

[49] K. Sakamoto and E. Ohno, "Electrochemical characterization of soluble cobalt phthalocyanine derivatives," *Dye. Pigment.*, vol. 37, pp. 291–306, May 1998.

[50] G. Torre, P. Vazquez, F. Agullo-Lopez, and T. Torres, "Role of structural factors in the nonlinear optical properties of phthalocyanines and related compounds," *Chem. Rev.*, vol. 104, pp. 3723–3750, Aug. 2004.

[51] M.-S. Liao, J. D. Watts, and M.-J. Huang, "DFT study of unligated and ligated manganese^{II} porphyrins and phthalocyanines," *Inorg. Chem.*, vol. 44, pp. 1941–1949, Feb. 2005.

[52] P. A. Reynolds and B. N. Figgis, "Metal phthalocyanine ground states: covalence and ab initio calculation of spin and charge densities," *Inorg. Chem.*, vol. 30, pp. 2294–2300, May 1991.

[53] R. Kraus, M. Grobosch, and M. Knupfer, "Full electronic excitation spectrum of condensed manganese phthalocyanine," *Chem. Phys. Lett.*, vol. 469, pp. 121–124, Feb. 2009.

[54] D. W. Clack and J. R. Yandle, "Electronic spectra of the negative ions of some metal phthalocyanines," *Inorg. Chem.*, vol. 11, pp. 1738–1742, Aug. 1972.

[55] A. B. P. Lever, P. C. Minor, and J. P. Wilshire, "Electrochemistry of manganese phthalocyanine in nonaqueous media," *Inorg. Chem.*, vol. 20, pp. 2550–2553, Aug. 1981.

[56] P. C. Minor, M. Gouterman, and A. B. P. Lever, "Electronic spectra of phthalocyanine radical anions and cations," *Inorg. Chem.*, vol. 24, pp. 1894–1900, June 1985.

[57] N. Sehlotho, M. Durmus, V. Ahsen, and T. Nyokong, "The synthesis and electrochemical behaviour of water soluble manganese phthalocyanines: Anion radical versus Mn(I) species," *Inorg. Chem. Commun.*, vol. 11, pp. 479–483, May 2008.

[58] K. R. Rajesh and C. S. Menon, "Optical studies of manganese phthalocyanine thin films," *Mater. Lett.*, vol. 51, pp. 266–269, Nov. 2001.

[59] Z. Xu, J. Zhao, H. Li, K. Li, Z. Cao, and J. Lu, "Influence of the electronic configuration of the central metal ions on catalytic activity of metal phthalocyanines to Li/SOCl$_2$ battery," *J. Power Sources*, vol. 194, pp. 1081–1084, Dec. 2009.

[60] N. A. Bell, J. S. Brooks, S. D. Forder, J. K. Robinson, and S. C. Thorpe, "Backscatter Fe-57 mossbauer studies of iron(II) phthalocyanine," *Polyhedron*, vol. 21, pp. 115–118, Jan. 2002.

[61] M. Mahyari and A. Shaabani, "Graphene oxide-iron phthalocyanine catalyzed aerobic oxidation of alcohols," *Appl. Catal., A*, vol. 469, pp. 524–531, Jan. 2014.

[62] N. Safari and F. Bahadoran, "Cytochrome P-450 model reactions: a kinetic study of epoxidation of alkenes by iron phthalocyanine," *J. Mol. Catal. A: Chem.*, vol. 171, pp. 115–121, June 2001.

[63] N. Sehlotho and T. Nyokong, "Catalytic activity of iron and cobalt phthalocyanine complexes towards the oxidation of cyclohexene using *tert*-butylhydroperoxide and chloroperoxybenzoic acid," *J. Mol. Catal. A: Chem.*, vol. 209, pp. 51–57, Feb. 2004.

[64] Q. Zhou and R. D. Gould, "A study of the response rate to nitrogen dioxide exposure in metal phthalocyanine thin film sensors," *Thin Solid Films*, vol. 317, pp. 436–439, Apr. 1998.

[65] B. Bialek, I. G. Kim, and J. I. Lee, "First-principles study on the electronic structures of iron phthalocyanine monolayer," *Surf. Sci.*, vol. 526, pp. 367–374, Mar. 2003.

[66] N. Sato, H. Yoshida, and K. Tsutsumi, "Unoccupied electronic states in phthalocyanine thin films studied by inverse photoemission spectroscopy," *Synth. Met.*, vol. 133-134, pp. 673–674, Mar. 2003.

[67] H. Yoshida, K. Tsutsumi, and N. Sato, "Unoccupied electronic states of 3d-transition metal phthalocyanines (MPc: M=Mn, Fe, Co, Ni, Cu and Zn) studied by inverse photoemission spectroscopy," *J. Electron Spectrosc. Relat. Phenom.*, vol. 121, pp. 83–91, Dec. 2001.

[68] J. Szuber, B. Szczepaniak, S. Kochowski, and A. Opilski, "Electronic properties of the iron phthalocyanine thin films UHV annealed and exposed to oxygen," *Vacuum*, vol. 46, pp. 547–549, May 1995.

[69] J. Szuber, B. Szczepaniak, M. Piwowarczyk, S. Kochowski, and A. Opilski, "Electronic properties of the space charge layer of the copper phthalocyanine thin films," *Czech. J. Phys.*, vol. 43, pp. 1041–1044, Sept. 1993.

[70] E. E. Koch and W. D. Grobman, "Ultraviolet photoemission studies of phthalocyanines," *J. Chem. Phys.*, vol. 67, pp. 837–, July 1977.

[71] W. Pong and J. A. Smith, "Photoelectric emission from copper phthalocyanine films," *J. Appl. Phys.*, vol. 44, pp. 174–176, Jan. 1973.

[72] B. Bialek, I. G. Kim, and J. I. Lee, "Ab initio study of the electronic structure of nickel phthalocyanine-monolayer and bulk," *Synth. Met.*, vol. 129, pp. 151–156, July 2002.

[73] H. Engelkamp, S. Middelbeek, and R. J. M. Nolte, "Self-assembly of disk-shaped molecules to coiled-coil aggregates with tunable helicity," *Science*, vol. 284, pp. 785–788, Apr. 1999.

[74] R. Gould and N. Ibrahim, "The electrical response of evaporated cobalt phthalocyanine thin films on exposure to NO_2," *Thin Solid Films*, vol. 398-399, pp. 432–437, Nov. 2001.

[75] W. Chen, B. Zhao, Y. Pan, Y. Yao, S. Lu, S. Chen, and L. Du, "reparation of a thermosensitive cobalt phthalocyanine/N-isopropylacrylamide copolymer and its catalytic activity on thiol," *J. Colloid Interface Sci.*, vol. 300, pp. 626–632, Aug. 2006.

[76] V. Iliev, V. Alexiev, and L. Bilyarska, "Effect of metal phthalocyanine complex aggregation on the catalytic and photocatalytic oxidation of sulfur containing compounds," *J. Mol. Catal. A: Chem.*, vol. 137, pp. 15–22, Jan. 1999.

[77] Y. Pan, W. Chen, S. Lu, and Y. Zhang, "Novel aqueous soluble cobalt phthalocyanine: synthesis and catalytic activity on oxidation of 2-mercaptoethanol," *Dyes and Pigments*, vol. 66, pp. 115–121, Aug. 2005.

[78] A. Sorokin, J.-L. Seris, and B. Meunier, "Efficient oxidative dechlorination and aromatic ring cleavage of chlorinated phenols catalyzed by iron sulfophthalocyanine," *Science*, vol. 268, pp. 1163–1166, May 1995.

[79] J. R. Premkumar and R. Ramaraj, "Photoreduction of carbon dioxide by metal phthalocyanine adsorbed nafion membrane," *Chem. Commun.*, pp. 343–344, Jan. 1997.

[80] B. Bialek, I. G. Kim, and J. I. Lee, "Density functional investigation of the electronic structure of cobalt phthalocyanine monolayer," *Thin Solid Films*, vol. 513, pp. 110–113, Feb. 2006.

[81] D. Schlettwein and T. Yoshida, "Electrochemical reduction of substituted cobalt phthalocyanines adsorbed on graphite," *J. Electroanal. Chem.*, vol. 441, pp. 139–146, Jan. 1998.

[82] G. I. Cardenas-Jiron, M. A. Gulppi, C. A. Caro, M. P. R. del Rio, and J. H. Zagal, "Reactivity of electrodes modified with substituted metallophthalocyanines. correlations with redox potentials, hammett parameters and donor-acceptor intermolecular hardness," *Electrochim. Acta*, vol. 46, pp. 3227–3235, July 2001.

[83] R. Lezna, S. Juanto, and J. Zagal, "Spectroelectrochemical studies of tetrasulfonated metallophthalocyanines adsorbed on the basal plane of graphite in the presence of cysteine," *J. Electroanal. Chem.*, vol. 452, pp. 221–228, July 1998.

[84] J. H. Zagal, M. A. Gulppi, C. A. Caro, and G. Cardenas-Jiron, "Paradoxical effect of the redox potential of adsorbed metallophthalocyanines on their activity for the oxidation of 2-mercaptoethanol. inner versus outer sphere electrocatalysis," *Electrochem. Commun.*, vol. 1, pp. 389–393, Sept. 1999.

[85] J. H. Zagal, M. A. Gulppi, M. Isaacs, G. Cardenas-Jiron, and M. J. Aguirre, "Linear versus volcano correlations between electrocatalytic activity and redox and electronic properties of metallophthalocyanines," *Electrochim. Acta*, 1998.

[86] J. H. Zagal, M. A. Gulppi, and G. Cardenas-Jiron, "Metal-centered redox chemistry of substituted cobalt phthalocyanines adsorbed on graphite and correlations with MO calculations and Hammett parameters. electrocatalytic reduction of a disulfide," *Polyhedron*, vol. 19, pp. 2255–2260, Nov. 2000.

[87] G. Guillaud, J. Simon, and J. Germain, "Metallophthalocyanines gas sensors, resistors and field effect transistors," *Coord. Chem. Rev.*, vol. 178-180, pp. 1433–1484, Dec. 1998.

[88] S. T. Lee, Y. M. Wang, X. Y. Hou, and C. W. Tang, "Interfacial electronic structures in an organic light-emitting diode," *Appl. Phys. Lett.*, vol. 74, pp. 670–672, Feb. 1999.

[89] T. A. Temofonte and K. F. Schoch, "Phthalocyanine semiconductor sensors for room-temperature ppb level detection of toxic gases," *J. Appl. Phys.*, vol. 65, pp. 1350–1355, Feb. 1989.

[90] S. L. Lai, M. Y. Chan, M. K. Fung, C. S. Lee, and S. T. Lee, "Copper hexadecafluorophthalocyanine and copper phthalocyanine as a pure organic connecting unit in blue tandem organic light-emitting devices," *J. Appl. Phys.*, vol. 101, p. 014509(4), Jan. 2007.

[91] S. M. Tadayyon, H. M. Grandin, K. Griffiths, P. R. Norton, H. Aziz, and Z. D. Popovic, "CuPc buffer layer role in OLED performance: a study of the interfacial band energies," *Organic Electronics*, vol. 5, pp. 157–166, June 2004.

[92] J. L. Zhang, J. L. Xu, T. C. Niu, Y. H. Lu, L. Liu, and W. Chen, "Reversible switching of a single-dipole molecule imbedded in two-dimensional hydrogen-bonded binary molecular networks," *J. Phys. Chem. C*, vol. 118, pp. 1712–1718, Jan. 2014.

[93] F. Aziz, K. Sulaiman, M. R. Muhammad, M. H. Sayyadb, and K. Karimov, "nfluence of thermal annealing on the structural properties of vanadyl phthalocyanine thin films: A comparative study," *Int. J. Chem. Mole. Nucl. Mater. Metal. Engi.*, vol. 5, no. 8, pp. 693–695, 2011.

[94] S. Daly, M. Girod, M. Vojkovic, A. Giuliani, R. Antoine, L. Nahon, R. A. J. OHair, and P. Dugourd, "Single-photon, double photodetachment of nickel phthalocyanine tetrasulfonic acid 4- anions," *J. Phys. Chem. Lett.*, vol. 7, pp. 2586–2590, June 2016.

[95] M. T. Hussein, E. M. Nasir, and A. H. Al-Aarajiy, "Structural and surface morphology analysis of nickel phthalocyanine thin films," *2013*, vol. 3, pp. 113–119, Apr. 2013.

[96] R. Daira, B. Boudjema, M. Mordjaoui, and M. Meziri, "Electrical properties of metallophthalocyanine thin films," *Optoelectron. Adv. Mat.*, vol. 5, pp. 167–171, Feb. 2011.

[97] J. B. Brito, D. J. C. Gomes, V. D. Justina, A. M. F. Lima, C. A. Olivati, J. R. Silva, and N. C. de Souza, "Nanostructured films from phthalocyanine and carbon nanotubes: Surface morphology and electrical characterization," *J. Colloid Interface Sci.*, vol. 367, pp. 467–471, Feb. 2012.

[98] B. Joseph and C. S. Menon, "Studies on the optical properties and surface morphology of nickel phthalocyanine thin films," *J. Chem.*, vol. 4, pp. 255–264, Apr. 2007.

[99] S.-B. Lee, S.-I. Pyun, and E.-J. Lee, "Effect of the compactness of the lithium chloride layer formed on the carbon cathode on the electrochemical reduction of SOCl$_2$ electrolyte in Li-SOCl$_2$ batteries," *Electrochim. Acta*, vol. 47, pp. 855–864, Dec. 2001.

[100] M. M. Morrison, "Studies in lithium oxyhalide cells for downhole instrumentation use of lithium tetrachlorogallate electrolyte in Li/SOCl$_2$ cells," *J. Power Sources*, vol. 45, pp. 343–352, July 1993.

[101] N. Marom, X. Ren, J. E. Moussa, J. R. Chelikowsky, and L. Kronik, "Electronic structure of copper phthalocyanine from G$_0$W$_0$ calculations," *Phys. Rev. B*, vol. 84, p. 195143(8), Nov. 2011.

[102] W. Auwarter, K. Seufert, F. Bischoff, D. Ecija, S. Vijayaraghavan, S. Joshi, F. Klappenberger, N. Samudrala, and J. V. Barth, "A surface-anchored molecular four-level conductance switch based on single proton transfer," *Nat. Nanotechnol.*, vol. 7, pp. 41–46, 2012.

[103] C. W. Tang, "Two-layer organic photovoltaic cell," *Appl. Phys. Lett.*, vol. 48, pp. 183–185, Jan. 1986.

[104] J. Wang, H. Wang, X. Yan, H. Huang, and D. Yan, "Air-stable ambipolar organic field-effect transistors based on phthalocyanince composites heterojunction," *Chem. Phys. Lett.*, vol. 407, pp. 87–90, May 2005.

[105] R. Ye, M. Baba, K. Suzuki, and K. Mori, "Structure and morphology of CuPc and F$_{16}$CuPc *pn* heterojunction," *Appl. Surf. Sci.*, vol. 254, pp. 7885–7888, Sept. 2008.

[106] H. Wang, J. Wang, H. Huang, X. Yan, and D. Yan, "Organic heterojunction with reverse rectifying characteristics and its application in field-effect transistors," *Org. Electr.*, vol. 7, pp. 369–374, Oct. 2006.

[107] I. G. Hill and A. Kahn, "Energy level alignment at interfaces of organic semiconductor heterostructures," *J. Appl. Phys.*, 1998.

[108] S. Kera, Y. Yabuuchi, H. Yamane, H. Setoyama, K. K. Okudaira, A. Kahn, and N. Ueno, "Impact of an interface dipole layer on molecular level alignment at an organic-conductor interface studied by ultraviolet photoemission spectroscopy," *Phys. Rev. B*, vol. 70, p. 085304(6), Aug. 2004.

[109] M. Knupfer and H. Peisert, "Electronic properties of interfaces between model organic semiconductors and metals," *Phys. Stat. Sol. (a)*, vol. 201, pp. 1055–1074, May 2004.

[110] A. S. Komolov and P. J. Moller, "Electronic charge distribution at interfaces between Cu-phthalocyanine films and semiconductor surfaces," *Surf. Sci.*, vol. 532-535, pp. 1004–1010, June 2003.

[111] J. D. Wright, "Gas adsorption on phthalocyanines and its effects on electrical properties," *Prog. Surf. Sci.*, vol. 31, no. 1-2, pp. 1–60, 1989.

[112] T. Chasse, C. I. Wu, I. G. Hill, and A. Kahn, "Band alignment at organic-inorganic semi-conductor interfaces: α-NPD and CuPc on InP(110)," *J. Appl. Phys.*, vol. 85, pp. 6589–6592, May 1999.

[113] E. I. H. Ishii, Kiyoshi Sugiyama and K. Seki, "Energy level alignment and interfacial electronic structures at organic/metal and organic/organic interfaces," *Adv. Mater.*, vol. 11, pp. 605–625, June 1999.

[114] I. Hill, J. Schwartz, and A. Kahn, "Metal-dependent charge transfer and chemical interaction at interfaces between 3,4,9,10-perylenetetracarboxylic bisimidazole and gold, silver and magnesium," *Organic Electron.*, vol. 1, pp. 5–13, Dec. 2000.

[115] T. Shimada, K. Hamaguchi, A. Koma, and F. S. Ohuchi, "Electronic structures at the interfaces between copper phthalocyanine and layered materials," *Appl. Phys. Lett.*, vol. 72, pp. 1869–1871, Apr. 1998.

[116] A. Calzolari, A. Ferretti, and M. B. Nardelli, "*Ab initio* correlation effects on the electronic and transport properties of metal(II)-phthalocyanine-based devices," *Nanotech.*, vol. 18, p. 424013(7), Sept. 2007.

[117] J. Ren, S. Meng, Y.-L. Wang, X.-C. Ma, Q.-K. Xue, and E. Kaxiras, "Properties of copper (fluoro-)phthalocyanine layers deposited on epitaxial graphene," *J. Chem. Phys.*, vol. 134, p. 194706(10), May 2011.

[118] S. Campidelli, B. Ballesteros, A. Filoramo, D. D. Diaz, G. de la Torre, T. Torres, G. M. A. Rahman, C. Ehli, D. Kiessling, F. Werner, V. Sgobba, D. M. Guldi, C. Cioffi, M. Prato, and J.-P. Bourgoin, "Facile decoration of functionalized single-wall carbon nanotubes with phthalocyanines via click chemistry," *J. Am. Chem. Soc.*, vol. 130, pp. 11503–11509, July 2008.

[119] J.-J. Cid, J.-H. Yum, S.-R. Jang, M. K. Nazeeruddin, E. Martinez-Ferrero, E. Palomares, J. Ko, and M. G. T. Torres, "Molecular cosensitization for efficient panchromatic dye-sensitized solar cells," *Angew Chem Int Ed.*, vol. 46, pp. 8358–8362, Nov. 2007.

[120] J. R. Pinzon, M. E. Plonska-Brzezinska, C. M. Cardona, A. J. Athans, S. S. Gayathri, D. M. Guldi, M. A. Herranz, N. Martin, T. Torres, and L. Echegoyen, "$Sc_3N@C_{80}$-ferrocene electron-donor/acceptor conjugates as promising materials for photovoltalic applications," *Angew. Chem. Int. Ed.*, vol. 47, pp. 4173–4176, May 2008.

[121] G. Lobbert, *Phthalocyanines. Ullmann's Encyclopedia of Industrial Chemistry*. Wiley-VCH Verlag GmbH & Co. KGaA, Weinheim, 2000.

[122] P. Liljeroth, J. Repp, and G. Meyer, "Current-induced hydrogen tautomerization and conductance switching of naphthalocyanine molecules," *Science*, vol. 317, pp. 1203–1206, Aug. 2007.

[123] G. V. Nazin, X. H. Qiu, and W. Ho, "Visualization and spectroscopy of a metal-molecule-metal bridge," *Science*, vol. 302, pp. 77–81, Oct. 2003.

[124] J. L. Zhang, J. L. Xu, T. C. Niu, Y. H. Lu, L. Liu, and W. Chen, "Reversible switching of a single-dipole molecule imbedded in two-dimensional hydrogen-bonded binary molecular networks," *J. Phys. Chem. C.*, vol. 118, pp. 1712–1718, 2014.

[125] P. Jarvinen, S. K. Hamalainen, K. Banerjee, P. Hakkinen, M. I. A. Harju, and P. Liljeroth, "Molecular self-assembly on graphene on SiO_2 and *h*-BN substrates," *Nano Lett.*, vol. 13, pp. 3199–3204, June 2013.

[126] C. A. Melendres and X. Feng, "On the electrochemical behavior of iron phthalocyanine film electrodes in acid solution," *J. Electrochem. Soc.*, vol. 130, no. 4, pp. 811–814, 1983.

[127] Y. Asai, S. Miyata, K. Onishi, T. Arai, M. Matsumoto, and K. Shigehara, "Metal-free octacyanophthalocyanine as cathode-active material for a secondary lithium battery," *Electrochim. Acta*, vol. 46, pp. 77–81, Oct. 2000.

[128] S. Zhang, X. Ren, and J. Read, "Heat-treated metal phthalocyanine complex as an oxygen reduction catalyst for non-aqueous electrolyte Li/air batteries," *Electrochim. Acta*, vol. 56, pp. 4544–4548, Apr. 2011.

[129] Y. Asai, K. Onishi, S. Miyata, S. J. Kim, M. Matsumoto, and K. Shigehara, "Octacyanophthalocyaninatoiron polymer as cathode material for a secondary lithium battery," *J. Electrochem Soc.*, vol. 148, no. 4, pp. A305–A310, 2001.

[130] Z. Xu, H. Li, H. Sim, Q. Zhang, and K. Li, "Carbon nanotubes with phthalocyanine-decorated surface produced by NH_3-assisted microwave reaction and their catalytic performance in Li/SOCl$_2$ battery," *Chinese J. Chem.*, vol. 28, pp. 2059–2066, Oct. 2010.

[131] Z. Xu, G. Zhang, Z. Cao, J. Zhao, and H. Li, "Effect of N atoms in the backbone of metal phthalocyanine derivatives on their catalytic activity to lithium battery," *J. Mol. Cat. A Chemical*, vol. 318, pp. 101–105, Mar. 2010.

[132] Y. S. Guo, H. H. Ge, G. D. Zhou, and Y. P. Wu, "Comparative study on carbon cathodes with and without cobalt phthalocyanine in Li/(SOCl$_2$ + BrCl) cells," *J. Power Sources*, vol. 194, pp. 508–514, Dec. 2009.

[133] S. Matsuda, S. Mori, Y. Kubo, K. Uosaki, K. Hashimoto, and S. Nakanishi, "Cobalt phthalocyanine analogs as soluble catalysts that improve the charging performance of Li-O_2 batteries," *Chem. Phys. Lett.*, vol. 620, pp. 78–81, Jan. 2015.

[134] Z. Liu, Q. Jiang, R. Zhang, R. Gao, and J. Zhao, "Graphene/phthalocyanine composites and binuclear metal phthalocyanines with excellent electrocatalytic performance to Li/$SOCl_2$ battery," *Electrochim. Acta*, vol. 187, pp. 81–91, Jan. 2016.

[135] M. A. Green, K. Emery, Y. Hishikawa, and W. Warta, "Solar cell efficiency tables (version 33)," *Prog. Photovolt: Res. Appl.*, vol. 17, pp. 85–94, Jan. 2009.

[136] J. Y. Kim, K. Lee, N. E. Coates, D. Moses, T. Q. Nguyen, M. Dante, and A. J. Heeger, "Efficient tandem polymer solar cells fabricated by all-solution processing," *Science*, vol. 317, pp. 222–225, July 2007.

[137] W. Ma, C. Yang, X. Gong, K. Lee, and A. J. Heeger, "Thermally stable, efficient polymer solar cells with nanoscale control of the interpenetrating network morphology," *Adv. Funct. Mater.*, vol. 15, pp. 1617–1622, Oct. 2005.

[138] J. Xue, S. Uchida, B. P. Rand, and S. R. Forrest, "Asymmetric tandem organic photovoltaic cells with hybrid planar-mixed molecular heterojunctions," *Appl. Phys. Lett.*, vol. 85, pp. 5757–5759, Dec. 2004.

[139] N. R. Armstrong, W. Wang, D. M. Alloway, D. Placencia, E. Ratcliff, and M. Brumbach, "Organic/organic' heterojunctions: Organic light emitting diodes and organic photovoltaic devices," *Macromol. Rapid Commun.*, vol. 30, pp. 717–731, May 2009.

[140] S. W. Cho, L. F. J. Piper, A. DeMasi, A. R. H. Preston, K. E. Smith, K. V. Chauhan, P. Sullivan, R. A. Hatton, and T. S. Jones, "Electronic structure of C_{60}/Phthalocyanine/ITO interfaces studied using soft x-ray spectroscopies," *J. Phys. Chem. C.*, vol. 114, pp. 1928–1933, Jan. 2010.

[141] S. H. Park, J. G. Jeong, H.-J. Kim, S.-H. Park, M.-H. Cho, S. W. Cho, Y. Yi, M. Y. Heo, and H. Sohn, "The electronic structure of C_{60}/ZnPc interface for organic photovoltaic device with blended layer architecture," *Appl. Phys. Lett.*, vol. 96, p. 013302(3), Jan. 2010.

[142] H. Huang, W. Chen, and A. T. S. Wee, "Low-temperature scanning tunneling microscopy investigation of epitaxial growth of F_{16}CuPc thin films on Ag(111)," *J. Phys. Chem. C*, vol. 112, pp. 14913–14918, July 2008.

[143] S. Pfuetzner, J. Meiss, A. Petrich, M. Riede, and K. Leo, "Thick C_{60}: ZnPc bulk heterojunction solar cells with improved performance by film deposition on heated substrates," *Appl. Phys. Lett.*, vol. 94, p. 253303(3), June 2009.

[144] R. Schueppel, R. Timmreck, N. ALllinger, T. Mueller, M. Furno, C. Uhrich, K. Leo, and M. Riede, "Controlled current matching in small molecule organic tandem solar cells using doped spacer layers," *J. Appl. Phys.*, vol. 107, p. 044503(6), Feb. 2010.

[145] J. T. Sun, Y. H. Lu, W. Chen, Y. P. Feng, and A. T. S. Wee, "Linear tuning of charge carriers in graphene by organic molecules and charge-transfer complexes," *Phys. Rev. B*, vol. 81, p. 155403(6), Apr. 2010.

[146] K. M. Lau, J. X. Tang, H. Y. Sun, C. S. Lee, S. T. Lee, and D. H. Yan, "Interfacial electronic structure of copper phthalocyanine and copper hexadecafluorophthalocyanine studied by photoemission," *Appl. Phys. Lett.*, vol. 88, p. 173513(3), Apr. 2006.

[147] S.-H. Lee, D.-H. Kim, J.-H. Kim, T.-H. Shim, and J.-G. Park, "Impact of donor, acceptor, and blocking layer thickness on power conversion efficiency for small-molecular organic solar cells," *Synth. Met.*, vol. 159, pp. 1705–1709, Sept. 2009.

[148] A. Ruocco, F. Evangelista, R. Gotter, A. Attili, and G. Stefani, "Evidence of charge transfer at the Cu-Phthalocyanine/Al(100) interface," *J. Phys. Chem. C*, vol. 112, pp. 2016–2025, Jan. 2008.

[149] L. Yan, N. J. Watkins, S. Zorba, Y. L. Gao, and C. W. Tang, "Thermodynamic equilibrium and metal-organic interface dipole," *Appl. Phys. Lett.*, vol. 81, pp. 2752–2754, Oct. 2002.

[150] A. S. Komolov and P. J. Moller, "Unoccupied electronic states and energy level alignment at interfaces between Cu-phthalocyanine films and semiconductor surfaces," *Synthetic Metals*, vol. 138, pp. 119–123, June 2003.

[151] Z. Bao, A. J. Lovinger, and J. Brown, "New air-stable *n*-channel organic thin film transistors," *J. Am. Chem. Soc.*, vol. 120, pp. 207–208, Jan. 1998.

[152] Y. J. Zhang, H. L. Dong, Q. X. Tang, S. Ferdous, F. Liu, S. C. B. Mannsfeld, W. P. Hu, and A. L. Briseno, "Organic single-crystalline *p-n* junction nanoribbons," *J. Am. Chem. Soc.*, vol. 132, pp. 11580–11584, Aug. 2010.

[153] L. G. D. Arco, Y. Zhang, C. W. Schlenker, K. Ryu, M. E. Thompson, and C. W. Zhou, "Continuous, highly flexible, and transparent graphene films by chemical vapor deposition for organic photovoltaics," *ACS Nano*, vol. 4, pp. 2865–2873, Apr. 2010.

[154] P. Hohenberg and W. Kohn, "Inhomogeneous electron gas," *Phys. Rev.*, vol. 136, pp. B864–B871, Nov. 1964.

[155] W. Kohn and L. J. Sham, "Self-consistent equations including exchange and correlation effects," *Phys. Rev.*, vol. 140, pp. A1133–A1138, Nov. 1965.

[156] J. P. Perdew, J. A. Chevary, S. H. Vosko, K. A. Jackson, M. R. Pederson, D. J. Singh, and C. Fiolhais, "Atoms, molecules, solids, and surfaces: Applications of the generalized gradient approximation for exchange and correlation," *Phys. Rev. B*, vol. 46, pp. 6671–6687, Sept. 1992.

[157] J. P. Perdew, K. Burke, and M. Ernzerhof, "Generalized gradient approximation made simple," *Phys. Rev. Lett.*, vol. 77, pp. 3865–3868, Oct. 1996.

[158] A. D. Becke, "Density-functional exchange-energy approximation with correct asymptotic behavior," *Phys. Rev. A*, vol. 38, pp. 3098–3100, Sept. 1988.

[159] C. Lee, W. Yang, and R. G. Parr, "Development of the Colle-Salvetti correlation-energy formula into a functional of the electron density," *Phys. Rev. B*, vol. 37, pp. 785–789, Jan. 1988.

[160] D. D. Koelling and B. N. Harmon, "A technique for relativistic spin-polarised calculations," *J. Phys. C: Solid State Phys.*, vol. 10, pp. 3107–3114, Jan. 1977.

[161] M. Douglas and N. M. Kroll, "Quantum electrodynamical corrections to the fine structure of helium," *Ann. Phys.*, vol. 82, pp. 89–155, Jan. 1974.

[162] A. K. Geim and K. S. Novoselov, "The rise of graphene," *Nat. Mater.*, vol. 6, no. 3, pp. 183–191, 2007.

[163] N. Ghaderi and M. Peressi, "First-principle study of hydroxyl functional groups on pristine, defected graphene, and graphene epoxide," *J. Phys. Chem. C*, vol. 114, pp. 21625–21630, Nov. 2010.

[164] H. J. Yoon, D. H. Jun, J. H. Yang, Z. Zhou, S. S. Yang, and M. M. C. Cheng, "Carbon dioxide gas sensor using a graphene sheet," *Sens. Actuators, B*, vol. 157, pp. 310–313, Mar. 2011.

[165] R.-H. Kim, M.-H. Bae, D. G. Kim, H. Cheng, B. H. Kim, D.-H. Kim, M. Li, J. Wu, F. Du, H.-S. Kim, S. Kim, D. Estrada, S. W. Hong, Y. Huang, E. Pop, and J. A. Rogers, "Stretchable, transparent graphene interconnects for arrays of microscale inorganic light emitting diodes on rubber substrates," *Nano Lett.*, vol. 11, pp. 3881–3886, July 2011.

[166] J. Wu, M. Agrawal, H. C. A. Becerril, Z. Bao, Z. Liu, Y. Chen, and P. Peumans, "Organic light-emitting diodes on solution-processed graphene transparent electrodes," *ACS Nano*, vol. 4, pp. 43–48, Nov. 2009.

[167] Z. Yin, S. Sun, T. Salim, S. Wu, X. Huang, Q. He, Y. Lam, and H. Zhang, "Organic photovoltaic devices using highly flexible reduced graphene oxide films as transparent electrodes," *ACS Nano*, 2010.

[168] A. Ghosh, K. V. Rao, S. J. George, and C. N. R. Rao, "Noncovalent functionalization, exfoliation, and solubilization of graphene in water by employing a fluorescent coronene carboxylate," *Chem. Eur. J.*, vol. 16, pp. 2700–2704, Jan. 2010.

[169] J. Mao, H. Zhang, Y. Jiang, Y. Pan, M. Gao, W. Xiao, and H. J. Gao, "Tunability of supramolecular kagome lattices of magnetic phthalocyanines using graphene-based moire patterns as templates," *J. Am. Chem. Soc.*, vol. 131, pp. 14136–14137, Sept. 2009.

[170] J. D. Wuest and A. Rochefort, "Strong adsorption of aminotriazines on graphene," *Chem. Commun.*, 2010.

[171] G. I. Cardenas-Jiron, C. A. Caro, D. Venegas-Yazigi, and J. H. Zagal, "Theoretical study of the interaction energy profile of cobalt phthalocyanine and 2-mercaptoethanol effect of the graphite on the global reactivity," *J. Mol. Struct.*, vol. 580, pp. 193–200, Mar. 2002.

[172] D. C.-A. J. M. S. G. I. Cardenas-Jiron, P. A. Leon-Plata, "Electrical characteristics of cobalt phthalocyanine complexes adsorbed on graphene," *J. Phys. Chem. C*, vol. 115, pp. 16052–16062, July 2011.

[173] L. Cortez, L. C. Berrios, M. Yanez, and G. I. Cardenas-Jiron, "Theoretical study of the binding nature of glassy carbon with nickel(II) phthalocyanine complexes," *Chem. Phys.*, vol. 365, pp. 164–169, Nov. 2009.

[174] G. I. Cardenas-Jiron and C. Berrios, "Theoretical evidence of the ni(III) participation in the chlorophenol oxidation on tetrasulphonated nickel phthalocyanine," *Int. J. Quantum Chem.*, vol. 108, pp. 2586–2594, June 2008.

[175] G. I. Cardenas-Jiron, C. Gonzalez, and J. Benavides, "Nitric oxide oxidation mediated by substituted nickel phthalocyanines: a theoretical viewpoint," *J. Phys. Chem. C*, vol. 116, pp. 16979–16984, July 2012.

[176] G. I. Cardenas-Jiron, V. Paredes-Garcia, D. Venegas-Yazigi, J. H. Zagal, M. Paez, and J. Costamagna, "Theoretical modeling of the oxidation of hydrazine by iron(II) phthalocyanine in the gas phase: influence of the metal character," *J. Phys. Chem. A*, vol. 110, pp. 11870–11875, Oct. 2006.

[177] T. Mugadza and T. Nyokong, "Facile electrocatalytic oxidation of diuron on polymerized nickel hydroxo tetraamino-phthalocyanine modified glassy carbon electrodes," *Talanta*, vol. 81, pp. 1373–1379, June 2010.

[178] D. V.-Y.-J. H. Z. M. P. J. C. V. Paredes-Garcia, G. I. Cardenas-Jiron, "Through-space and through-bond mixed charge transfer mechanisms on the hydrazine oxidation by cobalt(II) phthalocyanine in the gas phase," *J. Phys. Chem. A*, vol. 109, pp. 1196–1204, Jan. 2005.

[179] S. J. Young, J. P. Hart, A. A. Dowman, and D. C. Cowell, "The non-specific inhibition of enzymes by environmental pollutants: a study of a model system towards the development of electrochemical biosensor arrays," *Biosens. Bioelectron.*, vol. 16, pp. 887–894, Dec. 2001.

[180] R. Bechara, J. Petersen, V. Gernigon, P. Leveqque, T. Heiser, V. Toniazzo, D. Ruch, and M. Michel, "PEDOT:PSS-free organic solar cells using tetrasulfonic copper phthalocyanine as buffer layer," *Sol. Energy Mater. Sol. Cells*, vol. 98, pp. 482–485, Mar. 2012.

[181] P. A. Lane, J. Rostalski, C. Giebeler, S. J. Martin, D. D. C. Bradley, and D. Meissner, "Electroabsorption studies of phthalocyanine/perylene solar cells," *Sol. Energy Mater. Sol. Cells*, vol. 63, pp. 3–13, June 2000.

[182] F. Liang, F. Shi, Y. Fu, L. Wang, X. Zhang, Z. Xie, and Z. Su, "Donor-acceptor conjugates-functionalized zinc phthalocyanine: towards broad absorption and application in organic solar cells," *Sol. Energy Mater. Sol. Cells*, vol. 94, pp. 1803–1808, Oct. 2010.

[183] R. Motoyoshi, A. Suzuki, K. Kikuchi, and T. Oku, "Formation and characterization of copper tetrakis (4-cumylphenoxy) phthalocyanine: perylene solar cells," *Synth. Met.*, vol. 159, pp. 1345–1348, July 2009.

[184] A. K. Sarker, M. G. Kang, and J.-D. Hong, "A near-infrared dye for dye-sensitized solar cell: Catecholate-functionalized zinc phthalocyanine," *Dyes Pigm.*, vol. 92, pp. 1160–1165, Mar. 2012.

[185] A. Chunder, T. Pal, S. I. Khondaker, and L. Zhai, "Reduced graphene oxide/copper phthalocyanine composite and its optoelectrical properties," *J. Phys. Chem. C*, vol. 114, pp. 15129–15135, Aug. 2010.

[186] A. Jomphoak, R. Maezono, and T. Onjun, "Density functional theory of graphene/Cu phthalocyanine composite material," *J. Surf. Coat. Tech.*, vol. 306, pp. 236–239, Nov. 2016.

[187] S. Kamada, H. Nomoto, K. Fukuda, T. Fukawa, H. Shirai, and M. Kimura, "Noncovalent wrapping of chemically modified graphene with π-conjugated disk-like molecules," *Colloid Polym. Sci.*, vol. 289, pp. 925–932, June 2011.

[188] J.-P. Zhong, Y.-J. Fan, H. Wang, R.-X. Wang, L.-L. Fan, X.-C. Shen, and Z.-J. Shi, "Copper phthalocyanine functionalization of graphene nanosheets as support for platinum nanoparticles and their enhanced performance toward methanol oxidation," *J. Power Sources*, vol. 242, pp. 208–215, Nov. 2013.

[189] J.-P. Zhong, Y.-J. Fana, H. Wang, R.-X. Wang, L.-L. Fan, X.-C. Shen, and Z.-J. Shi, "Highly active Pt nanoparticles on nickel phthalocyanine functionalized graphene nanosheets for methanol electrooxidation," *Electrochim. Acta*, vol. 113, pp. 653–660, Dec. 2013.

[190] J. Malig, N. Jux, D. Kiessling, J.-J. Cid, T. T. P. Vazquez, and D. M. Guldi, "Towards tunable graphene/phthalocyanine-PPV hybrid systems," *Angew. Chem., Int. Ed.*, vol. 50, pp. 3561–3565, Apr. 2011.

[191] X.-F. Zhang and Q. Xi, "A graphene sheet as an efficient electron acceptor and conductor for photo induced charge separation," *Carbon*, vol. 49, pp. 3842–3850, Oct. 2011.

[192] J. Zhu, Y. Li, Y. Chen, J. Wang, B. Zhang, J. Zhang, and W. J. Blau, "Graphene oxide covalently functionalized with zinc phthalocyanine for broadband optical limiting," *Carbon*, vol. 49, pp. 1900–1905, May 2011.

[193] Y. Liu, Y.-Y. Wu, G.-J. Lv, T. Pu, X.-Q. He, and L.-L. Cui, "Iron(II) phthalocyanine covalently functionalized graphene as a highly efficient non-precious-metal catalyst for the oxygen reduction reaction in alkaline media," *Electrochim. Acta*, vol. 112, pp. 269–278, Dec. 2013.

[194] N. Li, M. Zhu, M. Qu, X. Gao, X. Li, W. Zhang, J. Zhang, and J. Ye, "Iron-tetrasulfophthalocyanine functionalized graphene nanosheets: Attractive hybrid nanomaterials for electrocatalysis and electroanalysis," *J. Electroanal. Chem.*, vol. 651, pp. 12–18, Jan. 2011.

[195] P. Jarvinen, S. K. Hamalainen, M. Ijas, A. Harju, and P. Liljeroth, "Self-assembly and orbital imaging of metal phthalocyanines on a graphene model surface," *J. Phys. Chem. C*, vol. 118, pp. 13320–13325, May 2014.

[196] N. Marom and L. Kronik, "Density functional theory of transition metal phthalocyanines, II: electronic structure of mnpc and fepc-symmetry and symmetry breaking," *Appl.Phys.A*, vol. 95, pp. 165–172, Apr. 2009.

[197] N. Marom, O. Hod, G. E. Scuseria, and L. Kronik, "Electronic structure of copper phthalocyanine: a comparative density functional theory study," *J. Chem. Phys.*, vol. 128, p. 164107(18), Apr. 2008.

[198] J. Tirado-Rives and W. L. Jorgensen, "Performance of B3LYP density functional methods for a large set of organic molecules," *J. Chem. Theory Comput.*, vol. 4, pp. 297–306, Jan. 2008.

[199] J. Baker, M. Muir, J. Andzelm, and A. Scheiner, "Hybrid hartree-fock density-functional theory functionals: The adiabatic connection method," *ACS Symp. Ser.*, vol. 629, pp. 342–367, May 1996.

[200] B. J. Lynch and D. G. Truhlar, "How well can hybrid density functional methods predict transition state geometries and barrier heights?," *J. Phys. Chem. A*, vol. 105, pp. 2936–2941, Jan. 2001.

[201] S. Heutz, C. Mitra, W. Wu, A. J. Fisher, A. Kerridge, M. Stoneham, T. H. Harker, J. Gardener, H.-H. Tseng, T. S. Jones, C. Renner, and G. Aeppli, "Molecular thin films: A new type of magnetic switch," *Adv. Mater.*, vol. 19, pp. 3618–3622, Oct. 2007.

[202] H. Yamada, T. Shimada, and A. Koma, "Preparation and magnetic properties of manganese(II) phthalocyanine thin films," *J. Chem. Phys.*, vol. 108, pp. 10256–10261, June 1998.

[203] M. Evangelisti, J. Bartolome, L. J. de Jongh, and G. Filoti, "Magnetic properties of α-iron(II) phthalocyanine," *Phys. Rev. B*, vol. 66, p. 14410(11), Oct. 2002.

[204] P. Coppens, L. Li, and N. J. Zhu, "Electronic ground state of iron(II) phthalocyanine," *J. Am. Chem. Soc.*, vol. 105, pp. 6173–6174, Apr. 1983.

[205] P. S. Miedema, S. Stepanow, P. Gambardella, and F. M. F. de Groot, "2p x-ray absorption of iron-phthalocyanine," *J. Phys. Conf. Ser.*, vol. 190, p. 012143(6), July 2009.

[206] S. Stepanow, P. S. Miedema, A. Mugarza, G. Ceballos, P. Moras, J. C. Cezar, C. Carbone, F. M. F. de Groot, and P. Gambardella, "Mixed-valence behavior and strong correlation effects of metal phthalocyanines adsorbed on metals," *Phys. Rev. B*, vol. 83, p. 220401, June 2011.

[207] A. Mugarza, R. Robles, C. Krull, R. Korytar, N. Lorente, and P. Gambardella, "Electronic and magnetic properties of molecule-metal interfaces: Transition-metal phthalocyanines adsorbed on Ag(100)," *Phys. Rev. B*, vol. 85, p. 155437(13), Apr. 2012.

[208] Z. Honda, S. Sato, M. Hagiwara, T. Kida, M. Sakai, T. Fukuda, and N. Kamata, "Preparation and magnetic properties of phthalocyanine-based carbon materials containing transition metals," *J. Appl. Phys.*, vol. 120, p. 024902(6), July 2016.

[209] Y. Kitaoka, T. Sakai, K. Nakamura, T. Akiyama, and T. Ito, "Magnetism and multiplets in metal-phthalocyanine molecules," *J. Appl. Phys.*, vol. 113, p. 17E130(3), Mar. 2013.

[210] M. S. Liao and S. Scheiner, "Electronic structure and bonding in metal phthalocyanines, metal=Fe, Co, Ni, Cu, Zn, Mg," *J. Chem. Phys.*, vol. 114, pp. 9780–9791, June 2001.

[211] T. S. Srivastava, J. L. Przybylinski, and A. Nath, "Moessbauer study of the intermolecular interactions in the α and β polymorphs of iron and cobalt phthalocyanines," *Inorg. Chem.*, vol. 13, pp. 1562–1564, July 1974.

[212] S. Lee, M. Yudkowsky, W. P. Halperin, M. Y. Ogawa, and B. M. Hoffman, "One-dimensional magnetism in copper phthalocyanine," *Phys. Rev. B*, vol. 35, pp. 5003–5007, Apr. 1987.

[213] H. Rydberg, M. Dion, N. Jacobson, E. Schroder, P. Hyldgaard, S. I. Simak, D. Langreth, and B. Lundqvist, "Van der waals density functional for layered structures," *Phys. Rev. Lett.*, vol. 91, p. 126402(4), Sept. 2003.

[214] M. Dion, H. Rydberg, E. Schoder, D. C. Langreth, and B. I. Lundqvist, "Van der waals density functional for general geometries," *Phys. Rev. Lett.*, vol. 92, p. 246401(4), June 2004.

[215] J.-H. Yang, D. Mu, Y. Gao, J. Tan, A. Lu, and D. Ma, "Cobalt phthalocyanine-graphene complex for electro-catalytic oxidation of dopamine," *J. Nat. Gas Chem.*, vol. 21, pp. 265–269, May 2012.

[216] J.-H. Yang, Y. Gao, W. Zhang, P. Tang, J. Tan, A.-H. Lu, and D. Ma, "Cobalt phthalocyanine-graphene oxide nanocomposite: Complicated mutual electronic interaction," *J. Phys. Chem. C*, vol. 117, pp. 3785–3788, Jan. 2013.

[217] L. Cui, T. Pu, Y. Liu, and X. He, "Layer-by-layer construction of graphene/cobalt phthalocyanine composite film on activated gce for application as a nitrite sensor," *Electrochim. Acta*, vol. 88, pp. 559–564, Jan. 2013.

[218] G. I. Carrdenas-Jiron, P. laLeon Plata, D. Cortes-Arriagada, and J. M. Seminario, "Electron transport properties through graphene oxide-cobalt phthalocyanine complexes," *J. Phys. Chem. C*, vol. 117, pp. 23664–23675, Oct. 2013.

[219] S. Zhong, J. Q. Zhong, A. T. S. Wee, and W. Chen, "Molecular orientation and electronic structure at organic heterojunction interfaces," *J. Electron. Spectrosc. Relat. Phenom.*, vol. 204, pp. 12–22, Oct. 2015.

[220] I. Salzmann, A. Moser, M. Oehzelt, T. Breuer, X. Feng, Z.-Y. Juang, D. Nabok, R. G. D. Valle, S. Duhm, G. Heimel, A. Brillante, E. Venuti, I. Bilotti, C. Christodoulou, J. Frisch, P. Puschnig, C. Draxl, G. Witte, K. Mullen, and N. Koch, "Epitaxial growth of π-stacked perfluoropentacene on graphene-coated quartz," *ACS Nano*, vol. 6, pp. 10874–10883, Nov. 2012.

[221] O. Barbieri, M. Hahn, A. Herzog, and R. Kotz, "Capacitance limits of high surface area activated carbons for double layer capacitors," *Carbon*, vol. 43, pp. 1303–1310, May 2005.

[222] E. Frackowiak and F. Beguin, "Carbon materials for the electrochemical storage of energy in capacitors," *Carbon*, vol. 39, no. 6, pp. 937–950, 2001.

[223] C. Arbizzania, M. Mastragostino, and F. Soavi, "New trends in electrochemical supercapacitors," *J. Power Sources*, vol. 100, pp. 164–170, Nov. 2001.

[224] T. A. Centeno and F. Stoeckli, "On the specific double-layer capacitance of activated carbons, in relation to their structural and chemical properties," *J. Power Sources*, vol. 154, pp. 314–320, Mar. 2006.

[225] D. Y. Qu and H. Shi, "Studies of activated carbons used in double-layer capacitors," *J. Power Sources*, vol. 74, no. 1, pp. 99–107, 1998.

[226] J. Gambya, P. Tabernaa, P. Simona, J. Fauvarquea, and M. Chesneau, "Studies and characterisations of various activated carbons used for carbon/carbon supercapacitors," *J. Power Sources*, vol. 101, pp. 109–116, Oct. 2001.

[227] H. Shi, "Activated carbons and double layer capacitance," *Electrochim. Acta*, vol. 41, no. 10, pp. 1633–1639, 1996.

[228] J. Wang, S. Q. Zhang, Y. Z. Guo, J. Shen, S. M. Attia, B. Zhou, G. Z. Zheng, and Y. S. Gui, "Morphological effects on the electrical and electrochemical properties of carbon aerogels," *J. Electrochem. Soc.*, vol. 148, pp. D75–D77, June 2001.

[229] K. H. An, K. K. Jeon, J. K. Heo, S. C. Lim, D. J. Bae, and Y. H. Leez, "High-capacitance supercapacitor using a nanocomposite electrode of single-walled carbon nanotube and polypyrrole," *J. Electrochem. Soc.*, vol. 149, pp. A1058–A1062, June 2002.

[230] C. Du, J. Yeh, and N. Pan, "High power density supercapacitors using locally aligned carbon nanotube electrodes," *Nanotechnology*, vol. 16, pp. 350–353, Feb. 2005.

[231] E. Frackowiak and F. Beguin, "Electrochemical storage of energy in carbon nanotubes and nanostructured carbons," *Carbon*, vol. 40, no. 10, pp. 1775–1787, 2002.

[232] C. Niu, E. K. Sichel, R. Hoch, D. Moy, and H. Tennent, "High power electrochemical capacitors based on carbon nanotube electrodes," *Appl. Phys. Lett.*, vol. 70, pp. 1480–1482, Jan. 1997.

[233] F. Pico, J. M. Rojo, M. L. Sanjuan, A. Anson, A. M. Benito, M. A. Callejas, W. K. Maserc, and M. T. Martinez, "Single-walled carbon nanotubes as electrodes in supercapacitors," *J. Electrochem. Soc.*, vol. 151, pp. A831–A837, June 2004.

[234] E. Frackowiak, K. Metenier, V. Bertagna, and F. Beguin, "Supercapacitor electrodes from multiwalled carbon nanotubes," *Appl. Phys. Lett.*, vol. 77, pp. 2421–2423, July 2000.

[235] K. H. An, W. S. Kim, Y. S. Park, Y. C. Choi, S. M. Lee, D. C. Chung, D. J. Bae, S. C. Lim, and Y. H. Lee, "Supercapacitors using single-walled carbon nanotube electrodes," *Adv. Mater.*, vol. 13, pp. 497–500, Apr. 2001.

[236] K. H. An, W. S. Kim, Y. S. Park, J.-M. Moon, D. J. Bae, S. C. Lim, Y. S. Lee, and Y. H. Lee, "Electrochemical properties of high-power supercapacitors using single-walled carbon nanotube electrode," *Adv. Funct. Mater.*, vol. 11, pp. 387–392, Oct. 2001.

[237] B.-J. Yoon, S.-H. Jeong, K.-H. Lee, H. S. Kim, C. G. Park, and J. H. Han, "Electrical properties of electrical double layer capacitors with integrated carbon nanotube electrodes," *Chem. Phys. Lett.*, vol. 388, pp. 170–174, Apr. 2004.

[238] B. Conway, V. Birss., and J. Wojtowicz, "The role and utilization of pseudocapacitance for energy storage by supercapacitors," *J. Power Sources*, vol. 66, pp. 1–14, May 1997.

[239] B. E. Conway, "Transition from supercapacitor to battery behavior in electrochemical energy storage," *J. Electrochem. Soc.*, vol. 138, pp. 1539–1548, Nov. 1991.

[240] I. H. Kim and K. B. Kim, "Ruthenium oxide thin film electrodes for supercapacitors," *Electrochem. Solid-State Lett.*, vol. 4, no. 5, pp. A62–A64, 2001.

[241] M. Mastragostino, C. Arbizzani, and F. Soavi, "Polymer-based supercapacitors," *J. Power Sources*, vol. 97-98, pp. 812–815, July 2001.

[242] K. S. Ryu, K. M. Kim, N.-G. Park, Y. J. Park, and S. H. Chang, "Symmetric redox supercapacitor with conducting polyaniline electrodes," *J. Power Sources*, vol. 103, pp. 305–309, Jan. 2002.

[243] G. A. Snook, P. Kao, and A. S. Best, "Conducting-polymer-based supercapacitor devices and electrodes," *J. Power Sources*, vol. 196, pp. 1–12, Jan. 2011.

[244] C. Arbizzani, M. Mastragostino, and L. Meneghello, "Polymer-based redox supercapacitors: A comparative study," *Electrochim. Acta*, vol. 41, pp. 21–26, Jan. 1996.

[245] E. Frackowiak, V. Khomenko, K. Jurewicz, K. Lota, and F. Beguin, "Supercapacitors based on conducting polymers/nanotubes composites," *J. Power Sources*, vol. 153, pp. 413–418, Feb. 2006.

[246] S. R. Sivakkumar and R. Saraswathi, "Performance evaluation of poly(N-methylaniline) and polyisothianaphthene in charge-storage devices," *J. Power Sources*, vol. 137, pp. 322–328, Oct. 2004.

[247] R. Sivakumar and R. Saraswathi, "Characterization of poly N-methylaniline) as a cathode active material in aqueous rechargeable batteries," *J. Power Sources*, vol. 104, pp. 226–233, Feb. 2002.

[248] H. Talbi, P. E. Just, and L. H. Dao, "Electropolymerization of aniline on carbonized polyacrylonitrile aerogel electrodes: applications for supercapacitors," *J. Appl. Electrochem.*, vol. 33, no. 6, pp. 465–473, 2003.

[249] M. Hughes, G. Z. Chen, M. S. P. Shaffer, D. J. Fray, and A. H. Windle, "Controlling the nanostructure of electrochemically grown nanoporous composites of carbon nanotubes and conducting polymers," *Compos. Sci. Technol.*, vol. 64, pp. 2325–2331, Nov. 2004.

[250] G. A. Snook, G. Z. Chen, D. J. Fray, M. Hughes, and M. Shaffer, "Studies of deposition of and charge storage in polypyrrole-chloride and polypyrrole-carbon nanotube composites with an electrochemical quartz crystal microbalance," *J. Electroanal. Chem.*, vol. 568, pp. 135–142, July 2004.

[251] D. F.-G. C. G.A. Snook, C. Peng, "Achieving high electrode specific capacitance with materials of low mass specific capacitance: Potentiostatically grown thick micronanoporous PEDOT films," *Electrochem. Commun.*, vol. 9, pp. 83–88, Jan. 2007.

[252] K. Lota, V. Khomenko, and E. Fracowiak, "Capacitance properties of poly(3,4-ethylenedioxythiophene)/carbon nanotubes composites," *J. Phys. Chem. Solids*, vol. 65, pp. 295–301, Mar. 2004.

[253] J. P. Zheng, P. J. Cygan, and T. R. Jow, "Hydrous ruthenium oxide as an electrode material for electrochemical capacitors," *J. Electrochem. Soc.*, vol. 142, no. 8, pp. 2699–2703, 1995.

[254] J. P. Zheng and T. R. Jow, "A new charge storage mechanism for electrochemical capacitors," *J. Electrochem. Soc.*, vol. 142, no. 1, pp. L6–L8, 1995.

[255] K. Jurewicz, S. Delpeux, V. Bertagna, F. Beguin, and E. Frackowiak, "Supercapacitors from nanotubes/polypyrrole composites," *Chem. Phys. Lett.*, vol. 347, pp. 36–40, Oct. 2001.

[256] E. Frackowiak, K. Jurewicz, S. Delpeux, and F. Beguin, "Nanotubular materials for supercapacitors," *J. Power Source*, vol. 97-98, pp. 822–825, July 2001.

[257] V. Khomenko, E. Frackowiak, and F. Beguin, "Determination of the specific capacitance of conducting polymer/nanotubes composite electrodes using different cell configurations," *Electrochim. Acta*, vol. 50, pp. 2499–2506, Apr. 2005.

[258] A. Laforgue, P. Simon, J. F. Fauvarque, M. Mastragostino, F. Soavi, J. F. Sarrau, P. Lailler, M. Conte, E. Rossi, and S. Saguatti, "Activated carbon/conducting polymer hybrid supercapacitors," *J. Electrochem. Soc.*, vol. 150, pp. A645–A651, Mar. 2003.

[259] M. Mastragostino, C. Arbizzani, and F. Soavi, "Conducting polymers as electrode materials in supercapacitors," *Solid State Ionics*, vol. 148, pp. 493–498, June 2002.

[260] H. Kim and B. N. Popov, "A mathematical model of oxide/carbon composite electrode for supercapacitors," *J. Electrochem. Soc.*, vol. 150, no. 1-2, pp. A1153–A1160, 2003.

[261] H. Li, L. Cheng, and Y. Xia, "A hybrid electrochemical supercapacitor based on a 5v li-ion battery cathode and active carbon," *Electrochem. Solid-State Lett.*, vol. 8, no. 9, pp. A433–A436, 2005.

[262] C. Lin, J. A. Ritter, and B. N. Popov, "Correlation of double-layer capacitance with the pore structure of sol-gel derived carbon xerogels," *J. Electrochem. Soc.*, vol. 146, pp. 3639–3643, June 1999.

[263] A. D. Pasquier, I. Plitz, S. Menocal, and G. Amatucci, "A comparative study of li-ion battery, supercapacitor and nonaqueous asymmetric hybrid devices for automotive applications," *J. Power Sources*, vol. 115, pp. 171–178, 2003.

[264] W. G. Pell and B. E. Conway, "Peculiarities and requirements of asymmetric capacitor devices based on combination of capacitor and battery-type electrodes," *J. Power Sources*, vol. 136, no. 2, pp. 334–345, 2004.

[265] X. Wang and J. P. Zheng, "The optimal energy density of electrochemical capacitors using two different electrodes," *J. Electrochem. Soc.*, vol. 151, no. 10, pp. A1683–A1689, 2004.

[266] L. Pauling, "The nature of the chemical bond. application of results obtained from the quantum mechanics and from a theory of paramagnetic susceptibility to the structure of molecules," *Nature Chem. Bond*, vol. 53, pp. 1367–1400, Apr. 1931.

[267] H. W. Kroto, J. R. Heath, S. C. Obrien, R. F. Curl, and R. E. Smalley, "C_{60} - The third man," *Nature*, vol. 318, pp. 162–163, Nov. 1985.

[268] S. Iijima and T. Ichihashi, "Single-shell carbon nanotubes of 1-nm diameter," *Nature*, vol. 363, pp. 603–605, June 1993.

[269] M. Monthioux and V. L. Kuznetsov, "Who should be given the credit for the discovery of carbon nanotubes?," *Carbon*, vol. 44, pp. 1621–1623, Aug. 2006.

[270] C. J. H. Wort and R. S. Balmer, "Diamond as an electronic material," *Mater. Today*, vol. 11, pp. 22–28, Jan. 2008.

[271] P. R. Wallace, "The band theory of graphite," *Phys. Rev. Lett.*, vol. 71, pp. 622–634, May 1947.

[272] G. W. Semenoff, "Condensed-matter simulation of a three-dimensional anomaly," *Phys. Rev. Lett.*, vol. 53, pp. 2449–2452, Dec. 1984.

[273] E. V. Castro, K. S. Novoselov, S. V. Morozov, N. M. R. Peres, J. D. Santos, J. Nilsson, F. Guinea, A. K. Geim, and A. H. C. Neto, "Biased bilayer graphene: semiconductor with a gap tunable by the electric field effect," *Phys. Rev. Lett.*, vol. 99, p. 216802(4), Nov. 2007.

[274] A. B. Kuzmenko, E. van Heumen, D. van der Marel, P. Lerch, P. Blake, K. S. Novoselov, and A. K. Geim, "Infrared spectroscopy of electronic bands in bilayer graphene," *Phys. Rev. B*, vol. 79, no. 11, p. 115441(5), 2009.

[275] S. V. Morozov, K. S. Novoselov, M. I. Katsnelson, F. Schedin, D. C. Elias, J. A. Jaszczak, and A. K. Geim, "Giant intrinsic carrier mobilities in graphene and its bilayer," *Phys. Rev. Lett.*, vol. 100, p. 016602(4), Jan. 2008.

[276] K. S. Novoselov, E. McCann, S. V. Morozov, V. I. Falko, M. I. Katsnelson, U. Zeitler, D. Jiang, F. Schedin, and A. K. Geim, "Unconventional quantum hall effect and berry's phase of 2π in bilayer graphene," *Nature Phys.*, vol. 2, pp. 177–180, Feb. 2006.

[277] T. Ohta, A. Bostwick, T. Seyller, K. Horn, and E. Rotenberg, "Controlling the electronic structure of bilayer graphene," *Science*, vol. 313, pp. 951–954, Aug. 2006.

[278] C. Lee, X. D. Wei, J. W. Kysar, and J. Hone, "Measurement of the elastic properties and intrinsic strength of monolayer graphene," *Science*, vol. 321, pp. 385–388, July 2008.

[279] R. R. Nair, P. Blake, A. N. Grigorenko, K. S. Novoselov, T. J. Booth, T. Stauber, N. M. R. Peres, and A. K. Geim, "Fine structure constant defines visual transparency of graphene," *Science*, vol. 320, p. 1308, June 2008.

[280] M. Levy, "Electron densities in search of hamiltonians," *Phys. Rev. A*, vol. 26, pp. 1200–1208, Sept. 1982.

[281] E. Lieb, "Density functionals for coulomb systems," *Int. Jour. Quant. Chem.*, vol. 24, pp. 243–277, Sept. 1983.

[282] S. Kera, H. Yamane, I. Sakuragi, K. K. Okudaira, and N. Ueno, "Very narrow photoemission bandwidth of the highest occupied state in a copper-phthalocyanine monolayer," *Chem. Phys. Lett.*, vol. 364, pp. 93–98, Sept. 2002.

[283] A. Rosa and E. J. Baerends, "Metal-macrocycle interaction in phthalocyanines: Density functional calculations of ground and excited states," *Inorg. Chem.*, vol. 33, pp. 584–595, Feb. 1994.

[284] A. D. Becke, "Density-functional thermochemistry. III. the role of exact exchange," *J. Chem. Phys.*, vol. 98, pp. 5648–5652, Apr. 1993.

[285] J. Heyd, G. E. Scuseria, and M. Ernzerhof, "Hybrid functionals based on a screened Coulomb potential," *J. Chem. Phys.*, vol. 118, pp. 8207–8215, May 2003.

Biography

Name	Mr. Apichai Jomphoak
Date of Birth	May 4th, 1977
Educational Attainment	2001: BS in Electrical Engineering, Lehigh University
	2011: MS in Technology, Sirindhorn International
	Institute of Technology
Scholarship	2014-2017: JAIST-SIIT-NECTEC Scholarship
	1996-2001: Royal Thai Scholarship
Work Experiences	2006-2013: Research Assistant
	National Electronics and Computer Technology Center

Publications

A. Jomphoak, R. Maezono, and T. Onjun. Density Functional Theory of Graphene/Cu Phthalocyanine Composite Material. Journal of Surface and Coating Technology, 306(A), 236-239, Nov. 2016. DOI: 10.1016/j.surfcoat.2016.06.015

International Conferences

A. Jomphoak, K. Hongo, and R. Maezono, Electronic Structure Calculations of Layered Perovskite Compound, $Li_2LaTa_2O_6N$, in the CASINO tutorial workshop in The Apuan Alps Centre for Physics (TTI 2017), 31 July - 4 August 2017, Vallico Sotto, Tuscany, Italy (2017).

A. Jomphoak, R. Maezono, and T. Onjun. Self-Interaction Effects of Transition Metal Phthalocyanines on Graphene: A DFT Study, in the 18th International Workshop on Computational Physics and Materials Science: Total Energy and Force Methods, 12-14 January 2017, Trieste, Italy (2017).

A. Jomphoak, R. Maezono, and T. Onjun. Density Functional Theory of Graphene/Metallophthalocyanines: Electronic Structure of CuPc, NiPc, and CoPc on Graphene, in the 2nd International Conference Advanced in Functional Materials (AFM 2016), 8-11 August 2016, Jeju, South Korea (2016) S1:8PVS-60.

A. Jomphoak, and T. Onjun. *Ab initio* Studies of Graphene/Cu Phthalocyanine Composite Material, in the 19th International Conference on Surface Modification of Materials by Ion Beans (SMMIB-19), 22-27 November 2015, Chiang Mai, Thailand (2015) CO17.

A. Jomphoak, T. Onjun, K. Hongo, and R. Maezono. Density Functional Theory Simulations of Aluminium Alkoxide and Fluoride, in the 4th International Symposium on Engineering, Energy and Environments (ISEEE 2015), 8-10 November 2015, Pattaya, Thailand (2015) MATE07.

A. Jomphoak, N. T. Cuong, and R. Maezono. A Quantum Monte Carlo Study on the Adsorption of CO Molecule on Cu(111) Surface, in the 5th Psi-K 2015 Conference, 6-10 September 2015, San Sebastian, Spain (2015) S10 439.